Doctoral Thesis

Ab initio molecular dynamics study of dynamic and electronic properties of covalent liquids under pressure

Satoshi Ohmura

Department of Physics
Graduate School of Science and Technology
Kumamoto University

March 2012

Contents

1 Introduction **8**

2 Method of Calculation **12**

2.1 Density functional theory 12

2.1.1 Kohn-Sham equation 13

2.1.2 Exchange-correlation energy 14

2.1.3 Pseudopotential approximation 17

2.2 Momentum-space formalism 20

2.3 Projector augumented waves (PAW) method 24

2.4 Hellmann-Feynman theorem 26

3 Dynanic properties of Liquid B_2O_3 under high pressure **28**

3.1 Introduction 28

3.2 Numerical details 30

3.3 Result and Discussion 31

3.3.1 Structure factor 31

3.3.2 Pair distribution function 34

3.3.3 Coordination-number distribution 37

3.3.4 Electronic density of states 38

3.3.5 Bond-overlap population 39

3.3.6 Mulliken charge 40

3.3.7 Diffusivity 42

3.3.8 Mechanism of atomic diffusion 43

3.3.9 Temperature dependence 52

3.4 Summary 53

4 Transport properties of liquid SiO_2, GeO_2 and $SrGeO_3$ 55
4.1 Introduction 55
4.2 Numerical details 56
4.3 Results of liquid SiO_2 57
  4.3.1 Coordination number dustribution 57
  4.3.2 Diffusion properties 58
4.4 Results of liquid GeO_2 and $SrGeO_3$ 59
  4.4.1 Pair distribution function 59
  4.4.2 Diffusion mechanism under ambient pressure 60
  4.4.3 Diffusion mechanism under high pressure 64
4.5 Discussion 66
4.6 Summary 67

5 Metalization in liquid Selenium under high pressure 68
5.1 Introduction 68
5.2 Numerical details 69
5.3 Results and discussion 71
  5.3.1 Structure factor 71
  5.3.2 Pair distribution function 72
  5.3.3 Electronic density of states 74
  5.3.4 Bond-overlap population 74
  5.3.5 Pressure-induced metallization of liquid Se 77
  5.3.6 Covalent-like interaction in the metallic state 78
  5.3.7 Comparison with liquid Te 79
  5.3.8 Dynamic properties 80
5.4 Summary 82

6 Polymerization transition in liquid AsS under pressure 84
6.1 Introduction 84
6.2 Numerical details 85
6.3 Results 86
  6.3.1 Volume-pressure relation 86
  6.3.2 Structure factor 87

6.3.3 Pair distribution function 89
6.3.4 Electronic density of states 91
6.3.5 Bond-overlap population 92
6.3.6 Diffusion coefficient 94
6.4 Discussion 95
6.5 Summary 97

7 Energy transport in light-harvesting dendrimer 98
7.1 Introduction 98
7.2 Numerical details 99
7.3 Result and discussion 99
7.3.1 Simulation result of the ground state 99
7.3.2 Simulation results of the excited state 102
7.3.3 Effects of the environments 103
7.3.4 Transfer time 104
7.4 Summary 104

8 Summary 106

List of Figures

1.1 Presssure dependence of the viscosity of various silicate and GeO_2 . . . 9

3.1 Density of liquid B_2O_3 . . . 31
3.2 Total structure factors of liquid B_2O_3. . . . 32
3.3 Partial structure factors of liquid B_2O_3 . . . 33
3.4 Partial pair distribution functions $g_{\alpha\beta}(r)$ of liquid B_2O_3. . . . 35
3.5 Nearest-neighbor distances and coordination number of liquid B_2O_3 . . . 36
3.6 Coordination-number distribution of liquid B_2O_3 . . . 37
3.7 Electronic density of states $D(E)$ of liquid B_2O_3 . . . 38
3.8 Angular-momentum l dependent partial electronic density of states of liquid B_2O_3 . . . 39
3.9 Bond-overlap populations of liquid B_2O_3 . . . 40
3.10 Distribution of the gross charges of liquid B_2O_3 . . . 41
3.11 Mean-square displacements of liquid B_2O_3 . . . 42
3.12 Diffusion coefficients of liquid B_2O_3 . . . 43
3.13 Diffusion mechanism 1 of liquid B_2O_3 . . . 45
3.14 Diffusion mechanism 1 relax of liquid B_2O_3 . . . 46
3.15 Diffusion mechanism 1 move of liquid B_2O_3 . . . 48
3.16 Diffusion mechanism 2 concerted reaction of liquid B_2O_3 . . . 50
3.17 Diffusion mechanism 3 of liquid B_2O_3 . . . 51
3.18 Partial pair distribution functions $g_{\alpha\beta}(r)$ of liquid B_2O_3. at a high temperature of 3500 K . . . 53

4.1 Coordination-number distribution of liquid SiO_2 . . . 57

4.2 Diffusion coefficients of liquid SiO_2 58

4.3 Pair distribution function $g(r)$ of liquid $SrGeO_3$ and GeO_2. . 59

4.4 Diffusion mechanism GeO_2 at ambient pressure 61

4.5 Diffusion mechanism of liquid $SrGeO_3$ 62

4.6 Diffusion mechanism II of liquid $SrGeO_3$ 63

4.7 Pressure dependence of the diffusion coefficients of liquid $SrGeO_3$ and GeO_2 64

4.8 Diffusion mechanisum of liquid GeO_2 under pressure 65

4.9 Pressure-temperature phase diagram of GeO_2 66

5.1 The total structure factor $S(k)$ of liquid Se. 71

5.2 Pair distribution function $g(r)$ of liquid Se. 72

5.3 Average coordination number and the nearest-neighbor distance of liquid Se 73

5.4 Electronic density of states $D(E)$ of liquid Se 75

5.5 Distribution of the bond-overlap populations of liquid Se . . . 76

5.6 Pair distribution function $g(r)$ at 9.4 GPa of liquid Se. 77

5.7 The time evolutions of the overlap populations $O_{ij}(t)$ of liquid Se 78

5.8 Diffusion coefficient and the share viscosity of liquid Se. 80

5.9 Velocity auto-correlation function and its Fourier transform of liquid Se 81

6.1 Volume as a function of pressure for liquid AsS at 1300 K. . . 86

6.2 Total structure factor liquid AsS 87

6.3 Partial structure factors of liquid AsS 88

6.4 Pair distribution functions of liquid AsS 89

6.5 Nearest-neighbor distances of liquid AsS 90

6.6 Electronic density of states of liquid AsS 92

6.7 Distribution of the bond-overlap populations of liquid AsS . . 93

6.8 Diffusion coefficients of liquid AsS 94

6.9 Pair distribution functions of liquid AsS 96

7.1 Spacial distribution of wavefunction in the ground state 100

7.2 Time evolution of electronic eigenenergies during adiabatic MD simulation for the ground state 101
7.3 Time evolution of electronic eigenenergies in TDKS-FSSH simulation. 102
7.4 Time evolution of electronic eigenenergies with and without THF solvent. 104
7.5 Time evolution of the existence probability of a photoexcited electron. 105

Chapter 1

Introduction

Since 2000, high pressure research of liquid structure has attracted great attentions. That year, a first-order liquid-liquid phase transition has been observed for phosphorus, that is, the structure of liquid phosphorus jumps suddenly from a molecular structure to a new polymetric structure form with higher density by increasing pressure [1]. After that, many high pressure studies have been conducted to investigate liquid structure, especially covalent liquids, such as liquid SiO_2, GeO_2, silicate and germanate, as candidates for observing pressure-induced first-order liquid-liquid phase transition. Additionally covalent liquids are attracted interest from earth science since they are strong related to Earth's mantle.

Besides structural changes, there are two interesting topics in research of covalent liquids under pressure. One is (i)viscosity behavior and the other is (ii)metallization.

(i) Viscosity of usual liquid such as liquid metal increase with pressure. However, a number of covalent liquids, such as SiO_2, GeO_2, silicates and germanates, have abnormal behavior of the viscosity shown in Fig. 1.1, i.e. the viscosity significantly drops with pressure [2, 3]. This anomalous behavior of the viscosity is considered to be related to the atomic diffusion in the liquids under pressure. Since it is very difficult to investigate the atomic diffusion in liquid state from experiment, the microscopic origin of anomalous pressure dependence of the viscosity is still unknown. It is, therefore, of particular interest to investigate the pressure dependence of the microscopic diffusion mechanism in covalent liquids with using computer simulation.

(ii)When pressure increases, metallization occurs in all substances. Liquids matter is no exception. The metallization of covalent liquids with increasing temperature have been intensively studied because of the anomaly

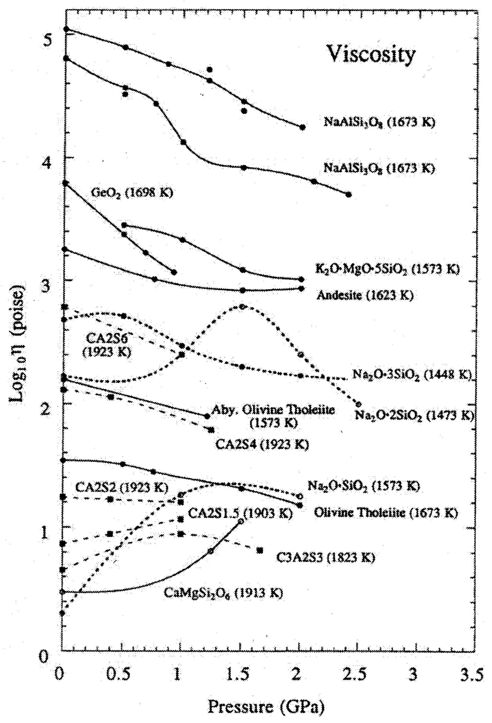

Figure 1.1: Presssure dependence of the viscosity of various silicate and GeO_2 [4]

which is metallization with volume expansion. On the other hand, pressure-induced metallization is accepted as expected phenomenon. Therefore, there are only a few studies about metallization with increasing pressure. Covalent liquids have strong local units such as SiO_4 tetrahedral unit, BO_3 triangle local unit and Se chain structure unit. When the pressure increases and metallization occurs, these local units should transform into other shape of local units or be broken. It is, however, unknown how to rearrange these local units.

Computer simulation based on molecular dynamics is powerful approach to clarify experimental difficult topics in the situation just described, such as the microscopic mechanism of atomic diffusion and the detail of pressure-induced metallization in covalent liquids.

Classical molecular dynamics (MD) using emprical potentials is well established as a powerful tool serving to investigate many-body condenced matter system including liquid system. Since the classical MD simulation is based on emprical potential, the result obtained from the simulation is significantly depended on the choice of the potential. To estimate the simulation result quantitatively, it is required to compare the result obtained by the simulation to the experimental result. Due to the above fact, the invesitigation based on classical MD simulation is very hard in the following type of system.

(i) "the extream condition system " such as high temperatute or high pressure in which it is difficult to perform experiments.

(ii) "the chemical complex system" in which there are many different type of interactions between atoms.

Ab initio molecular dynamics overcomes these problems. The basic idea underlying every *ab initio* mlecular dynamics method is to compute the forces acting on the nuclei from electronic structure calculations that are performed "on-the-fly" as the molecular dynamics trajectory is generated. Since forces acting on the nuclei are calculated without depending on the any emprical parameters in *ab initio* molecular dynamicis, the calculation under the extream condition such as high temperature or high pressure and the chemical complex system in which interactions between atoms changes between MD simulations or there are many different types interactions became possible.

We apply this *ab initio* molecular dynamics simulation to several covalent liquids. In addition, a new method of *ab initio* molecular dynamics adaptation of electronic transition and the application are introduced.

(i) liquid B_2O_3, SiO_2 GeO_2 and $SrGeO_3$ in order to clarify the dynamic properties of liquid oxide under pressure. Transport properties of liquid oxide, such as liquid B_2O_3, SiO_2 and GeO_2, under pressure are quite interesting in the sense that they show unexpected pressure dependence. It is, therefore, of partuicular interest to explore the dynamic properties and clarify the microscopic origin of the unexpected pressure dependence of liquid oxide. We focus on the relationship between macroscopic diffusion properties and microscopic diffusion mechanism.

(ii) liquid Se and liquid AsS in order to clarify the microscopic mechanism of pressure-induced metallization in liquid calcogenide. It is well known that pressure leads to sturctural change accompaning with metallization in liquid chalcogenide. However, the microcopic mechanism of the metallization and properties in the metallic state are still unknown. We focus on the the pressure effects on the covalent-like interaction during pressure-induced metallizatin.

(iii) light-harvesting dendrimer. The new method of *ab initio* molecular dynamics is introduced. Light-harvesting dendrimers is a example of the application. In the light-harvesting dendrimers, electronic excitation energy due to photoexcitation of antennas located on the periphery of the molecules is rapidly transported to the photochemical reaction centers at the cores of the molecules, which in turn perform useful work such as photosynthesis and molecular actuation. We focus on the energy tranport mechanism on atomic level.

Chapter 2

Method of Calculation

2.1 Density functional theory

The fundamental concept of density functional theory is that any properties of a system of many interacting particles can be viewed as a $functional$ of the ground state density $n_0(\mathbf{r})$; that is, one scalar function of position $n_0(\mathbf{r})$, in principle, determines all the information in the many-body wavefunctions for the ground state and all excited states. Density functional theory is based on two theorems first proved by Hohenberg and Kohn [5]. The relations based on the book "Electronic Structure" [6] can be started as follows:

- **Theorem I:** For any system of interacting particles in an external potential $V_{ext}(\mathbf{r})$ is determined uniquely, except for a constant, by the ground state density $n_0(\mathbf{r})$.

- **Corollary I:** Since the hamiltonian is thus determined, except for a constant shift of the energy, it follows that the many-body wavefunctions for all states (ground and excited) are determined. Therefore all properties of the system are completely determined given only the ground state density $n_0(\mathbf{r})$.

- **Theorem II:** A universal functional for the energy $E[n]$ in terms of the density $n(\mathbf{r})$ can be defined, valid for any external potential $V_{ext}(\mathbf{r})$. For any particular $V_{ext}(\mathbf{r})$, the exact ground state energy of the system is the exact ground state density $n_0(\mathbf{r})$.

- **Corollary II:** The functional $E[n]$ alone is sufficient to determine the exact ground state energy and density.

2.1.1 Kohn-Sham equation

The electronic structure of a physical system is calculated by the density functional theory (DFT). In the Kohn-Sham formulation of the DFT, the energy of the system is expressed as a functional of atomic positions $\{\mathbf{R}_I\}$ and one-electron wave functions (or Kohn-Sham orbitals) $\{\psi_m\}$ in the atomic unit:

$$\begin{aligned} E[\{\psi_m\},\{\mathbf{R}_I\}] =& T_s[\rho] + \sum_m f_m \int \psi_m^*(\mathbf{r}) V_{\text{ion}}(\mathbf{r}) \psi_m(\mathbf{r}) d\mathbf{r} \\ & + \frac{1}{2} \iint \frac{\rho(\mathbf{r})\rho(\mathbf{r}')}{|\mathbf{r}-\mathbf{r}'|} d\mathbf{r} d\mathbf{r}' + E_{\text{XC}}[\rho] + \frac{1}{2} \sum_{I \neq J} \frac{Z_I Z_J}{|\mathbf{R}_I - \mathbf{R}_J|} \end{aligned} \tag{2.1}$$

where $T_s[\rho]$ is the kinetic energy of a noninteracting electron gas in its ground state with the number density $\rho(\mathbf{r})$ of valence electrons, f_m an occupation number of mth electronic state,$\mathrm{V}_{ion}(\mathbf{r})$ an electron-ion interaction potential, $E_{XC}[\rho]$ the exchange-correlation energy functional, and the last term is the electrostatic energy between ions with valence $\{\mathrm{Z}_I\}$. The valence electron number density $\rho(\mathbf{r})$ is calculated as

$$\rho = \sum_m f_m |\psi_m(\mathbf{r})|^2 \tag{2.2}$$

The ground-state energy of the system, with given atomic position $\{\mathbf{R}_I\}$ is obtained by minimizing $E\{\{\psi_m\},\{\mathbf{R}_I\}\}$ with respect to $\{\{\psi_m\}\}$, subjected to orthonormality constraints,

$$\int \psi_m^*(\mathbf{r}) \psi_n(\mathbf{r}) d\mathbf{r} = \delta_{mn} \tag{2.3}$$

This minimization leads to the following eigenvalue equation (the Kohn-Sham equation),

$$\hat{H} \psi_m(\mathbf{r}) = \varepsilon_m \psi_m(\mathbf{r}) \tag{2.4}$$

with the eigenvalue ϵ_m for the mth electronic state. The Kohn-Sham Hamiltonian $\hat{H}$ is defined through

$$\hat{H}(\mathbf{r}) = -\frac{1}{2}\nabla^2 + V_{\mathrm{ion}}(\mathbf{r}) + V_{\mathrm{H}}(\mathbf{r}) + V_{\mathrm{XC}}(\mathbf{r}) \tag{2.5}$$

where $V_H(\mathbf{r})$ is the Hartree potential given by

$$V_H(\mathbf{r}) = \int \frac{\rho(\mathbf{r}')}{|\mathbf{r} - \mathbf{r}'|} d\mathbf{r}' \tag{2.6}$$

and $V_{\mathrm{XC}}(\mathbf{r}) = \delta E_{\mathrm{XC}}/\delta\rho$ is the exchange-correlation potential.

2.1.2 Exchange-correlation energy

The Kohn-Sham equations represent a mapping of the interacting many-electron system onto a system of noninteracting electrons moving in an effective potential originated from all the other electrons. If the exchange-correlation energy functional were known exactly, an exchange-correlation potential that included the effects of exchange and correlation exactly would be produced by taking the functional derivative with respect to the density.

Local density approximation

The Hohenberg-Kohn provides some motivation for using approximate methods to describe the exchange-correlation energy as a function of the electron. The simplest method is local density approximation (LDA). In LDA the exchange-correlation energy of electron system is constructed by assuming that the exchange-correlation energy per electron at a point $\mathbf{r}$ in the electron gas, $\epsilon_{XC}(\mathbf{r})$, is equal to the exchange-correlation energy per electron in a homogeneous electron gas that has the same density as the electron gas at point $\mathbf{r}$. Thus

$$E_{XC}[\rho(\mathbf{r})] = \int \epsilon_{XC}(\mathbf{r})\rho(\mathbf{r})d^3r \tag{2.7}$$

and

$$\frac{E_{XC}[\rho(\mathbf{r})]}{\delta\rho(\mathbf{r})} = \frac{\partial[\rho(\mathbf{r})\epsilon_{XC}(\mathbf{r})]}{\partial\rho(\mathbf{r})} \tag{2.8}$$

with

$$\epsilon_{XC}[\rho(\mathbf{r})] = \epsilon_{XC}^{\mathrm{hom}}(\mathbf{r}) \tag{2.9}$$

Generalized gradient approximation

To address the issue of inhomogeneities in the electronic density, the natural way is to carry out an expansion of the density in terms of the gradient and higher order derivatives. In general, the exchange-correlation energy can be written in the following form:

$$E_{XC}[\rho(\mathbf{r})] = \int \rho(\mathbf{r})\epsilon_{XC}[\rho(\mathbf{r}]F_{XC}[\rho(\mathbf{r}), \nabla\rho(\mathbf{r}), \nabla^2\rho(\mathbf{r}), \ldots]d\mathbf{r} \tag{2.10}$$

where the function F_{XC} is an enhancement factor that modifies the LDA expression according to the variation of the density in the vicinity of the considered point.

The second order gradient expansion corresponds to an expression of the type

$$E_{XC}[\rho(\mathbf{r})] = \int A_{XC}[\rho]\rho(\mathbf{r})^{4/3} + \int C_{XC}[\rho]|\nabla\rho(\mathbf{r})|^2/\rho(\mathbf{r})^{4/3}d\mathbf{r} \tag{2.11}$$

which is asymptotically valid for densities that vary slowly in space. The LDA retains only the first term of Eq. 2.11. A number of gradient expansions which have been named generalized gradient approximations (GGA) have been proposed. Here, two types of GGA functional BLYP and PBE are introduced.

In 1998, Becke proposed an exchange functional where the parameters were fitted to experimental molecular data [7].

$$\epsilon_X = \epsilon_X^{\mathrm{LDA}}\Big(1 - \frac{\beta}{2^{1/2}A_x}\frac{x^2}{1 + 6\beta x\mathrm{sinh}^{-1}(x)}\Big) \tag{2.12}$$

for $x = 2(6\pi^2)^(1/3)s = 2^{1/3}|\nabla\rho(\mathbf{r})|/\rho(\mathbf{r})^{\mathbf{4/3}}$. $A_x = (3/4)(3/\pi)^{1/3}$, and $\beta = 0.0042$.

This was complemented by a correlation functional derived also in 1988 by Lee, Yang, and Parr, thus giving rise to a very widely used combination called the BLYP functional [8]

$$\epsilon_C = -\frac{a}{1+d\rho^{-1/3}}\Big\{\rho + b\rho^{-2/3}\Big[C_F\rho^{5/3} - 2t_w + \frac{1}{9}\Big(t_w + \frac{1}{2}\nabla^2\rho\Big)\Big]e^{-c\rho^{-1/3}}\Big\} \tag{2.13}$$

where

$$t_w = \frac{1}{8}\Big(\frac{|\nabla^2\rho|}{\rho} - \nabla^2\rho\Big), \tag{2.14}$$

$C_F = 3/10(3\pi^2)^{2/3}$, $a = 0.04918, b = 0.132, c = 0.2533$, and $d = 0.349$. This correlation functional is not based on the LDA. It has been derived as an extension to other closed-shell systems of the Colle-Salvetti expression for the electronic correlation in helium [9].

In 1996, Perdew, Burke and Ernzerhof (PBE) proposed an exchange and correlation functional that satisfies as many formal properties and limits as possible, sacrificing only those deemed to be energetically less important [10].

The enhancement factor $F_X(\rho,\zeta,s)$ over the local exchange defined in Expression (2.10) depends on the local density ρ, magnetization density ζ (in the spin dependent case), and the demensionless density gradients $s = |\nabla\rho(\mathbf{r})|/(2k_F\rho)$. The chosen expression is

$$F_X(s) = 1 + \kappa - \frac{\kappa}{1+\mu s^2/\kappa} \tag{2.15}$$

where $\mu = \beta(\pi^2/3) = 0.21951$ and $\beta = 0.066725$ is related to the second order gradient expansion. PBE choose the κ=0.804. The correlation energy is written in a form similar to an earlier proposal of Perdew and Wang. It assumes the form

$$E_C^{\mathrm{GGA}} = \int \rho(\mathbf{r})\big[\epsilon_{\mathbf{C}}^{\mathrm{LDA}}(\rho,\zeta) + \mathbf{H}[\rho,\zeta,\mathbf{t}]\big]\,\mathbf{dr} \tag{2.16}$$

with

$$H[\rho,\zeta,t] = (e^2/a_0)\gamma\varphi^3\mathrm{In}\Big\{1 + \frac{\beta}{\gamma}t^2\Big[\frac{1+At^2}{1+At^2+A^2t^4}\Big]\Big\} \tag{2.17}$$

Here, $t = |\nabla\rho(\mathbf{r})|/2\varphi k_s\rho$ is a dimensionless density gradient, with k_s the Thomas-Fermi screening wave number, and $\varphi(\zeta) = [(1+\zeta)^{2/3} + (1-\zeta)^{2/3}]/2$ is spin-scaling factor. The quantity β is the same as for the exchange term $\beta = 0.066725$ and $\gamma = (1 - ln2)/\pi^2$=0.031091. The function A has the following form:

$$A = \frac{\beta}{\gamma}\left[e^{-\epsilon_C^{rmLDA}[\rho]/(\gamma\varphi^3/a_0)} - 1\right]^{-1} \tag{2.18}$$

So defined, the correlation correction term H satisfies the following properties:(a) it tends to the correct second-order gradient expansion in the slowly varying (high density) limit (t → 0), (b) it approaches minus the uniform electron gas correlation -ϵ_C^{LDA} for rapidly varying densities (t → ∞), thus making the correlation energy vanish in that limit, as required by the correlation hole sum rule, (c) it cancels the logarithmic singularity of ϵ_C^{LDA} in the high density limit, thus forcing the correlation energy to scale to a constant under uniform scaling of the density.

2.1.3 Pseudopotential approximation

It is well known that most physical properties of solids are dependent on the valence electrons to much greater extent than on the core electron. The pseudopotential approximation exploits this by removing the core electrons and by replacing them and the strong ionic potential by a weaker pseudopotential that acts on a set of pseudo wave functions rather than the true valence wave functions.

Norm-conserving pseudopotentials

The condition for the construction of norm-conserving pseudopotentials are the following:

(i) The eigenvalues of the pseudo-wave functions coincide with those of the all-electron wave functions for a chosen electronic configuration of the atom;

(ii) The radial pseudo-wave function $R_{PS}(r)$ is nodeless, and it is identical to the all-electron wave function outside a suitably chosen cutoff radius r_c:

$$R_{PS}(r) = \begin{cases} \widetilde{R}_{PS}(r) & r < r_c \\ R_{AE}(r) & r \geqq r_c \end{cases} \tag{2.19}$$

(iii) the norm of the true and pseudo-wave functions inside the pseudized region ($r < r_c$) is the same (norm-conservation condition):

$$\int_0^{r_c} |r\widetilde{R}_{PS}(r)|^2 dr = \int_0^{r_c} |r\widetilde{R}_{AE}(r)|^2 dr; \qquad (2.20)$$

(iv) The logarithmic derivatives of the all-electron and pseudo-wave function agree for $r \geqq r_c$.

The norm-conservation constraint guarantees that the pseudopotential is useful, not in every energy range, but at least in environments such that the eigenvalues do not depart significantly from the eigenvalues used in its constructions.

Ultrasoft pseudopotentials

The norm-conservation constraint is the main factor responsible for the hardness of some pseudepotentials, especially *p* states in first-row elements and *d* states in second-row transition metals, e.g. O $2p$ or Cu $3d$. For these states there is no core state of the same angular momentum to which they have to be orthogonal. Therefore, the all-electron wave function is nodeless and quite compressed compared to the other valence states, thus requiring a large number of plane waves to be represented accurately. Pseudization of this wave function does not help much because the pseudo-charge has to match the charge of the all-electron wave function and this latter is already nodeless.

The norm-conservation constraint is tightly linked to the concept of transferability through the sum rule.

$$-\frac{1}{2}\Big\{[rR^l(\epsilon, r)]^2 \frac{d}{d\epsilon}\frac{d}{dr}\ln R^l(\epsilon, r)]\Big\}_{r_c} = \int_0^{r_c} r^2[R^l(\epsilon, r)]^2 dr. \qquad (2.21)$$

This expression shows that the first order energy variation of the phase shifts is proportional to the norm of the wave function in the pseudized region. However, apart from respecting the transferability criterion embodies in (2.21), it is not strictly necessary that the norm of the all-electron and pseudo-wave functions coincide. Therefore, efforts directed towards the reduction of the plane wave cutoff should focus on relaxing the norm-conservation condition by generalizing the sum rule (2.21). The difference in the norm equation (2.20) is given by

$$Q_{ij} = \int_0^{R_c} dr Q_{ij}(\mathbf{r}), \qquad (2.22)$$

where

$$Q_{ij}(\mathbf{r}) = \psi_i^*(\mathbf{r})\psi_j(\mathbf{r}) - \phi_i^*(\mathbf{r})\phi_j(\mathbf{r}) \tag{2.23}$$

We now define the new functions

$$|\chi_p\rangle = (\epsilon_p - \hat{T} - V_{\mathrm{loc}})|\phi_p\rangle \tag{2.24}$$

where V_{local} is equal to the all-electron functions outside a cutoff radius $r > R_C$. For $r < R_c$, V_{local} is chose in some smooth fashion. If pseudofunctions ϕ_s are constructed from all-electron calculation at different energy ϵ_s, one can form the Matrix $B_{pq} = \langle\phi_p|\chi_q\rangle$. In terms of the functions $|\beta_q\rangle = \sum_p B_{pq}^{-1}|\chi_q\rangle$, the non-local potential operator can be written

$$V_0^{NL} = \sum_{p,q} B_{pq}|\beta_p\rangle\langle\beta_q|$$

In the calculation that uses an "ultrasoft pseudopotential" the solutions are orthonormalized according to

$$\langle\phi_p|S|\phi_q\rangle = \delta_{pq} \tag{2.25}$$

where

$$S = 1 + \sum_{r,s} q_{rs}|\chi_r\rangle\langle\chi_s| \tag{2.26}$$

$$q_{rs} = \int Q_{rs}(\mathbf{r})d\mathbf{r} \tag{2.27}$$

The generalized eigenvalue problem is

$$(\hat{T} + V^{loc} + V^{NL})|\varphi_p\rangle = \varepsilon_p S|\varphi_p\rangle \tag{2.28}$$

where

$$V^{NL} = V_0^{NL} + \sum_{p,q} \varepsilon_q Q_{pq}|\beta_p\rangle\langle\beta_q| = \sum_{p,q}(B_{pq} + \varepsilon_q Q_{pq})|\beta_p\rangle\langle\beta_q| \tag{2.29}$$

Fortunately, such a generalized eigenvalue problem is not a major complication with iterative method. The scattering properties are correct at each reference energy, in the sense that the logarithmic derivative match the AE one at that energy.

2.2 Momentum-space formalism

A momentum formalism is designed particularly for application with the self-consistent pseudo-potential method. In the present formalism, the total energy is obtained through band-structure calculation without additional integrations. Following the conventional density functional formalism in a pseudopotential framework, the total energy is given by

$$E_{total} = T + V + \int E_{xc}(\mathbf{r})dr^3 \tag{2.30}$$

where the total kinetic energy, T is

$$T = \sum_i \int \psi_i^*(\mathbf{r})(-\nabla^2)\psi_i(\mathbf{r})d^3r, \tag{2.31}$$

and the electronic potential energy, V is

$$\begin{aligned} V = &\sum_{i,\mu,l} \int \psi_i^*(\mathbf{r})U_{ps,l}(\mathbf{r}-\mathbf{R}_\mu)\hat{P}_l\psi_i(\mathbf{r})d^3r \\ &+ \frac{1}{2}\iint \frac{2\rho(\mathbf{r})\rho(\mathbf{r}')}{|\mathbf{r}-\mathbf{r}'|}d^3rd^3r' + \frac{1}{2}\sum_{\mu\neq\nu}\frac{2Z^2}{|\mathbf{R}_\mu-\mathbf{R}_\nu|} \end{aligned} \tag{2.32}$$

$$\begin{aligned} V = &\sum_{i,\mu,l} \int \psi_i^*(\mathbf{r})U_{ps,l}(\mathbf{r}-\mathbf{R}_\mu)\hat{P}_l\psi_i(\mathbf{r})d^3r \\ &+ \frac{1}{2}\iint \frac{2\rho(\mathbf{r})\rho(\mathbf{r}')}{|\mathbf{r}-\mathbf{r}'|}d^3rd^3r' + \frac{1}{2}\sum_{\mu\neq\nu}\frac{2Z^2}{|\mathbf{R}_\mu-\mathbf{R}_\nu|} \end{aligned} \tag{2.33}$$

and E_{XC} is exchange -correlation energy.

Let the momentum-space representations of wave function, the charge density, the inter-electronic Coulomb potential and the exchange-correlation Coulomb potential be denoted by $\psi(\mathbf{k_i}+\mathbf{G})$, $\rho(\mathbf{G})$, $V_{\text{coul}}(\mathbf{G})$ and $\mu_{\text{XC}}(\mathbf{G})$, respectively, where the $(\mathbf{G})$ are reciprocal lattice vectors.

$$\psi_i(\mathbf{r}) = \exp[i\mathbf{k}_i\cdot\mathbf{r}]u_i(\mathbf{r}) \tag{2.34}$$

$$= \exp[i\mathbf{k}_i\cdot\mathbf{r}]\sum_{\mathbf{G}}\psi(\mathbf{k}_i+\mathbf{G})\exp[i\mathbf{G}\cdot\mathbf{r}] \tag{2.35}$$

$$= \sum_{\mathbf{G}}\psi(\mathbf{k}_i+\mathbf{G})\exp[i(\mathbf{k}_i+\mathbf{G})\cdot\mathbf{r}] \tag{2.36}$$

$$\rho(\mathbf{r}) = \sum_{\mathbf{G}} \rho(\mathbf{G}) \exp[i\mathbf{G} \cdot \mathbf{r}] \tag{2.37}$$

$$V_{Coul}(\mathbf{G}) = \frac{8\pi\rho(\mathbf{G})}{G^2} \tag{2.38}$$

Using this Fourier representation, the Coulomb repulsion energy becomes:

$$\frac{1}{2}\iint \frac{2\rho(\mathbf{r})\rho(\mathbf{r}')}{|\mathbf{r}-\mathbf{r}'|} d^3r d^3r' = \frac{1}{2}\Omega \sum_{\mathbf{G}} V_{Coul}(\mathbf{G})\rho^*(\mathbf{G}) \tag{2.39}$$

The pseudopotential energy can be written as:

$$\begin{aligned}&\sum_{i,\mu,l} \int \psi_i^*(\mathbf{r}) U_{ps,l}(\mathbf{r}-\mathbf{R}_\mu)\hat{P}_l \psi_i(\mathbf{r}) d^3r \\ &\quad = \Omega\Big(\sum_{\mathbf{G}} S(\mathbf{G})U_{ps}(\mathbf{G})\rho(\mathbf{G}) + \sum_{i,l,\mathbf{G},\mathbf{G}'} \psi^*(\mathbf{k}_i+\mathbf{G})\psi(\mathbf{k}_i+\mathbf{G}')S(\mathbf{G}'-\mathbf{G})U'_{ps,l,\mathbf{k}_i^*+\mathbf{G},\mathbf{k}_i+\mathbf{G}'}\Big)\end{aligned} \tag{2.40}$$

where

$$\hat{P}_l = \sum_{m=l}^{l} |lm\rangle\langle lm| \tag{2.41}$$

and

$$S(\mathbf{G}) = \frac{1}{N}\int \rho(\mathbf{r}) \exp[i\mathbf{G}\cdot\mathbf{r}] dr^3 \tag{2.42}$$

$$= \frac{1}{N}\int \sum_i \delta(\mathbf{r}-\mathbf{r}_i) \exp[i\mathbf{G}\cdot\mathbf{r}] dr^3 \tag{2.43}$$

$$= \frac{1}{N}\sum_i \exp[i\mathbf{G}\cdot\mathbf{r}_i] dr^3 \tag{2.44}$$

From equations (2.30), (2.39) and (2.40) it can be seen that total energy reduces to

$$E_{total} = \Omega\Big(\sum_{i,\mathbf{G}} |\psi(\mathbf{k}_i + \mathbf{G}|^2(\mathbf{k}_i + \mathbf{G})^2 + \frac{1}{2}\sum_{\mathbf{G}} V_{Coul}(\mathbf{G})\rho^*(\mathbf{G}) \tag{2.45}$$

$$+ \frac{3}{4}\sum_{\mathbf{G}} \mu^*_{XC}(\mathbf{G})\rho(\mathbf{G}) + \sum_{\mathbf{G}} S(\mathbf{G})U^*_{ps}(\mathbf{G})\rho(\mathbf{G}) \tag{2.46}$$

$$+ \sum_{i,l,\mathbf{G},\mathbf{G}'} \psi^*(\mathbf{k}_i + \mathbf{G})\psi(\mathbf{k}_i + \mathbf{G}')S(\mathbf{G}' - \mathbf{G})U'_{ps,l,\mathbf{k}_i+\mathbf{G},\mathbf{k}_i+\mathbf{G}'}\Big) \tag{2.47}$$

$$+ \frac{1}{2}\sum_{\mu\neq\nu} \frac{2Z^2}{|\mathbf{R}_\mu - \mathbf{R}_\nu|} \tag{2.48}$$

To simplify equation (2.48), we multiply on the left of equation

$$\Big(-\nabla^2 + \sum_{\mu,l} U_{ps,l}(\mathbf{r} - \mathbf{R}_\mu)\hat{P}_l + \int \frac{2\rho(\mathbf{r}')}{|\mathbf{r} - \mathbf{r}'|}d^3r' + \mu_{xc}(\mathbf{r})\Big)\psi_i(\mathbf{r}) = \epsilon_i\psi_i(\mathbf{r}) \tag{2.49}$$

by $\psi_i^*(r)$, integrate over $\mathbf{r}$ and sum over i, and substitute the result into equation (2.30):

$$E_{total} = \sum_i \varepsilon_i - \frac{1}{2}\int\int \frac{2\rho(\mathbf{r})\rho(\mathbf{r}')}{|\mathbf{r} - \mathbf{r}'|}d^3rd^3r' - \frac{1}{4}\int \mu_{XC}(\mathbf{r})\rho(\mathbf{r})d^3r + \frac{1}{2}\sum_{\mu\neq\nu} \frac{2Z^2}{|\mathbf{R}_\mu - \mathbf{R}_\nu|} \tag{2.50}$$

$$= \sum_i \varepsilon_i - \Omega\Big[\frac{1}{2}\sum_{\mathbf{G}} V_{Coul}(\mathbf{G})\rho^*(\mathbf{G}) + \frac{1}{4}\sum_{\mathbf{G}} \mu^*_{XC}(\mathbf{G})\rho(\mathbf{G})\Big] + \frac{1}{2}\sum_{\mu\neq\nu} \frac{2Z^2}{|\mathbf{R}_\mu - \mathbf{R}_\nu|} \tag{2.51}$$

In practice, some mathematical manipulation are necessary to calculate E_{total} from equation (2.51) because $V_{\text{coul}}(0)$, $U_{\text{PS}}(0)$ and $\sum_{\mu\neq\nu} \frac{2Z^2}{|\mathbf{R}_\mu - \mathbf{R}_\nu|}$ are individually divergent quantities. First, we solve tha band-structure eigenvalue problem, equation (2.51) with $V_{\text{coul}}(0)$ and $U_{\text{PS}}(0)$ set equal to zero. For small $|\mathbf{G}|$ the local potential is :

$$U_{PS}(\mathbf{G}) = \frac{-8\pi Z}{\Omega_{at}G^2} + \alpha_1 + (\textit{higher terms in } G) \tag{2.52}$$

where the constant term α_1 is given by:

$$\alpha_1 = \lim_{G\to 0}[U_{ps}(G) + \frac{-8\pi Z}{\Omega_{at}G^2}] = (1/\Omega_{at}\int [U_{ps}(r) + (2Z/r)]d^3r \tag{2.53}$$

Another quality relevant to the total energy is β, defined from the expansion at small G of the charge density:

$$\rho(G) = (Z/\Omega_{at}) + \beta G^2 + (\textit{higher terms in } G) \tag{2.54}$$

From equation (2.38)

$$\beta = \lim_{G\to 0} \frac{\Omega_{at}}{8\pi}\Big(V_{Coul}(G) - \frac{8\pi Z}{\Omega_{at}G^2}\Big) = \frac{\Omega_{at}}{8\pi}\frac{1}{\Omega}\iint \frac{2[\rho(r) - (Z/\Omega_{at})]}{|\mathbf{r}-\mathbf{r}'|}d^3r d^3r' \tag{2.55}$$

The lattice (ion-ion) energy per atom is usually expressed assuming the average electronic potential is zero, as

$$\frac{1}{2}\sum_{\nu}{}' \frac{2Z^2}{|\mathbf{R}_\nu|} = \gamma_{Ewald} + \frac{1}{2}\lim_{G\to 0}\frac{8\pi Z}{\Omega_{at}G^2} \tag{2.56}$$

that is,

$$\gamma_{Ewald} \equiv \frac{1}{2}\sum_{\nu}{}' \frac{2Z^2}{|\mathbf{R}_\nu|} - \frac{1}{2}\lim_{G\to 0}\frac{8\pi Z}{\Omega_{at}G^2} = \frac{1}{2}\left(\sum_{\nu}{}' \frac{2Z^2}{\mathbf{R}_\nu} - \frac{1}{\Omega_{at}}\int \frac{2Z^2}{r}d^3r\right) \tag{2.57}$$

Combining equations (2.38), (2.52), (2.54) and (2.56), the energy per atom coming from the three divergent terms is

$$\lim_{G\to 0}\Omega_{at}\Big[\frac{1}{2}V_{Coul}(G)\rho(G) + U_{ps}(G)\rho(G)\Big] + \frac{1}{2}\sum_{\nu}{}' \frac{2Z^2}{|\mathbf{R}_\nu|} \tag{2.58}$$

$$= \lim_{G\to 0}\Big[\frac{\Omega_{at}}{2}\frac{8\pi[Z/\Omega_{at} + \beta G^2]^2}{G^2} \tag{2.59}$$

$$+ \Omega_{at}\Big(\frac{-8\pi Z}{\Omega_{at}G^2} + \alpha_1\Big)\Big(\frac{Z}{\Omega_{at}} + \beta G^2\Big) + \frac{1}{2}\frac{8\pi Z^2}{\Omega_{at}G^2}\Big] + \gamma_{Ewald} \tag{2.60}$$

$$= \alpha_1 Z + \gamma_{Ewald} \tag{2.61}$$

The final expression for the total energy per atom is

$$E_{total}(\textit{per atom}) = \frac{1}{N}\sum_i \varepsilon_i - \frac{1}{2}\Omega_{at}\sum_{G\neq 0} V_{Coul}(\mathbf{G})\rho(\mathbf{G}) \tag{2.62}$$

$$- \frac{1}{4}\Omega_{at}\sum_{\mathbf{G}} \mu_{XC}(\mathbf{G})\rho(\mathbf{G}) + \alpha_1 Z + \gamma_{Ewald} \tag{2.63}$$

2.3 Projector augumented waves (PAW) method

The projector augmented wave (PAW) methods, developed by Blöchl [11] and Kresse [12] is a powerful tool for performing electronic structure calculations within the framework of DFT. Like “ultrasoft” pseudopotential method, it introduces projectors and auxiliary localized functions. The PAW approach also defines a functional for the total energy that involves auxiliary functions and it uses advances in algorithms for efficient solution of the generalized eigenvalue problem like (2.28). However, the difference is that the PAW approach keeps the full all-electron wavefunction. Since the all-electron wavefunction varies rapidly near the nucleus, all integrals are evaluated as a combination of integrals of smooth functions extending throughout space plus localized contributions evaluated by radial integration over muffin-tin spheres. One can define a smooth part of a valence wavefunction $\widetilde{\phi}_i^v(\mathbf{r})$ and a linear transformation $\phi^v = \tau\widetilde{\phi}^v$ that relates the set of all-electron valence functions $\phi_j^v(\mathbf{r})$ to the smooth functions $\widetilde{\phi}_i^v(\mathbf{r})$. The transformation is assumed to ne unity except worth a sphere centered on the nucleus, $\tau = 1 + \tau_0$. For simplicity, we omit the superscript v, assuming that the ϕ_s are valence states, and the labels i, j. Adopting the Dirac notation, the expansion of the each smooth function $|\widetilde{\phi}\rangle$ in partial waves m within each sphere can be written,

$$|\widetilde{\phi}\rangle = \sum_m c_m |\widetilde{\phi}_m\rangle \tag{2.64}$$

with the corresponding all-electron functions,

$$|\phi\rangle = \tau|\widetilde{\phi}\rangle = \sum_m c_m |\widetilde{\phi}_m\rangle \tag{2.65}$$

Hence the full wavefunction in all space can be written

$$|\phi\rangle = |\widetilde{\phi}\rangle + \sum_m c_m \{|\phi_m\rangle - |\widetilde{\phi}_m\rangle\} \tag{2.66}$$

In the transformation τ is required to be linear, then the coefficients must be given by a projection i each sphere

$$c_m = \langle \widetilde{p}_m | \widetilde{\phi}\rangle \tag{2.67}$$

for some set of projection operators $\tilde{p}$. If the projection operator satisfy the biorthogonality condition,

$$\langle \widetilde{p}_m | \widetilde{\phi}_{m'}\rangle = \delta_{mm'} \tag{2.68}$$

then the one-center expansion $\sum_m |\widetilde{\phi}_m\rangle\langle\widetilde{p}_m|\widetilde{\phi}\rangle$ of the smooth function $\widetilde{\phi}$ equals $\widetilde{\phi}$ itself.

The difference from pseudo potentials is that the transformation τ still involves the full all-electron wavefunction

$$\tau = 1 + \sum_m \{|\phi_m\rangle - |\tilde{\phi}_m\rangle\}\langle\tilde{p}_{m'}| \tag{2.69}$$

Furthermore, the expressions apply equally well to core and valence states so that one can derive all-electron results by applying the expressions to all the electron states.

The general form of the PAW equations can be cast in terms of transformation (2.69). For any operator $\hat{A}$ in the original all-electron problem, one can introduce a transformed operator $\tilde{A}$ that operates on the smooth part of the wavefunctions

$$\tilde{A} = \tau^\dagger \hat{A} \tau = \hat{A} + \sum_{mm'} |\tilde{p}_m\rangle\{\langle\phi_m|\hat{A}|\phi_{m'}\rangle - \langle\tilde{\phi}_m|\hat{A}|\tilde{\phi}_{m'}\rangle\}\langle\tilde{p}_{m'}| \tag{2.70}$$

Furthermore, one can add to the right-hand side of (2.70) any operator of the form

$$\hat{B} - \sum_{mm'} |\tilde{p}_m\rangle\langle\phi_m|\hat{B}|\phi_{m'}\rangle\langle\tilde{p}_{m'}| \tag{2.71}$$

with no changes in the expectation values. For example, one can remove the nuclear Coulomb singularity in the equations for the smooth function, leaving a term that can be dealt with in the radial equations about each nucleus.

The expressions for physical quantities in the PAW approach follow from (2.69) and (2.70). For example, the density is given by calculating the expectation value of the real-space projection operator $|\mathbf{r}\rangle\langle\mathbf{r}|$

$$n(\mathbf{r}) = \tilde{n}(\mathbf{r}) + n^1(\mathbf{r}) - \tilde{n}^1(\mathbf{r}) \tag{2.72}$$

which can be written in terms of eigenstates labeled i with occupations f_i as

$$\tilde{n}(\mathbf{r}) = \sum_i f_i |\tilde{\phi}_i(\mathbf{r})|^2 \tag{2.73}$$

$$n^1(\mathbf{r}) = \sum_i f_i \sum_{mm'} \langle\tilde{\phi}_i|\tilde{\phi}_m\rangle \phi_m^*(\mathbf{r})\phi_{m'}(\mathbf{r})\langle\tilde{\phi}_{m'}|\tilde{\phi}_i\rangle \tag{2.74}$$

and

$$\tilde{n}^1(\mathbf{r}) = \sum_i f_i \sum_{mm'} \langle \tilde{\phi}_i | \tilde{\phi}_m \rangle \tilde{\phi}_m^*(\mathbf{r}) \tilde{\phi}_{m'}(\mathbf{r}) \langle \tilde{\phi}_{m'} | \tilde{\phi}_i \rangle \tag{2.75}$$

The last two terms are localized around each atom and the integrals can be done in spherical coordinates with no problems from the string variations near the nucleus, as in augmented methods. Section 13.2 is devoted to the PAW method and expressions for other quantities i molecules and condensed matter.

2.4 Hellmann-Feynman theorem

One of the beautiful theorems of physics is the “force theorem” called“Hellmann-Feynman theorem” for the force conjugate to any parameter in the hamiltonian. The important is that the force on a nucleus is given strictly in terms of the charge density, independent of the electron kinetic energy, exchange and correlation. The force conjugate to any parameter describing a system, such as position of a nucleus $\mathbf{R}_I$, can always be written

$$\mathbf{F}_I = -\frac{\partial E}{\partial \mathbf{R}_I} \tag{2.76}$$

The derivative can be written using first-order perturbation theory

$$-\frac{\partial E}{\partial \mathbf{R}_I} = -\langle \Psi | \frac{\partial \hat{H}}{\partial \mathbf{R}_I} | \Psi \rangle - \langle \frac{\Psi}{\partial \mathbf{R}_I} | \hat{H} | \Psi \rangle - \langle \Psi | \hat{H} | \frac{\Psi}{\partial \mathbf{R}_I} \rangle - \frac{\partial E_{II}}{\partial \mathbf{R}_I} \tag{2.77}$$

E_{II} of the final term is the electrostatic nucleus-nucleus (ion-ion) interaction, which is essential in the total energy calculation, but is only a classical additive term in theory of electronic structure. Using the fact that at the exact ground state solution the energy is extremal with respect to all possible variations of the wavefunction, it follows that the middle two terms in (2.77) vanish and the only non-zero terms come from the explicit dependence of the nuclear position.

$$-\frac{\partial E}{\partial \mathbf{R}_I} = -\langle \Psi | \frac{\partial \hat{H}}{\partial \mathbf{R}_I} | \Psi \rangle - \frac{\partial E_{II}}{\partial \mathbf{R}_I} \tag{2.78}$$

Because the Hellmann-Feynman theorem depends upon the requirement that the electronic states are at their variational minimum, it follows that there must be a continuum of “Hellmann-Feynman theorem” that corresponds to the addition of any linear variation in Ψ or n. Although such terms vanish in principle, they can have an enormous impact upon the accuracy and physical interpretation resulting formulas. The most relevant example in electronic structure is the case of core electrons: it is more physical and more accurate computationally to move the electron density in the core region along with the nucleus rather than holding the density strictly fixed.

Finally, there are drawbacks to the fact that expressions for the force theorem depends on the electronic wavefunction being an exact eigenstate. If the basis is not complete and it depends on the position of the nuclei, then there are additional terms that must be explicitly included so that the expression for the force given by the Hellmann-Feynman thorem is identical to the explicit derivative of the energy. Explicit expressions are given for use in independent-particle Kohn-Sham calculation.

Chapter 3

Dynanic properties of Liquid B_2O_3 under high pressure

3.1 Introduction

Crystalline boron oxide (B_2O_3) in ambient conditions has a trigonal unit cell in which each boron atom is coordinated to three oxygen atoms with strong single bonds forming a triangular BO_3 unit, and each oxygen atom is twofold coordinated to boron atoms [13, 14]. Under compression, a high-pressure phase appears at a pressure of about 6.5 GPa [15, 16]. This structure has an orthorhombic unit cell which consists of interconnected BO_4 tetrahedral units with six- and eight-membered rings. Each boron atom bonds to four oxygen atoms to form a distorted tetrahedron with one short bond and three longer bonds. This reflects the fact that one-third of the oxygen atoms are still twofold coordinated to boron atoms and the remaining have threefold coordination. In the vitreous state under pressures up to approximately 10 GPa, the coordination numbers are essentially unchanged, while the planarity of the BO_3 units is lost with increasing pressure [17]. Fourfold-coordinated boron atoms appear at higher pressures, and increase gradually with increasing pressure [17, 18].

It is well known that the transport properties of vitreous B_2O_3 (v-B_2O_3) are largely affected by the addition of alkali oxides [19]. Whereas the ionic conductivity of v-B_2O_3 without doped impurities is very small, it increases drastically with increasing the amount of alkali oxides added. Due to the presence of alkali elements as well as excess oxygen atoms, some of the covalent bonds between boron and oxygen atoms are broken. As a results, the network structure of v-B_2O_3, consisting of threefold-coordinated boron and twofold-coordinated oxygen atoms, is considerably modified by the doping [20]. It is, therefore, considered that these changes in the structural and bonding properties determine the transport properties of borate glasses, and enhance the ionic conductivity. In this way, the atomic dynamics in B_2O_3 is directly influenced by the modification of the networks of B-O bonds. Since the local structure of v-B_2O_3 is modified by compression as described above, its dynamic properties are expected to change with pressure.

Although many studies on the properties of crystalline and vitreous B_2O_3 have been reported, there are few on liquid B_2O_3. It is known that the local coordination around each atom remains the same upon melting at atmospheric pressure [21], i.e. boron atoms are predominantly threefold coordinated to oxygen atoms, and most of oxygen atoms bridge two adjacent boron atoms. However, the main difference of the liquid state from the crystalline and vitreous states comes from the fact that the covalent bonds must be rearranged with long-range atomic diffusion even without doped impurities. Recent first-principles investigation of the structural and bonding properties of liquid B_2O_3 [22] has revealed that, under ambient conditions, a non-bridging oxygen double bonded to a twofold-coordinated boron is always involved with atomic diffusion accompanied by rearrangement of the covalent bonds to reduce the formation energy of the overcoordination defects.

Concerning the effects of pressure on the structure of the liquid state, the position of the first x-ray diffraction peak has been measured as a function of pressure up to about 5 GPa [23]. The transport properties of liquid B_2O_3 under pressure have been studied by quenching experiments [24] and computer simulations [25] with an empirical interatomic potential. The former has revealed that the viscosity of the undercooled melt decreases with increasing pressure up to 8 GPa. The latter has shown that the diffusivity of atoms is enhanced by pressure below 15 GPa, as in other covalent liquids, such as SiO_2 and GeO_2 [26, 27]. It is, however, unclear how the rearrangement process of the covalent bonds is affected by compression.

In this paper, we investigate the structural, electronic, and dynamic properties of liquid B_2O_3 under pressure by *ab initio* molecular dynamics (MD) simulations with interatomic forces calculated quantum mechanically. So far, several first-principles studies for crystalline [28, 29, 30, 31] and vitreous [17, 32, 33] B_2O_3 under ambient and high pressures have been reported. However, the liquid properties under pressure have not been investigated yet from first principles. The purposes of our study are (1) to clarify the pressure-induced structural change in liquid B_2O_3, (2) to elucidate the effects of pressure on the electronic properties, and (3) to discuss the mechanism of atomic diffusion accompanied by the B-O bond exchange under pressure.

Although the major results for the dynamic properties have been reported earlier [34], this paper provides a full description of the calculated results including the structural and electronic properties.

3.2 Numerical details

We use a system of 120 (48B+72O) atoms in a cubic supercell was used under periodic boundary conditions. The equations of motion for atoms were solved via an explicit reversible integrator [35] with a time step of $\Delta t = 1.2$ fs. The atomic forces were obtained from the electronic states calculated using the projector-augmented-wave (PAW) method [11, 12] within the framework of density functional theory (DFT) in which the generalized gradient approximation (GGA) [10] was used for the exchange-correlation energy. The plane-wave cutoff energies are 30 and 200 Ry for the electronic pseudo-wave functions and the pseudo-charge density, respectively. The energy functional was minimized using an iterative scheme [36, 37].Projector functions are generated for the $2s$ and $2p$ states of B and O. The Γ point was used for Brillouin zone sampling. To obtain a liquid state, we began by carrying out an *ab initio* MD simulation for about 5 ps at a temperature of 5000 K starting from the low-pressure crystalline phase [13]. The temperature is selected to be high enough to make the system reach a completely disordered state without the effects of the initial configuration. Then, we decreased the temperature of the system gradually to a target temperature of 2500 K. the experimental data [38] obtained up to 1500 K. The temperature of 2500 K was chosen so as not only to be sufficiently high to maintain the liquid state even at the high pressures, but also in order to observe enough number of atomic-diffusion events to analyze the diffusion mechanism in a statistically meaningful way within a limited amount of simulation time. To determine the density of the liquid state under pressure, a constant-pressure MD simulation [39] was performed for 2.4 ps at each given pressure. Using the time-averaged density, the static and diffusion properties were investigated by MD simulations in the canonical ensemble [40, 41]. The time-averaged pressure [42, 43] was calculated at each density, and we obtained the density-pressure relation as shown in Fig. 3.1. The thermodynamic states investigated in this study cover a pressure range from 1.4 to 198.8GPa. The quantities of interest were obtained by averaging over $14.4 \sim 21.6$ ps to achieve good statistics after the initial equilibration, which takes at least 2.4 ps.

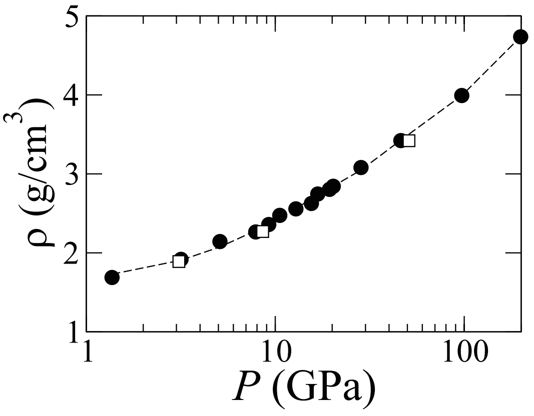

Figure 3.1: Pressure dependence of the density of liquid B_2O_3 at 2500 K (solid circles) and 3500 K (open squares).

3.3 Result and Discussion

3.3.1 Structure factor

Figure 3.2 shows the pressure dependence of the structure factors of liquid B_2O_3. The solid and dashed lines display the neutron and x-ray structure factors, $S_{\mathrm{n}}(k)$ and $S_{\mathrm{x}}(k)$, respectively. $S_{\mathrm{n}}(k)$ is calculated from the partial structure factors $S_{\alpha\beta}(k)$, shown in Fig. 3.3, with the neutron scattering lengths, and $S_{\mathrm{x}}(k)$ is obtained from $S_{\alpha\beta}(k)$ with the x-ray scattering factors. At pressures below 10 GPa, clear peaks exist at about $k = 1.6$ and 6.0 Å^{-1} in the profiles of $S_{\mathrm{n}}(k)$ and $S_{\mathrm{x}}(k)$. Note that the overall profile of $S_{\mathrm{n}}(k)$ in this pressure range is consistent with the experimental $S_{\mathrm{n}}(k)$ of the vitreous state [44]. While only $S_{\mathrm{x}}(k)$ has another peak at about 3.2 Å^{-1} at lower pressures, the corresponding peak grows in $S_{\mathrm{n}}(k)$ at higher pressures. With increasing pressure, the peak at about $k = 1.6$ Å^{-1} shifts to larger k, and merge into the peak at about $k = 3.2$ Å^{-1} in both $S_{\mathrm{n}}(k)$ and $S_{\mathrm{x}}(k)$. This shift of the peak at about $k = 1.6$ Å^{-1} in $S_{\mathrm{x}}(k)$ is in agreement with that observed by x-ray scattering experiments [23] up to 5 GPa. The peak at about $k = 6.0$ Å^{-1} also becomes higher at higher pressures.

Figure 3.3 shows the Ashcroft-Langreth partial structure factors $S_{\alpha\beta}(k)$. The pressure dependence of the profiles of $S_{\mathrm{n}}(k)$ and $S_{\mathrm{x}}(k)$ is well understood

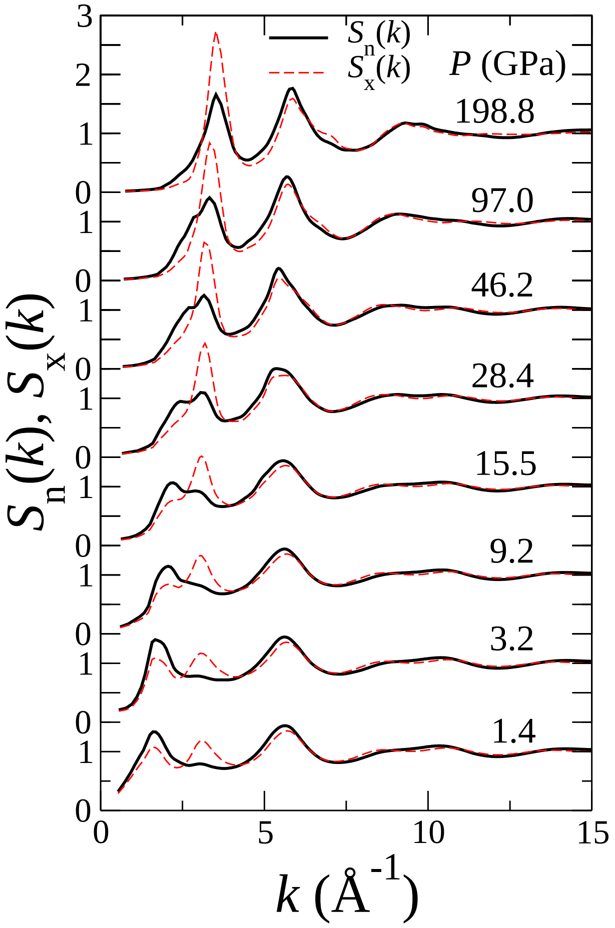

Figure 3.2: Pressure dependence of the total structure factors.The solid and dashed lines show the neutron and x-ray structure factors, $S_n(k)$ and $S_x(k)$, respectively.

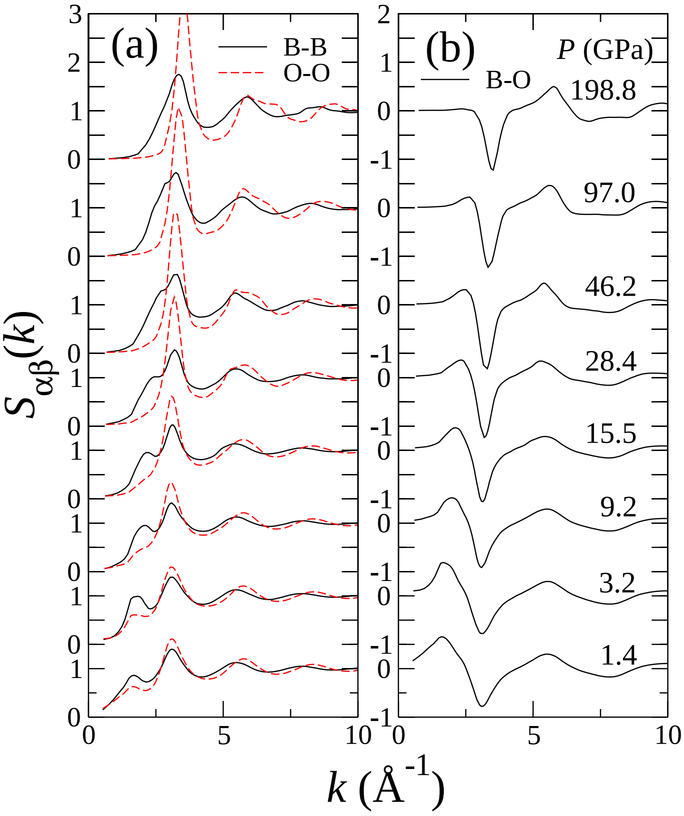

Figure 3.3: Pressure dependence of the partial structure factors $S_{\alpha\beta}(k)$. (a) The solid and dashed lines show $S_{\rm BB}(k)$ and $S_{\rm OO}(k)$, respectively. (b) The solid lines show $S_{\rm BO}(k)$.

from $S_{\alpha\beta}(k)$. At lower pressures, both $S_{\mathrm{BB}}(k)$ and $S_{\mathrm{OO}}(k)$ have the three peaks at about k = 1.6, 3.2, and 6.0 Å^{-1}, which give the corresponding peaks in $S_{\mathrm{n}}(k)$ and $S_{\mathrm{x}}(k)$. Because of the cancellation due to the existence of a negative dip in $S_{\mathrm{BO}}(k)$, no clear peak appears in $S_{\mathrm{n}}(k)$ around $k = 3.2$ Å^{-1}. With increasing pressure, the peak at about $k = 1.6$ Å^{-1} shifts to larger k in $S_{\mathrm{BB}}(k)$ and $S_{\mathrm{BO}}(k)$, while it disappears around 10 GPa in $S_{\mathrm{OO}}(k)$. At the wavevector of about k = 3.2 Å^{-1}, the peaks grow largely in $S_{\mathrm{BB}}(k)$ and $S_{\mathrm{OO}}(k)$, whereas the dip changes only a little in $S_{\mathrm{BO}}(k)$ with pressure. Therefore, the peaks of $S_{\mathrm{n}}(k)$ and $S_{\mathrm{x}}(k)$ grow at the corresponding k when the pressure increases. At higher pressures, the peak of $S_{\mathrm{OO}}(k)$ is much higher than that of $S_{\mathrm{BB}}(k)$.

3.3.2 Pair distribution function

The pressure dependence of the partial pair distribution functions $g_{\alpha\beta}(r)$ is displayed in Fig. 3.4. In $\mathrm{g_{BO}}(r)$, a sharp first peak exists at about 1.4 Å over all pressures, and becomes more asymmetric with increasing pressure. There are no homopolar bonds in liquid B_2O_3 under pressure, as $g_{\mathrm{BB}}(r)$ and $g_{\mathrm{OO}}(r)$ are zero over the r range of the first peak of $g_{\mathrm{BO}}(r)$ even at higher pressures. Note that a very broad peak appears around 3 Å in the profile of $g_{\mathrm{BO}}(r)$ when the pressure approaches about 30 GPa. This peak is related to the appearance of ring structures at higher pressures.

Figures 3.5(a)∼3.5(c) show the pressure dependence of the nearest-neighbor distances $r_{\alpha\beta}$ between α- and β-type atoms, which were obtained from the first-peak positions of $g_{\alpha\beta}(r)$. The pressure dependence of the average oxygen coordination number N_{BO} around B atoms is shown in Fig. 3.5(d). We calculated N_{BO} by the integration of $4\pi r^2 n_{\mathrm{O}} g_{\mathrm{BO}}(r)$ from r = 0 to 1.9 Å, which was determined with reference to the first-minimum position at the lowest pressure [45], where n_{O} is the number density of O atoms. The local bonding nature remains almost unchanged up to about 3 GPa, because all three $r_{\alpha\beta}$ and N_{BO} have nearly no pressure dependence. This means that the system is compressed by decreasing the empty space. For $P > 3$ GPa, N_{BO} increases gradually with increasing pressure, while r_{BO} still keeps its value constant up to about 10 GPa, which is consistent with the fact that the asymmetry of the first peak of $g_{\mathrm{BO}}(r)$ becomes larger. With further compression for $P > 10$ GPa, r_{BO} increases with pressure and has a maximum at about 50 GPa, while r_{BB} and r_{OO} decrease monotonically. Accompanying these changes, N_{BO} increases and approaches four at about 100 GPa, indicating that the local structure changes largely with pressure. Note that

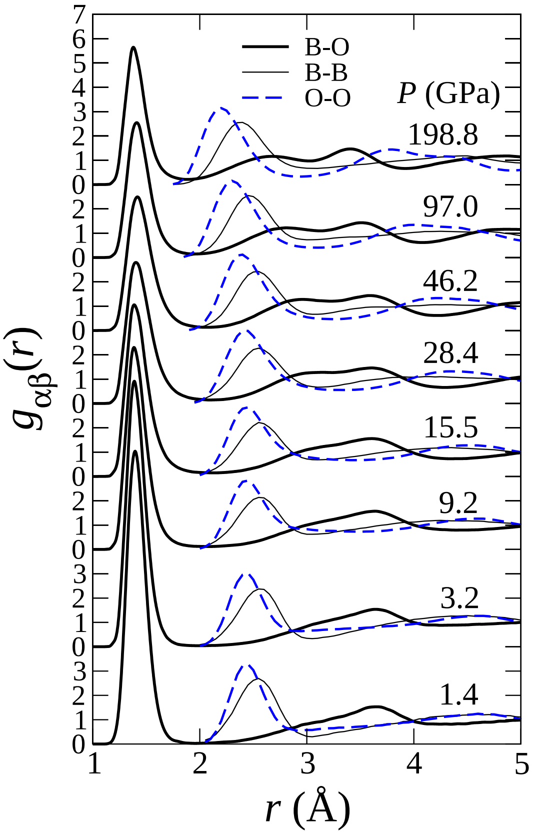

Figure 3.4: Pressure dependence of the partial pair distribution functions $g_{\alpha\beta}(r)$. The thick solid, thin solid, and thick dashed lines show $g_{\mathrm{BO}}(r)$, $g_{\mathrm{BB}}(r)$, and $g_{\mathrm{OO}}(r)$, respectively.

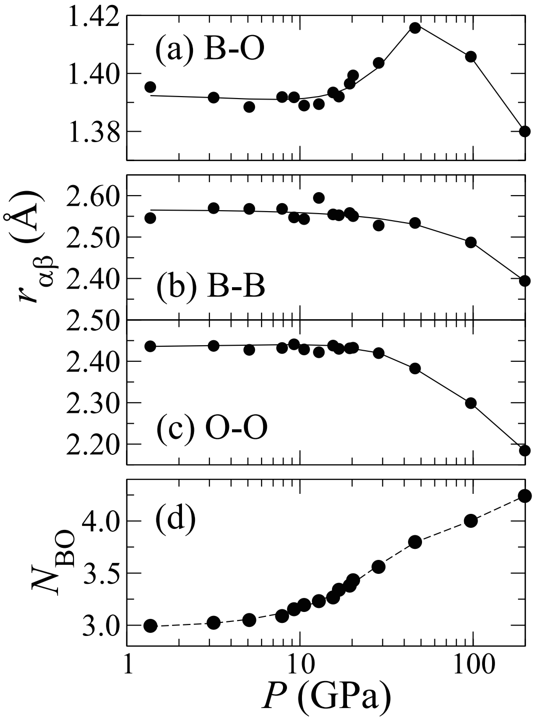

Figure 3.5: Pressure dependence of the nearest-neighbor distances $r_{\alpha\beta}$ for α-β = (a) B-O, (b) B-B, and (c) O-O. (d) Pressure dependence of the oxygen coordination number N_{BO} around boron atoms.

the difference between r_{BB} and r_{OO} becomes larger with increasing pressure. This implies that the average B-O-B and O-B-O angles change differently under compression, because r_{BB} and r_{OO} reflect these angles.

3.3.3 Coordination-number distribution

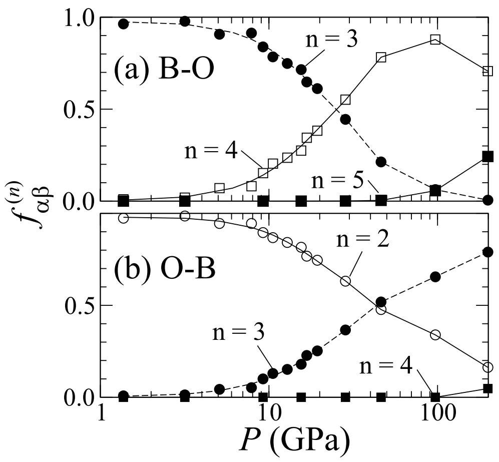

Figure 3.6: Pressure dependence of the coordination-number distribution $f_{\alpha\beta}^{(n)}$ for α-β = (a) B-O and (b) O-B.

Figure 3.6 shows the pressure dependence of the coordination-number distribution $f_{\alpha\beta}^{(n)}$, which is the ratio of $N_{\alpha\beta}^{(n)}/N_\alpha$, where $N_{\alpha\beta}^{(n)}$ is the number of α-type atoms coordinated to n β-type atoms and N_α is the total number of α-type atoms. To obtain $N_{\alpha\beta}^{(n)}$, the same cutoff distance $R = 1.9$ Å was used as in the calculation of N_{BO}. From Fig. 3.6, we see that liquid B_2O_3 consists mainly of BO_3 units connected by bridging O atoms under pressures up to about 3 GPa, and the BO_4 units increase gradually with increasing pressure for $P > 3$ GPa. $f_{\mathrm{BO}}^{(3)}$ and $f_{\mathrm{BO}}^{(4)}$ are exchanged for each other at about 25 GPa, while $f_{\mathrm{OB}}^{(2)}$ and $f_{\mathrm{OB}}^{(3)}$ are interchanged at a higher pressure of about 50 GPa. At about 100 GPa, the number of fourfold-coordinated B atoms approaches about 90 %, and about 5 % of B atoms have fivefold coordination. Under further compression up to about 200 GPa, one-fourth of the B atoms have fivefold coordination, and instead fourfold-coordinated B atoms decrease. Also, fourfold-coordinated O atoms appear under such high pressures, whereas twofold-coordinated O atoms still exist.

3.3.4 Electronic density of states

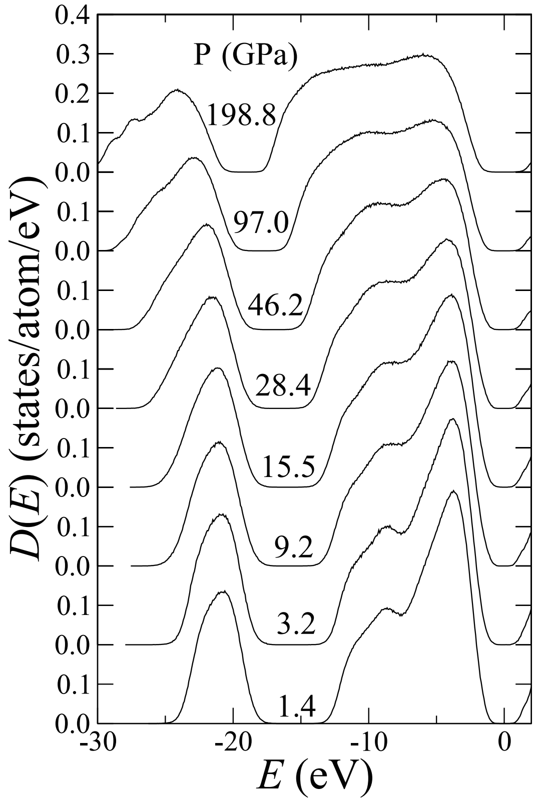

Figure 3.7: Pressure dependence of the electronic density of states $D(E)$.

Figures 6.6 and 3.8 show the pressure dependence of the total electronic density of states (DOS), $D(E)$, and the angular-momentum l dependent partial DOS, $D^l_\alpha(E)$, for α-type atoms, respectively. $D(E)$ is related to $D^l_\alpha(E)$ as $D(E) = \sum_\alpha c_\alpha \sum_l D^l_\alpha(E)$, where c_α is the number concentration of α-type atoms. In $D(E)$, there are two segments below the Fermi level ($E = 0$) over all pressures. The peak at around $E = -22$ eV shifts to lower energies and its energy range spreads with compression. Another segment consists of a large peak at about $E = -4$ eV and a shoulder around $E = -9$ eV at lower pressures. Note that the peak at about $E = -4$ eV originates from the lone-pair (LP) non-bonding p states around O atoms (see Fig. 3.8(b)). This peak becomes lower with increasing pressure, and its height are comparable to the shoulder at higher pressures, which means that some of the LP states are lost around O atoms. As was seen in Fig. 3.6, fourfold-coordinated B and threefold-coordinated O atoms increase with increasing pressure, and it

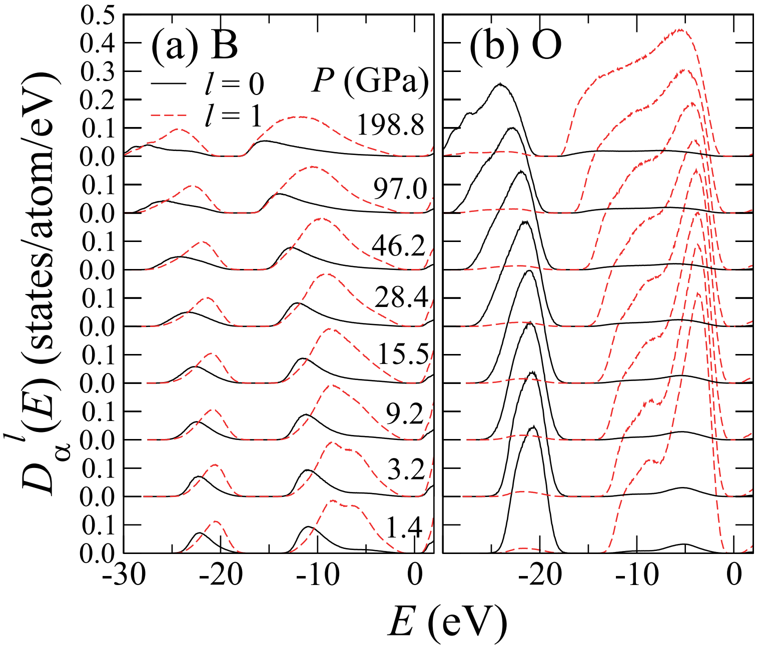

Figure 3.8: Pressure dependence of the angular-momentum l dependent partial electronic density of states $D_\alpha^l(E)$ for α = (a) B and (b) O atoms. The solid and dashed lines show $D_\alpha^l(E)$ for $l = 0$ and 1, respectively.

is, therefore, obvious that the electrons in the LP states are used to form new bonds between B and O atoms. The $2s$ and $2p$ orbitals are hybridized around B atoms at all pressures as shown in Fig. 3.8(a).

3.3.5 Bond-overlap population

We used population analysis [46, 47] to clarify the change in the bonding properties due to compression. By expanding the electronic wave functions in an atomic-orbital basis set, we obtained the overlap population O_{ij} between the ith and jth atoms and the gross charge Q_i for the ith atom. O_{ij} gives a semiquantitative estimate of the strength of the covalent-like bonding between atoms, and Q_i is a quantity that measures the ionicity of each atom. Figure 6.7 shows the time-averaged distribution $p_{\alpha\beta}(\overline{O})$ of the overlap populations $O_{i\in\alpha,j\in\beta}$. At all pressures, there is a clear peak at positive $\overline{O}$. This indicates that the covalent bond between B and O atoms is retained up to at least 200 GPa. The position of this peak is about $\overline{O} = 0.75$ up to 15.5 GPa, which reflects the σ-type covalent B-O bonds in the BO_3 units.

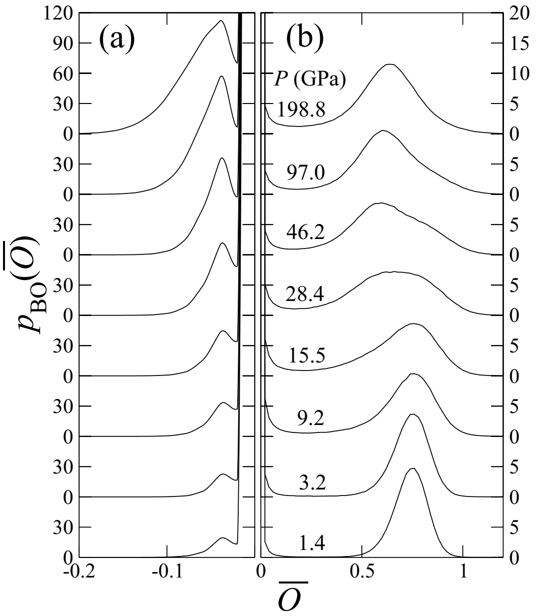

Figure 3.9: Pressure dependence of the distribution of the bond-overlap populations $p_{\mathrm{BO}}(\overline{O})$ for (a) $\overline{O} < 0$ and (b) $\overline{O} > 0$

It shifts to lower $\overline{O} = 0.6$ between 15.5 and 46.2 GPa, and is unchanged at pressures over 46.2 GPa. This pressure dependence of $p_{\alpha\beta}(\overline{O})$ reveals that the covalent B-O bonds become weak accompanying the increase of the BO_4 units. A clear peak also exists at negative $\overline{O}$, which comes from the interaction between the LP states around O atoms and the bonding states around B atoms. This peak grows with increasing pressure, reflecting the increase of interactions between O and B atoms.

3.3.6 Mulliken charge

Figure 3.10 shows the time-averaged distributions $q_\alpha(Q)$ of the gross charges $Q_{i\in\alpha}$ for α-type atoms. The peak positions of $q_{\mathrm{B}}(Q)$ and $q_{\mathrm{O}}(Q)$ shift to smaller and larger Q, respectively, with increasing pressure, i.e. the electrons around O atoms are transferred toward B atoms. This is consistent with the fact that the spatial distribution of the electrons that form the LP states around O atoms at lower pressures spreads to form new B-O bonds with increasing pressure. We can see that $q_{\mathrm{O}}(Q)$ has a shoulder besides the peak at higher pressures over 46.2 GPa; the shoulder originates from twofold-coordinated O atoms, while the peak comes from threefold-coordinated O

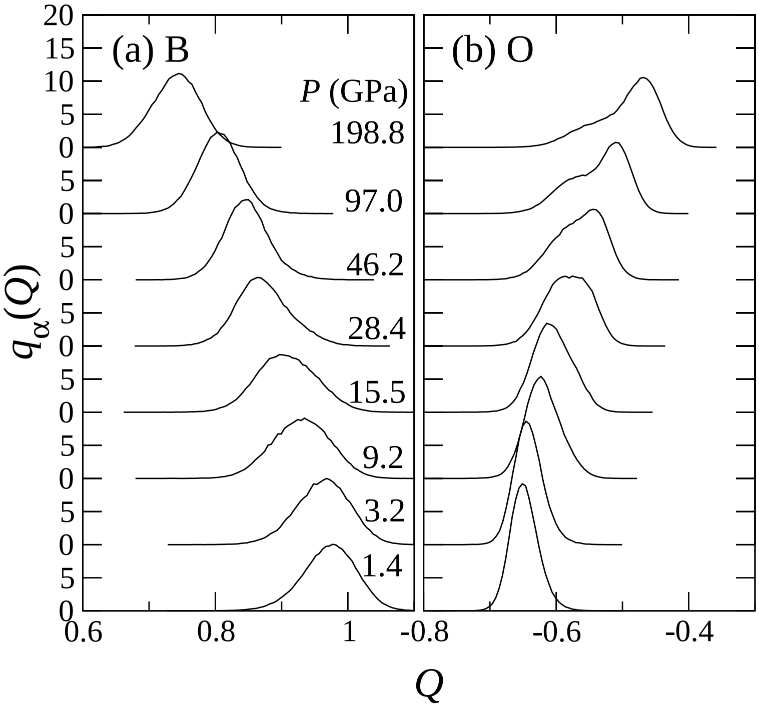

Figure 3.10: Pressure dependence of the distribution of the gross charges $q_\alpha(Q)$ for $\alpha =$ (a) B and (b) O.

atoms. On the other hand, $q_{\mathrm{B}}(Q)$ consists of only one peak for this pressure range, because almost all B atoms have fourfold coordination.

3.3.7 Diffusivity

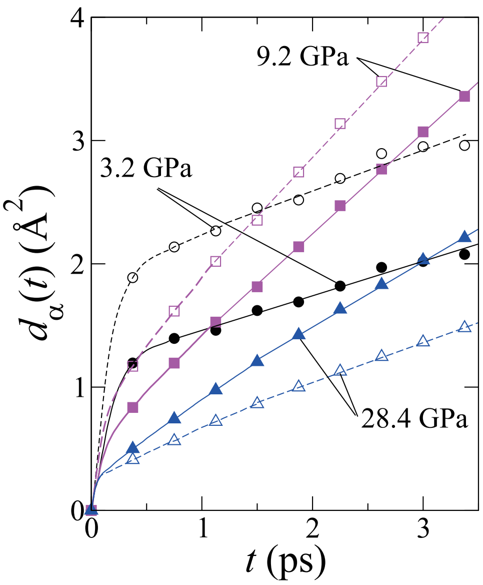

Figure 3.11: Pressure dependence of the mean-square displacements $d_\alpha(t)$. The solid and open symbols show $d_{\mathrm{B}}(t)$ and $d_{\mathrm{O}}(t)$, respectively.

The pressure dependence of the mean-square displacements $d_\alpha(t)$ is shown in Fig. 3.11, where the solid and open symbols show $d_{\mathrm{B}}(t)$ and $d_{\mathrm{O}}(t)$, respectively. $d_\alpha(t)$ is defined as $d_\alpha(t) = \sum_{i\in\alpha}\langle(r_i(t) - r_i(0))^2\rangle/N_\alpha$, where $r_i(t)$ is the position of the ith atom at time t and the brackets $\langle\cdots\rangle$ mean average with respect to the time origin $t = 0$. Both $d_{\mathrm{B}}(t)$ and $d_{\mathrm{O}}(t)$ have finite slopes, i.e. liquid states are reproduced by our simulations. Since the slopes of $d_{\mathrm{B}}(t)$ and $d_{\mathrm{O}}(t)$ increase when the pressure is increased from 3.2 to 9.2 GPa, we see that the atomic diffusion is enhanced by compression. Under further compression to 28.4 GPa, the slopes of $d_{\mathrm{B}}(t)$ and $d_{\mathrm{O}}(t)$ decrease. Note that the slope of $d_{\mathrm{B}}(t)$ is larger than that of $d_{\mathrm{O}}(t)$ at 28.4 GPa, while $d_{\mathrm{O}}(t)$ has a slightly larger slope at 3.2 and 9.2 GPa.

Figure 3.12 shows the diffusion coefficients D_α for $\alpha = \mathrm{B}$ and O atoms as a function of pressure. They were estimated from the slopes of $d_\alpha(t)$. Clearly, liquid B_2O_3 has a diffusion maximum around 10 GPa at the temperature of 2500 K. (See the open symbols. The temperature dependence will be discussed later.) In the pressure range of $P < 10$ GPa, both D_{B} and D_{O} increase with increasing pressure similarly to each other, which is consistent with the observed pressure dependence of the viscosity of the undercooled liquid [24]. While D_{O} has 10-20 % larger values than D_{B} under pressures up to about 10 GPa, D_{B} becomes more than two times larger than D_{O} when the pressure exceeds 20 GPa.

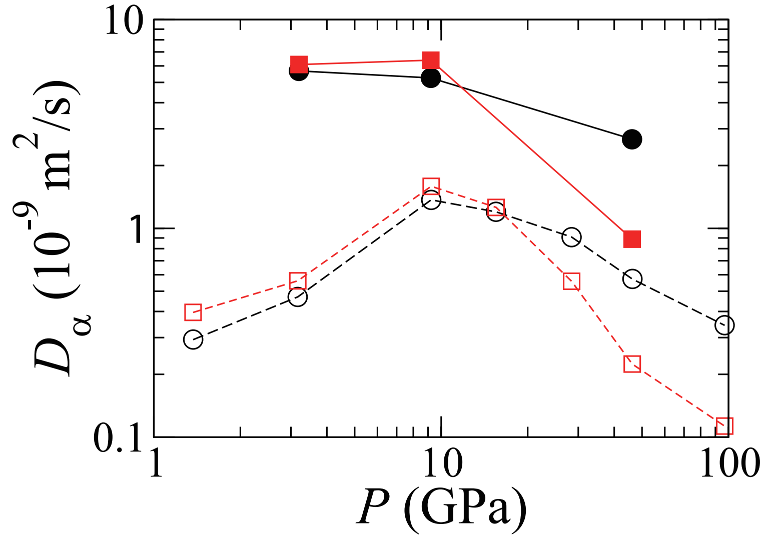

Figure 3.12: Pressure dependence of the diffusion coefficients D_α for $\alpha = \mathrm{B}$ (circles) and O (squares) atoms. The open and solid symbols indicate D_α at temperatures of 2500 and 3500 K, respectively.

3.3.8 Mechanism of atomic diffusion

As seen in the previous subsections, B atoms are mainly coordinated to three O atoms, and almost all O atoms bridge two adjacent B atoms as in the crystalline phase, even though atoms diffuse in the liquid state. It is obvious from the sharp first peak of $g_{\mathrm{BO}}(r)$ and the profile of $D^l_\alpha(E)$ that the covalent bonds between B and O atoms are preserved in liquid B_2O_3. These results are in good agreement with the recent experimental observations [21]. However, it is unclear how B-O bonds are exchanged with the diffusion of atoms in the liquid state while retaining the covalent bonds. To clarify the mechanism of atomic diffusion, we have investigated the time evolution of bonding nature by utilizing the population analysis [46, 47]. The bond-overlap populations, which give a semiquantitative estimate of the strength of the covalent-like bonding between atoms, were calculated as a function of time.

We found that one non-bridging O atom double bonded to a twofold-coordinated B atom is always involved with atomic diffusion accompanied by the B-O bond switching. A typical example of the generation of a non-bridging oxygen is shown in Fig. 3.13, where the time evolution of the bond-overlap populations associated with the B and O atoms of interest is displayed with snapshots of atomic configurations. In the atomic configuration at 0.01 ps (the bottom panel of Fig. 3.13), all B and O atoms displayed are threefold- and twofold-coordinated, respectively, to hetero atoms, i.e. there is no bond defect. As shown in the top panel of Fig. 3.13, $O_{\mathrm{B2-O2}}(t)$ begins to increase at about 0.04 ps, which means that a covalent bond is formed between B2 and O2. We can see this new B2-O2 bond in the snapshot at 0.07 ps. Due to the formation of the bond, both B2 and O2 are over-coordinated. Since the over-coordination is energetically unstable, one of the covalent bonds around the threefold-coordinated O2 atom is broken. It is seen that the bond-overlap population between B1 and O2, $O_{\mathrm{B1-O2}}(t)$, becomes almost zero for $t > 0.1$ ps, and the covalent bond between these atoms disappears in the snapshot at 0.13 ps. Note that B1 is coordinated to only two oxygens, while B2 is still over-coordinated. Finally, the covalent bond between B2 and O1 is broken, as $O_{\mathrm{B2-O1}}(t)$ is almost zero for $t > 0.16$ ps. While the threefold coordination of B2 is recovered, O1 is coordinated to only one boron B1, as displayed in the snapshot at 0.19 ps. In this way, the non-bridging O atom (O1) is generated with the twofold-coordinated B atom (B1). We see that there is a double bond between B1 and O1 because $O_{\mathrm{B1-O1}}(t)$ has higher values for $t > 0.16$ ps after the breaking of the B2-O1 bond. It should be noted that this process takes place in the participation of only two over-coordinated (one fourfold-coordinated B and one threefold-coordinated O) atoms, namely only one BO_4 unit.

After about 2 ps, the double bond between B1 and O1 disappears as shown in Fig. 3.14. First, the non-bridging O1 approaches to B3 to form a new covalent bond between them. We see that $O_{\mathrm{B3-O1}}(t)$ gradually increases for $t > 2.01$ ps as shown in the top panel of Fig. 3.14, and that O1 is bonded to B3 in the atomic configuration at 2.08 ps. It is also seen that $O_{\mathrm{B1-O3}}(t)$ increases for $t > 2.07$ ps, which means the formation of a covalent bond between B1 and O3 as displayed in the snapshot at 2.11 ps. In this configuration, O1 and B1 have the proper coordination numbers, and instead B3 and O3 are over-coordinated. As $O_{\mathrm{B3-O3}}(t)$ becomes nearly zero at about 2.12 ps, the B3-O3 bond is broken, and an atomic configuration with no bond defect is finally obtained as displayed in the snapshot at 2.18 ps. In

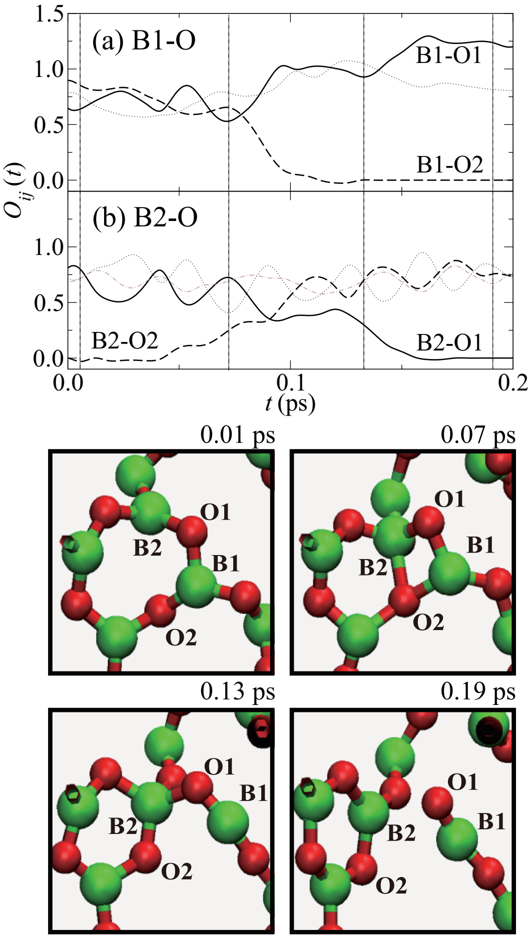

Figure 3.13: (Top panel) The time evolution of bond-overlap populations $O_{ij}(t)$ for (a) i = B1, $j \in$ O and (b) i = B2, $j \in$ O in the process of the formation of a non-bridging oxygen. The thick solid and thick dashed lines show $O_{ij}(t)$ associated with the B and O atoms of interest as denoted in the figures. The thin lines show $O_{ij}(t)$ between the B atoms of interest (labeled as 'B1' and 'B2') and their neighboring O atoms except O1 and O2. The vertical dotted lines show the times when the atomic configurations are displayed in the bottom panel. (Bottom panel) Atomic configurations at $t = 0.01$, 0.07, 0.13 and 0.19 ps. The large green and small red spheres show B and O atoms, respectively.

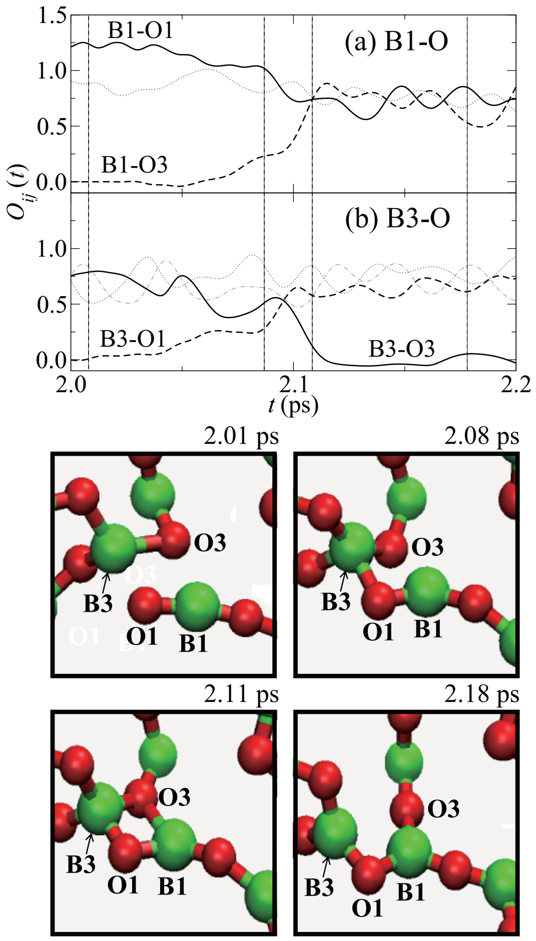

Figure 3.14: (Top panel) The time evolution of bond-overlap populations $O_{ij}(t)$ for (a) i = B1, $j \in$ O and (b) i = B3, $j \in$ O in the process of the disappearance of the non-bridging oxygen. The thick solid and thick dashed lines show $O_{ij}(t)$ associated with the B and O atoms of interest as denoted in the figures. The thin lines show $O_{ij}(t)$ between the B atoms of interest (labeled as 'B1' and 'B3') and their neighboring O atoms except O1 and O3. The vertical dotted lines show the times when the atomic configurations are displayed in the bottom panel. (Bottom panel) Atomic configurations at $t = 2.01$, 2.08, 2.11 and 2.18 ps. The large green and small red spheres show B and O atoms, respectively.

this process, two over-coordinated atoms (B3 and O3) are created as in the formation process of the non-bridging O atoms.

As displayed in Figs. 3.13 and 3.14, the B-O bonds are exchanged with the formation of the under-coordinated O and B atoms (O1 and B1) in liquid B_2O_3. It seems to be possible that the covalent bonds are exchanged without the formation of such under-coordinated atoms as in the relaxation process suggested for vitreous B_2O_3 [48]. It is, however, necessary to generate two BO_4 groups with sharing two O atoms, namely four over-coordinated atoms (two over-coordinated B and two over-coordinated O), in this relaxation process. The energy necessary to create two BO_4 groups is higher than that for the formation process of the non-bridging O atoms, which requires only one BO_4 group as found in our simulations. We consider that this is the reason why most of the diffusion processes take place accompanied by the under-coordinated atoms in liquid B_2O_3.

The intermediate defect structures with the non-bridging O atoms double bonded to twofold-coordinated B atoms are energetically unstable, and therefore they are eventually recovered as shown in Fig. 3.14. It should be mentioned that the structure of liquid B_2O_3 is rather porous as in solids. Due to the existence of wide void space, the non-bridging oxygens cannot be bonded to other B atoms immediately after their formation. So the non-bridging oxygens diffuse while keeping the double bonds for a period of time, namely 1.7 ps on average, with the shortest time being 0.8 ps and the longest 4.3 ps.

Another important diffusion event accompanied by the covalent-bond switching is shown in Fig. 3.15, where covalent bonds are exchanged around the intermediate defect structure with the non-bridging O atom while keeping the double bond between the under-coordinated O and B atoms (O1 and B1 in the figure). As seen in the top panel of Fig. 3.15, around B1 atom, initially $O_{\mathrm{B1-O4}}(t)$ and $O_{\mathrm{B1-O5}}(t)$ are almost zero and finite, respectively, for $t < 0.05$ ps, they cross each other at about 0.11 ps, and finally $O_{\mathrm{B1-O5}}(t)$ becomes almost zero while $O_{\mathrm{B1-O4}}(t)$ is finite for $t > 0.14$ ps. This means that a covalent-bond exchange occurs around B1 atom: the covalent bond between B1 and O5 is broken, and at almost the same time a new bond is formed between B1 and O4 (see the atomic configurations in the bottom panel of Fig. 3.15). In the same say, another covalent-bond exchange occurs around B4 atom: the B4-O4 bond is broken, and the B4-O5 bond is formed, as seen from the time evolution of $O_{\mathrm{B4-O4}}(t)$ and $O_{\mathrm{B4-O5}}(t)$. Note that the coordination number of each atom is unchanged before and after this event. Especially the double bond between B1 and O1 is retained while switching the covalent bonds, as $O_{\mathrm{B1-O1}}(t)$ keeps high values. Since the

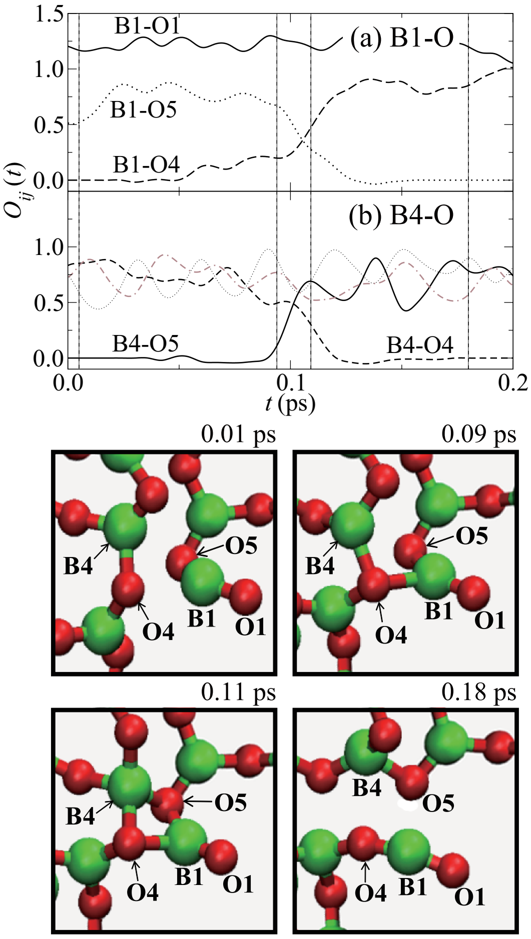

Figure 3.15: (Top panel) The time evolution of bond-overlap populations $O_{ij}(t)$ for (a) i = B1, $j \in$ O and (b) i = B4, $j \in$ O in a bond-switching process near the non-bridging oxygen. The thick solid, thick dashed, and thick dotted lines show $O_{ij}(t)$ associated with the B and O atoms of interest as denoted in the figures. The thin lines show $O_{ij}(t)$ between the B atoms of interest (labeled as 'B1' and 'B4') and their neighboring O atoms except O1, O4, and O5. The vertical dotted lines show the times when the atomic configurations are displayed in the bottom panel. (Bottom panel) Atomic configurations at $t = 0.02$, 0.09, 0.11 and 0.18 ps. The large green and small red spheres show B and O atoms, respectively.

non-bridging oxygen (O1) is always away from any atoms, it cannot be involved in these concerted bond exchanges. The pressure-induced diffusion enhancement must be related to the weakening of the covalent-like interaction between atoms accompanying the increase in the coordination number, as in other covalent liquids [26, 27]. In fact, we found that, in liquid B_2O_3 under pressures over 3 GPa, long-range atomic diffusion occurs by the usual concerted reactions as shown in Fig. 3.16, while the nonbridging O atoms are always involved in diffusion processes at lower pressures [22]. In Fig. 3.16, the time evolution of the bond-overlap populations $O_{ij}(t)$ associated with the B and O atoms of interest is displayed with snapshots of atomic configurations. As displayed in the snapshot at 0.09 ps, two BO_4 groups are generated as an intermediate by forming two new B-O bonds between adjoining BO_3 units, in contrast to the fact that only one BO_4 group is required to produce the nonbridging O atoms. The concerted reactions occur more frequently under higher pressures, which will result from the covalent-bond weakening due to the compression, and will enhance the atomic diffusion. We also observed that the reactions with the nonbridging O atoms decrease with increasing pressure and almost disappear for $P > 10$ GPa.

The concerted reactions as well as the reactions with the nonbridging O atoms involve equal numbers of B and O atoms, and therefore D_{B} and D_{O} would depend similarly to each other on pressure up to about 10 GPa as seen in Fig. 3.12. D_{O} has 10-20 % larger values than D_{B}, which may be due to the lower coordination number of O atoms [34]. The appearance of diffusion maximum is not surprising but quite natural in the covalent liquids. It is, however, unusual that the diffusivity of O atoms is reduced more quickly than that of B atoms with compression above 10 GPa. The important point is that, under pressures over 20 GPa, the number of fourfold-coordinated B atoms is much larger than that of threefold-coordinated B atoms, and, on the other hand, both twofold- and threefold-coordinated O atoms exist.

To consider the anomalous diffusive properties of liquid B_2O_3 under pressure, it is worth noting that the number of fourfold-coordinated B atoms becomes larger than that of threefold-coordinated B atoms, as shown in Fig. 3.6(a), when D_{B} and D_{O} are interchanged. We focused on diffusion processes associated with fourfold-coordinated B atoms. A typical example is shown in Fig. 3.17, where the time evolution of the bond-overlap populations, $O_{ij}(t)$, associated with the B and O atoms of interest is displayed with snapshots of atomic configurations. $O_{ij}(t)$ yields a semiquantitative estimate of the strength of the covalent-like bonding between atoms [46, 47]. In the beginning of this process, the B atom labeled 'B1' has fourfold coordination. The atomic configuration at 0.02 ps (and also at 0.17 ps) shows

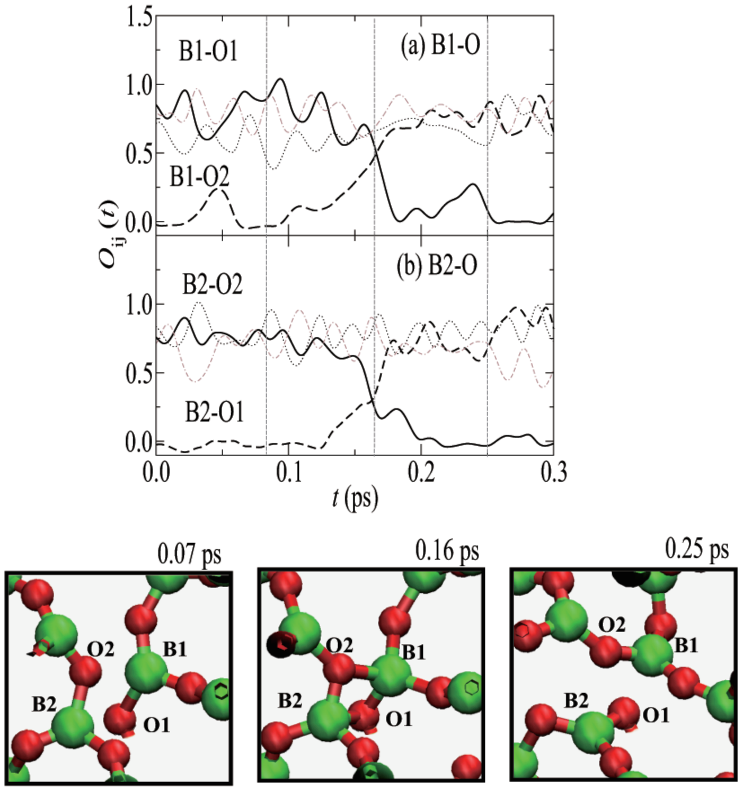

Figure 3.16: (Top panel) Time evolution of the bond-overlap populations $O_{ij}(t)$ for (a) i = B1, $j \in$ O and (b) i = B2, $j \in$ O in the process of bond switching with two BO_3 groups observed at 9.2 GPa. The thick solid and thick dashed lines show $O_{ij}(t)$ associated with the B (labeled as 'B1' and 'B2') and O (labeled as 'O1' and 'O2') atoms of interest. The thin lines show $O_{ij}(t)$ between the B1 or B2 atoms and their neighboring O atoms except O1 and O2. (Bottom panel) Atomic configurations at $t = 0.00$, 0.09 and 0.18 ps. The large and small spheres show B and O atoms, respectively.

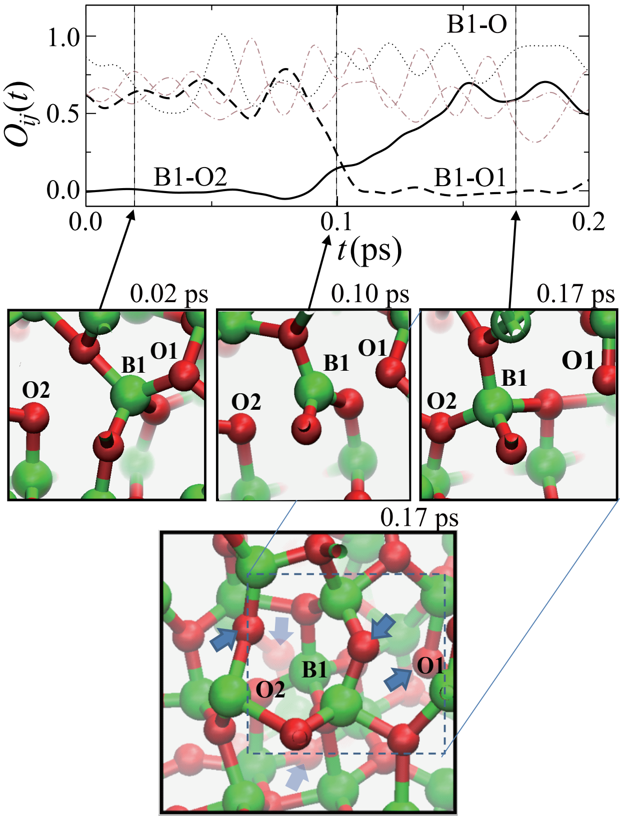

Figure 3.17: (Top panel) The time evolution of bond-overlap populations $O_{ij}(t)$ for i = B1, $j \in$ O in the diffusion process observed at 46.2 GPa. The thick solid and dashed lines show $O_{ij}(t)$ associated with the B and O atoms of interest. The thin lines show $O_{ij}(t)$ between the B atom of interest (labeled 'B1') and their neighboring O atoms except O1 and O2. (Middle panel) Atomic configurations at $t = 0.02$, 0.10, and 0.17 ps. The large and small spheres show B and O atoms, respectively. (Bottom panel) Extended view of the atomic configuration at $t = 0.17$ ps. The arrows denote O atoms that are twofold coordinated to B atoms.

that fourfold-coordinated B atoms have a tetrahedral arrangement, which demands sp^3 hybridization around them. As displayed in the top panel of Fig. 3.17, $O_{\mathrm{B1-O1}}(t)$ begins to decrease at about 0.08 ps and almost vanishes for $t > 0.11$ ps. This time change means that the covalent bond between B1 and O1 is broken within 0.03 ps. On the other hand, $O_{\mathrm{B1-O2}}(t)$ increases gradually between 0.08 and 0.15 ps, indicating that a covalent bond is formed between B1 and O2, taking 0.07 ps to form. As shown in the atomic configuration at 0.10 ps, the B1 atom has threefold coordination with a planar arrangement before the formation of the new B1-O2 bond is complete. This planar configuration is considered to be rather stable with sp^2 hybridization around the B1 atom, as seen regularly at pressures lower than 10 GPa. In this way, one of the B-O bonds is broken quickly, and a new B-O bond is formed gradually when B atoms move between the fourfold-coordinated sites.

In the diffusion process shown in Fig. 3.17, twofold-coordinated O atoms, toward which fourfold-coordinated B atoms move, are necessary as B1 moves toward O2. Note that O2 has twofold-coordination before B1 bonds to it. As shown in Fig. 3.6(b), twofold coordinated O atoms exist even at high pressures. In addition, several twofold-coordinated O atoms exist around each B atom, at least at about 50 GPa (see the bottom panel in Fig. 3.17). These facts indicate that this diffusion process occurs rather frequently, and that B atoms can diffuse fairly easily. On the other hand, for the concerted reaction involving the migration of O and B atoms, threefold-coordinated B and twofold-coordinated O atoms are necessary. However, the number of threefold-coordinated B atoms decreases rapidly with increasing pressure for $P > 20$ GPa, which means that the concerted reaction is suppressed at such high pressures. This is why D_{O} decreases rapidly with increasing pressure.

3.3.9 Temperature dependence

In order to investigate the effects of temperature on the properties of liquid B_2O_3 under pressure, some MD simulations were carried out at a higher temperature of 3500 K. Figure 3.18 shows the pressure dependence of $g_{\alpha\beta}(r)$ at 3500 K. From the comparison of each profile with the corresponding $g_{\alpha\beta}(r)$ at 2500 K (Fig. 3.4), we see that the first peaks of all $g_{\alpha\beta}(r)$ become broader because of the larger thermal motion of atoms. However, the peak positions and the average coordination numbers are almost unchanged. In this sense, the effects of the increase of pressure to ~ 50 GPa on the static structure would be more important than those of the increase of temperature from 2500 to 3500 K.

The pressure dependence of the diffusion coefficients D_α at 3500 K is

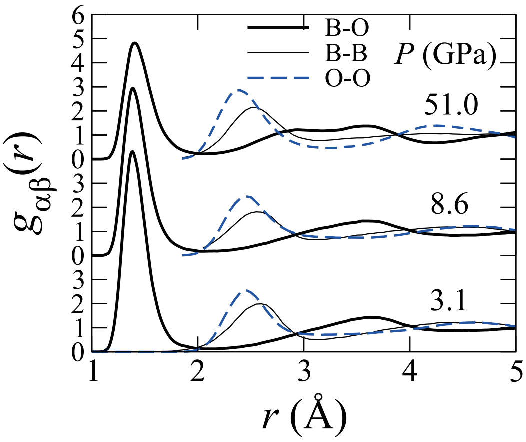

Figure 3.18: Pressure dependence of the partial pair distribution functions $g_{\alpha\beta}(r)$ at a high temperature of 3500 K. The thick solid, thin solid, and thick dashed lines show $g_{\mathrm{BO}}(r)$, $g_{\mathrm{BB}}(r)$, and $g_{\mathrm{OO}}(r)$, respectively.

shown in Fig. 3.12 together with that at 2500 K. The maximum behavior of the diffusivity becomes weaker or disappears when the temperature is higher. A similar temperature dependence has been seen in liquid SiO_2 [26]. Note that the diffusivity of O atoms becomes much lower than that of B atoms with increasing pressure even at 3500 K. This is because B atoms will eventually have fourfold coordination with compression, regardless of temperature.

3.4 Summary

We have investigated the structural, bonding, and dynamic properties of liquid B_2O_3 under pressures up to about 200 GPa by *ab initio* molecular dynamics simulations. The effects of compression on the static structure have been discussed based on the pressure dependence of the structure factors, the pair distribution functions, the nearest-neighbor distances, and the coordination-number distribution. The structure consists mainly of planar BO_3 units up to about 3 GPa, and the number of tetrahedral BO_4 units increases gradually under further compression. The number of fourfold-coordinated B atoms reaches a maximum of about 90 % at about 100 GPa. Threefold-coordinated B atoms almost disappear at pressures over 50 GPa, whereas twofold-coordinated O atoms still exist even under such high pressures. The bonding properties at each pressure have been examined by population analysis. It has been seen from the distribution of the bond-overlap populations that the covalent bonds weaken due to the structural change from BO_3 to BO_4 units. The pressure dependence of the mean-square displacements has shown that the diffusion maximum occurs at about 10 GPa when the temperature is relatively low. Regardless of temperature, the diffusivity of O atoms will eventually becomes much smaller than that of B atoms under higher pressures, while the former is slightly larger than the latter at lower pressures. This is because the number of threefold-coordinated B atoms decreases rapidly with pressure, and the concerted reaction is suppressed.

Chapter 4

Transport properties of liquid SiO_2, GeO_2 and $SrGeO_3$

4.1 Introduction

Covalent liquids have been intensively studied because of geological interest, since they are closely related with igneous processes in the Earth. Especially, transport properties of covalent liquids under pressure are very interesting in the sense that an unexpected pressure dependence is observed. For a number of covalent liquids, such as SiO_2, GeO_2, silicates and germanates, have abnormal behavior of the viscosity, i.e. the viscosity significantly drops with pressure [2, 3]. This anomalous behavior of the viscosity is considered to be related to the atomic diffusion in the liquids under pressure. It is, therefore, of particular interest to investigate the pressure dependence of the microscopic diffusion mechanism in covalent liquids. Recently, molecular dynamics (MD) studies of liquid GeO_2 under pressure have been reported [49]. It was shown that the diffusivity of atoms increases with pressure, as in other covalent liquids, such as SiO_2 [26] and B_2O_3[50]. It is, however, unclear how the rearrangement process of the covalent bonds is affected by compression. Because the calculated results obtained by empirical potentials depend on the choice of the potential form, theoretical investigations based on first-principles theory would be needed to clarify the microscopic mechanism of atomic diffusion in liquid state.

In this paper, we report on a detailed investigation of atomic diffusion in liquid SiO_2, GeO_2 and $SrGeO_3$ by *ab initio* MD simulations with interatomic forces calculated quantum mechanically in the framework of the density-functional theory (DFT). The SiO_2 crystal structure is α-quartz phase conists of SiO_4 tetrahedral local units. The structure of crystalline GeO_2 and $SrGeO_3$ also is well known. The high temperature phase of crystalline GeO_2 is α-quartz type structure which is based on corner-sharing GeO_4 tetrahedron [51]. In the structure of crystalline $SrGeO_3$, Ge_3O_9 molecules form layers and Sr atoms exist between the layers [52]. The coordination number of Ge to O atoms is four in both crystalline GeO_2 and $SrGeO_3$. In the $SrGeO_3$ the molecule has two oxygen sites, the bridging oxygen and non-bridging oxygens sites, which have two and one neighboring Ge atoms, respectively. The local structures of these materials remain the same even in the liquid state, i.e. there exist non-bridging oxygens, in liquid $SrGeO_3$ while there are few non-bridging oxygens in liquid GeO_2. For this reason, it is expected that the mechanisms of atomic diffusion in these liquids are different from each other. The purpose of our study is to clarify the microscopic mechanism of atomic diffusion in tetrahedral covalent liquids such as liquid SiO_2, GeO_2 and $SrGeO_3$. We discuss how Si-O or Ge-O bonds are exchanged accompanying the diffusion of atoms and how the diffusion mechanisms change with pressure.

4.2 Numerical details

The electronic states are calculated using the projector-augmented-wave (PAW) method [11, 12] within the framework of the density functional theory (DFT) in which the generalized gradient approximation (GGA) [10] is used for the exchange-correlation energy. The plane-wave cutoff energies are 30 and 200 Ry for the electronic pseudo-wave functions and the pseudo-charge density, respectively. The energy functional is minimized using an iterative scheme [36, 37]. The Γ point is used for Brillouin zone sampling. As the valence electrons, we include the $4s$, $4p$ and $5s$ electrons of Sr, $3s$ and $3p$ electrons of Si, $4s$ and $4p$ electrons of Ge and $2s$ and $2p$ electrons of O. Other electrons in the lower energy electronic states of each atom are treated with the frozen-core approximation. We use two systems of 120 (24Sr+24Ge+72O) atoms for $SrGeO_3$ and 144 (48Ge or Si +96O) atoms for SiO_2 and GeO_2 in a cubic supercell under periodic boundary conditions. Using the Nosé-Hoover thermostat technique [40, 41], the equations of motion are solved via an explicit reversible integrator [35] with a time step of $\Delta t = 1.2$ fs. To obtain a liquid state, we begin by carrying out an *ab initio* MD simulation for about 5 ps at a temperature of 4000 K starting from the crystalline structure [51, 52]. The temperature is selected to be high enough to make the system reach a completely disordered state without the effects of the initial configuration. Then, we decrease the temperature of the system gradually to a target temperature of 3000 K for SiO_2 and 2500 K for GeO_2 and $SrGeO_3$. The number density is determined from zero-pressure condition. The target temperature we have chosen is rather high in order to observe enough number of atomic-diffusion events to analyze the diffusion mechanism in a statistically meaningful way within a limited amount of simulation time. Note that the temperature dependence of physical quantities is not discussed in this paper, and conclusions derived are independent of the selected temperature. The simulation time 7.2 ps, is long enough to achieve good statistics.

4.3 Results of liquid SiO_2

4.3.1 Coordination number dustribution

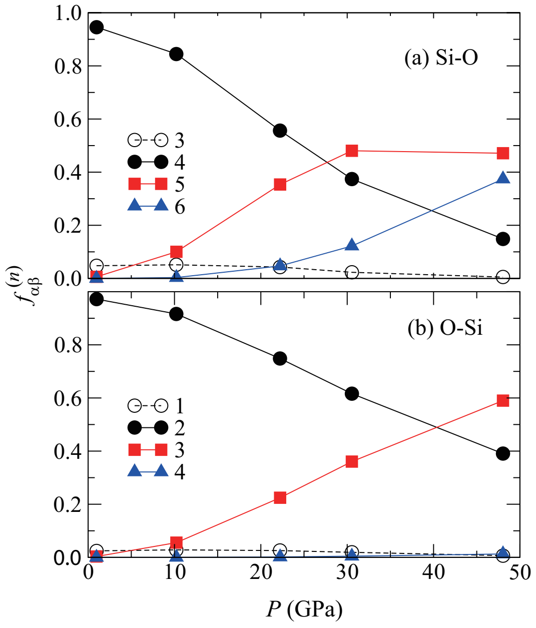

Figure 4.1: Pressure dependence of the coordination-number distribution $f_{\alpha\beta}^{(n)}$ for α-β = (a) Si-O and (b) O-Si.

Figure 4.1 shows the pressure dependence of the coordination-number distribution $f_{\alpha\beta}^{(n)}$ of liquid SiO_2, which is the ratio of $N_{\alpha\beta}^{(n)}/N_\alpha$, where $N_{\alpha\beta}^{(n)}$ is the number of α-type atoms coordinated to n β-type atoms and N_α is the total number of α-type atoms. To obtain $N_{\alpha\beta}^{(n)}$, the same cutoff distance $R = 2.1$ Å was used as in the calculation of N_{SiO}. From Fig. 4.1, we can see that liquid SiO_2 consists mainly of SiO_4 tetrahedral local units connected by bridging O atoms at ambient pressure. With incresing pressure, fivefold-coordinated Si atoms increase while fourfold-coordinated Si atoms decrease. $f_{\mathrm{SiO}}^{(4)}$ and $f_{\mathrm{SiO}}^{(5)}$ are exchanged for each other at about 20 GPa while $f_{\mathrm{OSi}}^{(2)}$ and $f_{\mathrm{OSi}}^{(3)}$ are interchanged at a higher pressure of about 40 GPa. Above 20 GPa, $f_{\mathrm{SiO}}^{(6)}$ appears, which means that SiO_6 octahedral local unit appears. When pressure increases above 20 GPa, $f_{\mathrm{SiO}}^{(4)}$ decrease, $f_{\mathrm{SiO}}^{(5)}$ does not change and $f_{\mathrm{SiO}}^{(6)}$ increases. At about 50 GPa, the number of fourfold-coordinated Si atoms is 15 % and fivefold-coordinated and sixfold-coordinated Si atoms together accounted for 85 % whereas the number of twofold-coordinated O atoms is still 40 %.

4.3.2 Diffusion properties

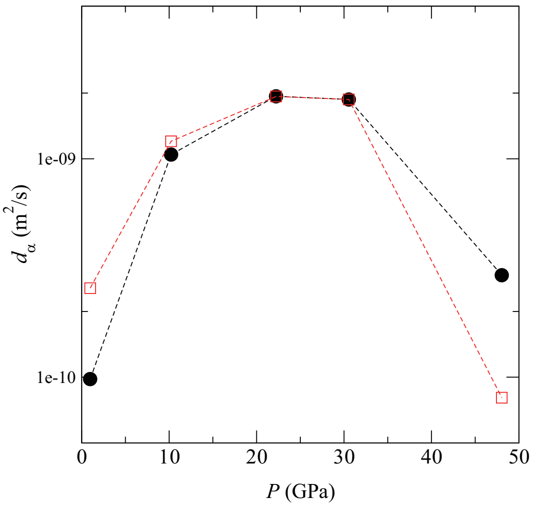

Figure 4.2: Pressure dependence of the diffusion coefficients D_α for α = Si (circles) and O (squares) atoms.

Figure 4.2 shows the diffusion coefficients D_α for α = Si and O atoms as a function of pressure. They were estimated from the slopes of mean aquare displacement. Clearly, there is a diffusion maximum in liquid SiO_2 around 20 GPa. In liquid SiO_2, atomic diffusion occurs by usual concerted reaction the same as liquid B_2O_3 shown in Fig. 3.16. From Fig. 4.1, the number of fourfold-coordinated and fivefold-coordinated Si atoms are almost same at around 20 GPa. This means that the concerted reactions occur more frequently in this pressure region. In the pressure range of $P < 20$ GPa, both D_{Si} and D_{O} increase with increasing pressure similarly to each other. when the pressure approaches about 50 GPa, D_{Si} becomes more than twice larger than D_{O}. As shown in Fig. 4.1 almost all Si atoms are overcoordination such as fivefold or sixfold coordination while bridging O atoms still exist in this pressure region. Therefore, this anomalous diffusion property can be explained by the same mechanism of liquid B_2O_3 shown in 3.17. Namely, there are diffusion path for Si atoms but there are no diffusion path for O atoms at about 50 GPa.

4.4 Results of liquid GeO_2 and $SrGeO_3$

4.4.1 Pair distribution function

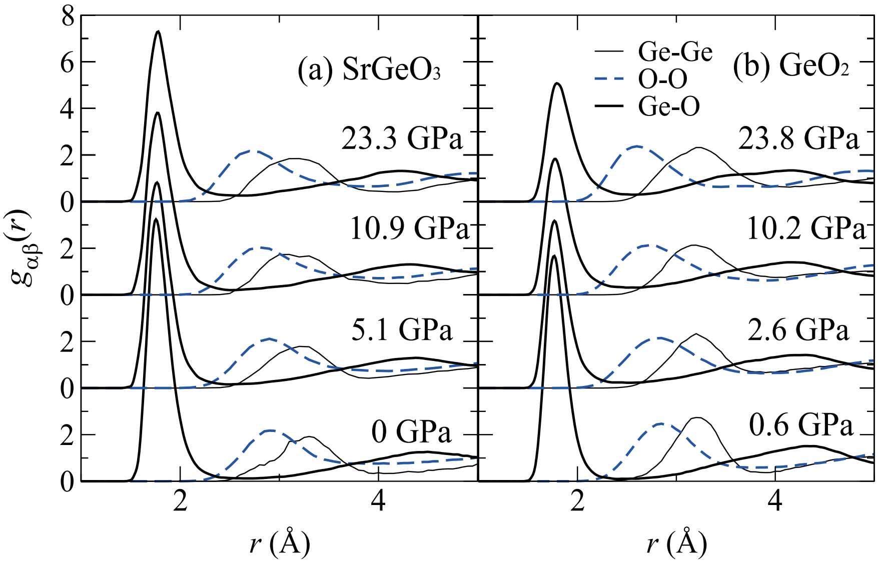

Figure 4.3: Pair distribution function $g(r)$ of liquid $SrGeO_3$ and GeO_2.

Figure 4.3 shows pressure dependence of the partial pair distribution functions $g_{\alpha\beta}(r)$ of liquid $SrGeO_3$ (a) and GeO_2 (b). The position of the sharp first peak of $g_{\mathrm{GeO}}(r)$ is 1.76 Å for both liquids at ambient pressure. the position of both liquids shifts to large r because the Ge-O bond becomes weak with increasing pressure accompanying the increase in the average number of O atoms cooordinated to Ge atoms. The oxygen coordination number around Ge atoms of liquid $SrGeO_3$ and GeO_2 approaches nearly 4.5 and 5.1, respectively, around 23 GPa.

The shape of $g_{\mathrm{GeGe}}(r)$ of liquid $SrGeO_3$ is different from that of liquid GeO_2, while the shape of $g_{\mathrm{OO}}(r)$ are almost the same. This difference of $g_{\mathrm{GeGe}}(r)$ reflects the fact that there are non-bridging oxygens (NBO) in liquid $SrGeO_3$, while almost no NBO in liquid GeO_2.

4.4.2 Diffusion mechanism under ambient pressure

The local structure of crystal GeO_2 and $SrGeO_3$ remain even in liquid state. It is obvious that the covalent bond between Ge and O atoms are preserved in both liquids. It is, however, unclear how Ge-O bonds are exchanged with the diffusion of atoms in the liquid state while retaining the covalent bonds. To clarify the mechanism of atomic diffusion, we investigate the time evolution of bonding nature by utilizing the population analysis [46, 47]. The bond-overlap populations, which give a semiquantitive estimate of the strength of the covalent-like bonding between atoms, are calculated as a function of time.

In liquid GeO_2, Ge atoms are mainly coordinated to four O atoms and O atoms bridge two adjacent Ge atoms as in the crystalline phase, even though atoms diffuse in the liquid state. We find that a non-bridging O atom double bonded to a Ge atom is always involved with atomic diffusion accompanied by Ge-O bond switching as in liquid B_2O_3 [50]. A typical example of the generation of non-bridging oxygen is shown in Fig. 4.5, where the time evolution of the bond overlap populations associated with the Ge and O atoms of interest is displayed with snapshots of atomic configuration. In the atomic configuration at 0.18 ps (the bottom panel of Fig. 4.5) all Ge and O atoms displayed are fourfold- and twofold-coordinated, respectively, to heteroatoms, i.e., there is no bond defect. As shown in the top panel of 4.5, $O_{\mathrm{Ge2-O2}}(t)$ begins to increase at about 0.2 ps, which means that a covalent bond is formed between Ge2 and O2. We can see this new Ge2-O2 bond in the snapshot at 0.27 ps. Due to the formation of the bond, both Ge2 and O2 are overcoordinated. Since the overcoordination is unstable, one of covalent bonds around O2 is broken (in the snapshot at 0.38 ps). Note that Ge1 is coordinated to only three oxygens, while Ge2 is still over-coordinated. Finally, the covalent bond between Ge2 and O1 is broken. While fourfold-coordination around Ge2 atom is recovered, O1 is coordinated only one Ge atom (Ge1) as displayed in the snapshot at 0.60 ps. In this way, the non-

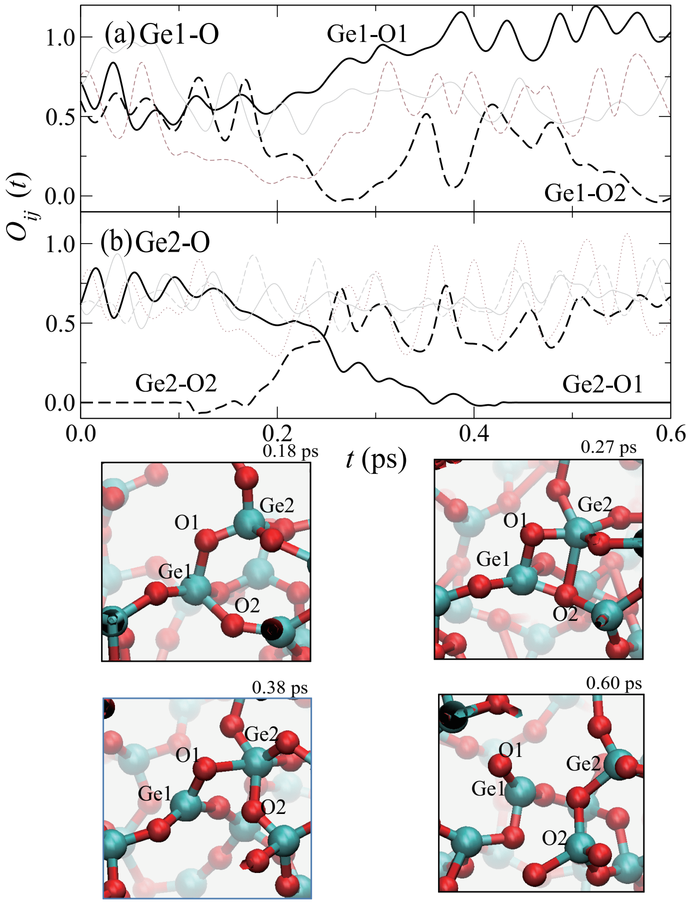

Figure 4.4: (Top panel) The time evolution of bond-overlap populations $O_{ij}(t)$ for (a) i = Ge1, $j \in$ O and (b) i = Ge2, $j \in$ O in the process of the formation of a non-bridging oxygen. The thick sold and thick dashed lines show $O_{ij}(t)$ associated with the Ge and O atoms of interest as denoted in the figures. The thin lines show $O_{ij}(t)$ between the Ge atoms of interest (labeled as 'Ge1' and 'Ge2') and their neighboring O atoms except O1 and O2. (Bottom panel) Atomic configurations at $t = 0.18$, 0.27, 0.38 and 0.60 ps. The large and small spheres show Ge and O atoms, respectively.

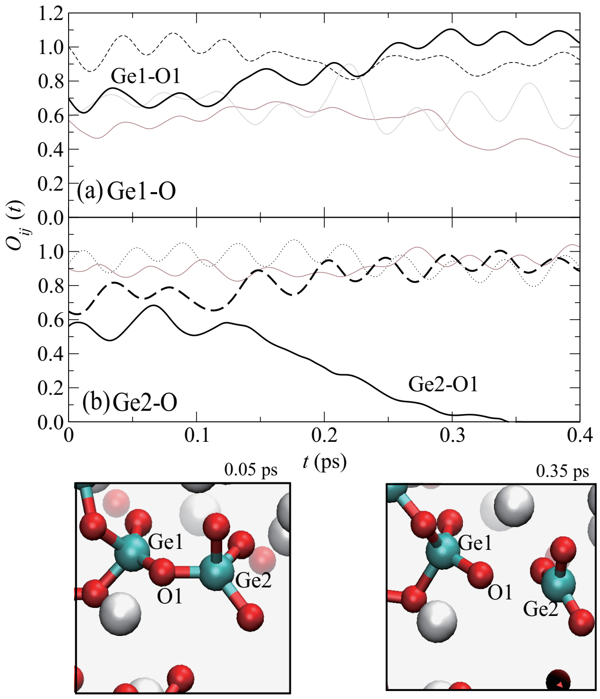

Figure 4.5: (Top panel) The time evolution of bond-overlap populations $O_{ij}(t)$ for (a) i = Ge1, $j \in$ O and (b) i = Ge2, $j \in$ O in the process of the formation of a non-bridging oxygen. The thick sold and thick dashed lines show $O_{ij}(t)$ associated with the Ge and O atoms of interest as denoted in the figures. The thin lines show $O_{ij}(t)$ between the Ge atoms of interest (labeled as 'Ge1' and 'Ge2') and their neighboring O atoms except O1. (Bottom panel) Atomic configurations at $t = 0.05$ and 0.35 ps. The large ,middle and small spheres show Sr, Ge and O atoms, respectively.

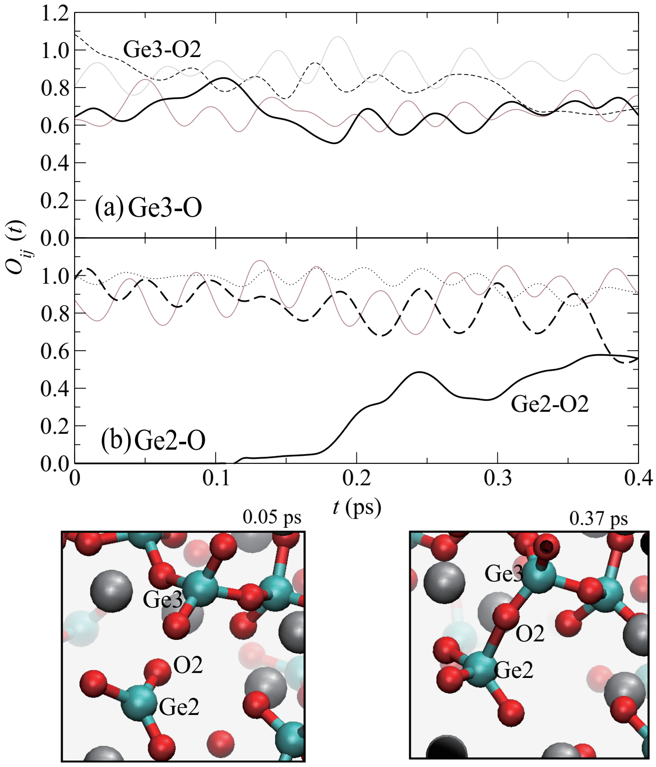

Figure 4.6: (Top panel) The time evolution of bond-overlap populations $O_{ij}(t)$ for (a) i = Ge3, $j \in$ O and (b) i = Ge2, $j \in$ O in the process of the formation of a non-bridging oxygen. The thick sold and thick dashed lines show $O_{ij}(t)$ associated with the Ge and O atoms of interest as denoted in the figures. The thin lines show $O_{ij}(t)$ between the Ge atoms of interest (labeled as ’Ge1’ and ’Ge2’) and their neighboring O atoms except O2. (Bottom panel) Atomic configurations at $t = 0.05$ and 0.37 ps. The large, middle and small spheres show Sr, Ge and O atoms, respectively.

bridging oxygen is generated.

In crystalline $SrGeO_3$, all Ge atoms bond to two bridging oxygens and two non-bridging oxygen. This form is also the most stable in the liquid state as in the crystalline states. When Ge-O bond is broken, the local structure is deformed, for example, Ge atom might be bonding to three bridging oxyges and only one non-bridging oxygen. A typical example of the bond breaking is shown in Fig. 4.6. In the atomic configuration at 0.05 ps, Ge1 bonds to three bridging oxygens and only one non-bridging oxygen. Since this form is not stable, one of bridging oxygens around Ge1 tries to be non-bridging oxygen. As shown in the top panel in Fig. 4.6, $O_{\mathrm{Ge2-O1}}(t)$ begins to decrease at about 0.15 ps. the covalent bond between Ge2 and O1 is broken, as $O_{\mathrm{Ge2-O1}}(t)$ is almost zero for t > 0.35 ps. In the snapshot at 0.35 ps, Ge2 is threefold-coordinated to O atoms, and Ge1 has the most stable form, i.e., bonds to two bridging oxygens and two non-bridging oxygens.

The disappearance process of threefold-coordinated Ge atom (Ge2) is shown in Fig. 4.6. First, the threefold-coordinated Ge2 approaches non-bridging oxygen O2 to form a new covalent bond between them. We see that $O_{\mathrm{Ge2-O2}}(t)$ gradually increases for t > 0.12 ps as shown in the top panel of Fig. 4.6, which means the formation of covalent bond between Ge2 and O2 as displayed in the snapshot at 0.37 ps.

4.4.3 Diffusion mechanism under high pressure

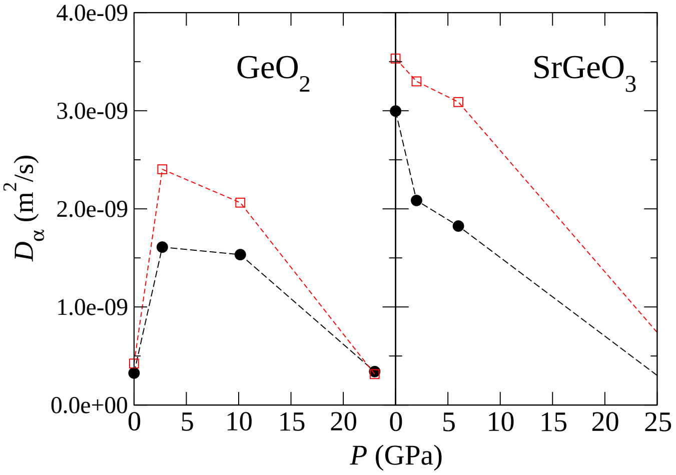

Figure 4.7: Pressure dependence of the diffusion coefficients D_α for α = Ge (solid circles) and O (open squares) atoms.

Figure 4.7 shows the diffusion coefficients D_α for α= Ge and O atoms as a function of pressure. Clearly, only liquid GeO_2 has a diffusion maximum around 5 GPa, while D_α decreases monotonically in liquid $SrGeO_3$. In liquid GeO_2, the atomic diffusion with concerted reaction appears when pressure increases. Figure 4.8 shows this process at about 4 GPa. The concerted reactions with two over-coordinated Ge atoms can take place because Ge atoms are more easily coordinated to five O atoms under higher pressure. The important point is that non-bridging oxygen is not required in this mechanism while the formation of non-bridging oxygens are always involved in diffusion process at ambient pressure. Since liquid $SrGeO_3$ has non-bridging oxygens in normal condition, the formation of non-bridging oxygens is not needed for atomic diffusion at ambient pressure. This is why the diffusivities of liquid $SrGeO_3$ are much higher than those of liquid GeO_2 which does not have non-bridging oxygens at ambient conditions.

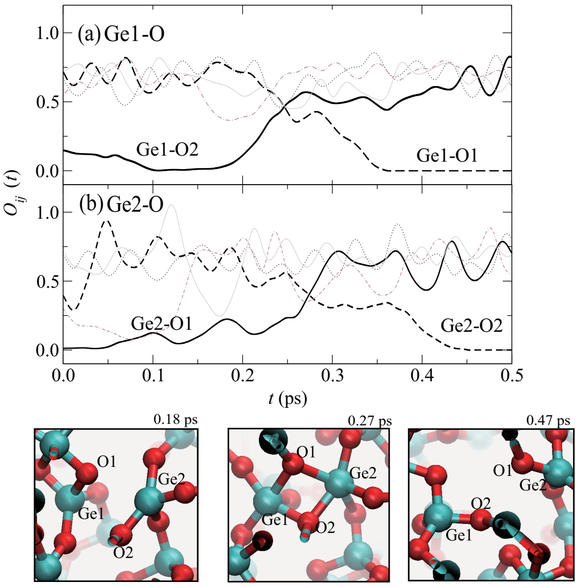

Figure 4.8: (Top panel) The time evolution of bond-overlap populations $O_{ij}(t)$ for (a) i = Ge1, $j \in$ O and (b) i = Ge2, $j \in$ O in the process of the formation of a non-bridging oxygen. The thick sold and thick dashed lines show $O_{ij}(t)$ associated with the Ge and O atoms of interest as denoted in the figures. The thin lines show $O_{ij}(t)$ between the Ge atoms of interest (labeled as 'Ge1' and 'Ge2') and their neighboring O atoms except O1 and O2. (Bottom panel) Atomic configurations at t = 0.18, 0.27 and 0.47 ps. The large and small spheres show Ge and O atoms, respectively.

4.5 Discussion

Altough liquid SiO_2, GeO_2 and $SrGeO_3$ have similar local unit (tetrahedral local unit), it is seen a clear distinction of the dynamic properties, especially diffusion properties under pressure. Liquid SiO_2 have diffudion maximum and dynamic assymetry (Si atom can move easier than O) under pressure. On the other hand, liquid GeO_2 have only diffusion maximum under pressure. When it comes to liquid $SrGeO_3$, it does not even have diffusion maximum under pressure. The reason why liquid GeO_2 does not have dynamic assymetry can be understood from the phase diagram of GeO_2. Figure 4.9 shows the pressure-temperature phase diagram of GeO_2 [24]. Unlike SiO_2, the rutile GeO_2 which consists of GeO_6 units is the most stable phase at room temerature and pressure. That is, high energy does not need to be transformed into GeO_6 local unit compared to transformation of SiO_6. If almost all Si atoms are overcoordination in liquid SiO_2, It is difficult to diffuse for O atom. However, there are diffusion path for O atoms in liquid GeO_2 because it is easier to transform GeO_5 into GeO_6 than transformation of SiO_5. That is, O atoms can move as well as Ge atoms. This is why liquid GeO_2 does not have dynamic assymetry.

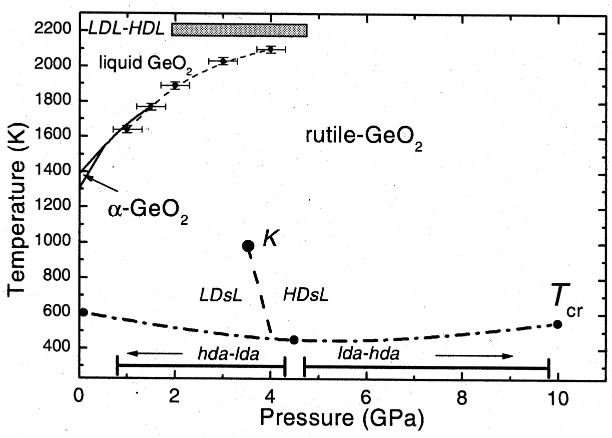

Figure 4.9: Pressure-temperature phase diagram of GeO_2.

With regard to liquid $SrGeO_3$, there are two types of covalent bond in a tetrahedral GeO_4 unit. One is the single bond between Ge and bridging O. The other is the double bond between Ge and nonbridging O. In liquid $SrGeO_3$, atomic diffusion occurs by transformation single bond into double bond and vice versa as shown in Fig. 4.5. Since over-coordinated Ge atoms are not needed in this mechanism, pressure does not enhance the atomic diffusion. Therefore, the diffusivities of liquid $SrGeO_3$ decrease monotonically with pressure.

4.6 Summary

The diffusion properties of liquid SiO_2, GeO_2 and $SrGeO_3$ under pressure are inveistigated by *ab initio* molecular dynamics simulations. Our simulation reveal the origin of anomalous diffusion properties common to all covalent liquids under pressure. The usual concerted reaction with generating overcoordination gives the diffusion maximum under pressure. Atomic diffusion of liquid SiO_2 and liquid GeO_2 occurs with the cocerted reaction while atomic diffusion of liquid $SeGeO_3$ does not need the overcoordination. These distinctions gives whether diffusion coefficients increases or not with pressure. With regaed to dynamic assymetry, it is orignated from the energy differences between the low-pressure phase and the high-pressure phase of crystalline state.

Chapter 5

Metalization in liquid Selenium under high pressure

5.1 Introduction

Both crystalline selenium and tellurium in ambient conditions have a trigonal structure in which each atom is coordinated to two other atoms with strong covalent bonds forming a chain structure. The structural and bonding properties of the crystals are determined by four valence p electrons [53]. Two of them form σ-type covalent bonds between atoms, and the rest occupy non-bonding states which are called lone-pair (LP) states. These crystals behave as a semiconductor, where the valence and conduction bands are formed by the LP and anti-bonding σ^* states, respectively. Under pressure, a similar sequence of structural transitions is exhibited by crystalline selenium [54, 55], tellurium [56, 57, 58, 59], and their mixtures [60] accompanied by a discontinuous increase in the coordination number. All the high pressure states show metallic properties.

On melting at ambient pressure, the chain structure is basically preserved in liquid Se and Te. While liquid Te exhibits semi-metallic properties due to a high density of three-fold coordinated defects [61], liquid Se shows semiconducting properties as the crystalline phase does. Since large chain molecules are maintained in liquid Se, it has a large viscosity near the triple point [62]. Accompanying the decrease of the average chain length with increasing temperature and pressure, the electrical conductivity of liquid Se increases, and a metallic state appears near the critical point in spite of the volume expansion [63, 64, 65]. In relation to such semiconductor-metal (SC-M) transition, the temperature dependence of the structure has been thoroughly studied by x-ray diffraction measurements [66] and first-principles theory [67, 68].

Recently, Brazhkin *et al.* [69] have measured the viscosity of liquid Se at pressures up to 6.3 GPa by real-time radiography. They found that the viscosity decreases largely with pressure along the melting curve in the semiconducting state, and experiences a further significant drop at the pressure where the metallization occurs. They suggested that this observed viscosity decrease is related to the chain defragmentation. However, the details of pressure effects on the chain structure of liquid Se are still unknown, because x-ray diffraction experiments [70, 71, 72] have been carried out so far in only a limited range of pressure: Raty *et al.* [70] have investigated the pressure-induced structural change between 3.0 and 4.1 GPa, Tsuji [71] has reported the x-ray diffraction pattern at 4.4 and 8.4 GPa, and Katayama *et al.* [72] have performed x-ray diffraction experiments in a pressure range from 2.6 to 4.9 GPa. These experimental studies commonly suggest that the local atomic structure of metallic liquid Se under pressure is similar to that of liquid Te.

The pressure dependence of the atomic structure of liquid Te has, on the other hand, been investigated both experimentally and theoretically in detail. Funamori and Tsuji [73] have measured synchrotron x-ray diffraction of liquid Te under pressure up to 22 GPa. They found that there is a maximum at about 6 GPa in the pressure vs nearest-neighbor distance curve, while the coordination number increases monotonically with pressure. Shimojo *et al.* [74] have carried out *ab initio* molecular dynamics (MD) simulations for liquid Te under pressure. They concluded that there are two stages in the compression process. In the first stage, the nearest-neighbor distance increases with pressure up to 6 GPa due to a formation of a weak covalent bonding state between Te atoms. In the second stage, the anisotropy of atomic configuration around each atom reduces with increasing pressure.

In this paper, we investigate the structural, bonding, and dynamic properties of liquid Se under pressure by *ab initio* MD simulations. The purposes of our study are to clarify the structure of liquid Se at high pressures, and to elucidate the microscopic relation between the structural changes and the pressure-induced SC-M transition. We also discuss a comparison with the static structure of liquid Te under pressure.

5.2 Numerical details

In MD simulations, the atomic forces are obtained from the electronic states calculated by the projector-augmented-wave (PAW) method [11, 12] within the framework of density functional theory (DFT). The generalized gradient approximation (GGA) [10] is used for the exchange-correlation energy. The plane-wave cutoff energies are 15 and 100 Ry for the electronic pseudo-wave functions and the pseudo-charge density, respectively. The energy functional is minimized using an iterative scheme [36, 37].Projector functions are generated for the 4s, 4p, and 4d states. The Γ point is used for Brillouin zone sampling. The equations of motion for atoms were solved via an explicit reversible integrator [35] with a time step of $\Delta t = 2.4$ fs. A system of 81 atoms in a cubic supercell is used under periodic boundary conditions. The system-size dependence of the atomic structure is discussed in the Appendix.

Table 5.1: Densities ρ (g/cm^3) used in MD simulations of liquid Se in the canonical ensemble. The relative volumes V/V_0, where V_0 is the volume at $\rho = 3.79$ g/cm^3 ($P = 0$ GPa, $T = 560$ K), and the time-averaged pressures [42, 43] P (GPa) are also listed.

ρ (g/cm^3)	V/V_0	P (GPa)	T (K)
3.91	0.97	0.1	560
4.51	0.84	0.9	650
5.06	0.75	3.3	800
5.42	0.70	5.0	1000
5.78	0.66	7.0	1000
6.14	0.62	9.4	1000
7.30	0.52	28.1	2000
7.89	0.48	39.2	2000
9.52	0.40	85.9	2000

To determine the density of the liquid state under pressure, a constant-pressure MD simulation [39] is performed for 2.4 ps at each given pressure. The temperatures are along the experimental melting curve [69]. Using the time-averaged density, the static and diffusion properties are investigated by MD simulations in the canonical ensemble [40, 41]. The time-averaged pressure [42, 43] is calculated at each density, and we obtain the density-pressure relation as listed in Table. 5.1. The thermodynamic states investigated in this study cover a density range from 3.91 to 9.52 g/cm^3, and a pressure range from 0.1 to 85.9 GPa. The quantities of interest are obtained by averaging over 14.4 $\sim$ 21.6 ps to achieve good statistics after the initial equilibration, which takes at least 2.4 ps.

5.3 Results and discussion

5.3.1 Structure factor

Figure 5.1 shows the pressure dependence of the structure factor $S(k)$ of liquid Se. The solid lines display the calculated $S(k)$. The results of x-ray diffraction experiments [66, 72] are plotted by the open circles. It is seen that the calculated results are in good agreement with experiments. With increasing pressure, the first peak around 1.8 Å^{-1} at 0.1 GPa shifts to larger k, and its intensity increases. In contrast, the second peak decreases its height with pressure, and almost disappears above 9 GPa. The peaked behavior at the highest pressure 85.8 GPa indicates that the system falls into a partially ordered state.

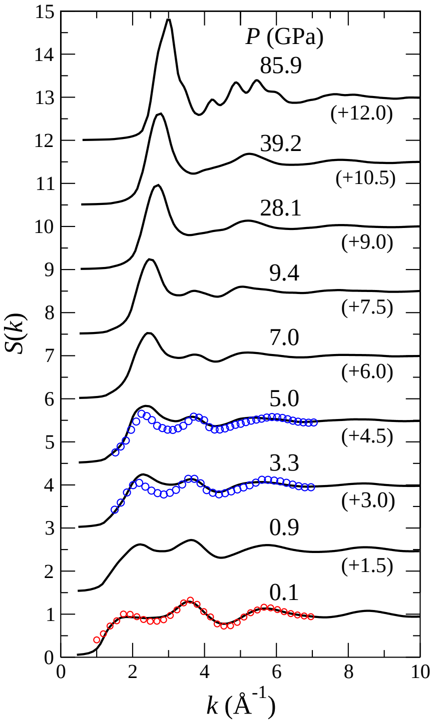

Figure 5.1: Pressure dependence of the total structure factor $S(k)$. The solid lines and open circles show the calculated and experimental $S(k)$, respectively. The curves are shifted vertically as indicated by the figures in parentheses.

5.3.2 Pair distribution function

The pressure dependence of the pair distribution function $g(r)$ of liquid Se is displayed by the solid lines in Fig. 5.2. A sharp first peak exists at about 2.4 Å, well separated from the second peak, at 0.1 GPa. This peak reflects the strong covalent bonding between the intrachain nearest-neighbor atoms. With increasing pressure, the second peak shifts to smaller r, and the first minimum becomes shallower. At 7.0 and 9.4 GPa, the minimum almost disappears, and the second peak becomes a shoulder. At higher pressures, the second peak merges into the first peak, and the height grows with pressure.

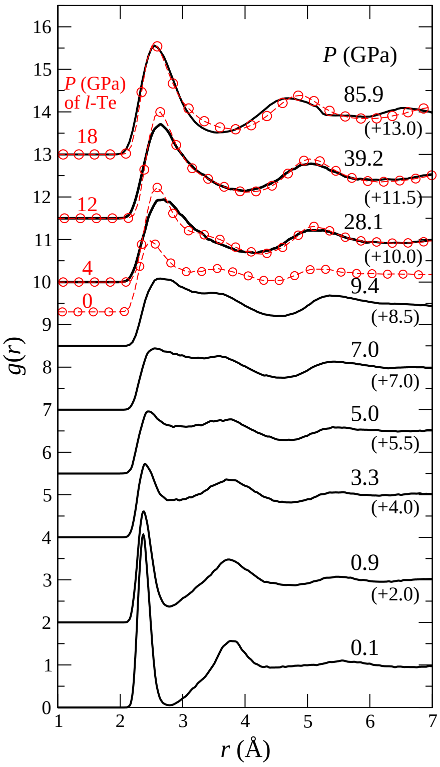

Figure 5.2: Pressure dependence of the pair distribution function $g(r)$. The solid lines show $g(r)$ of liquid Se and the dashed lines with open circle show $g(r)$ of liquid Te. The curves are shifted vertically as indicated by the figures in parentheses.

Figure 5.3 shows the pressure dependence of the coordination number N and the nearest-neighbor distance r_1 (the first-peak position of $g(r)$). The

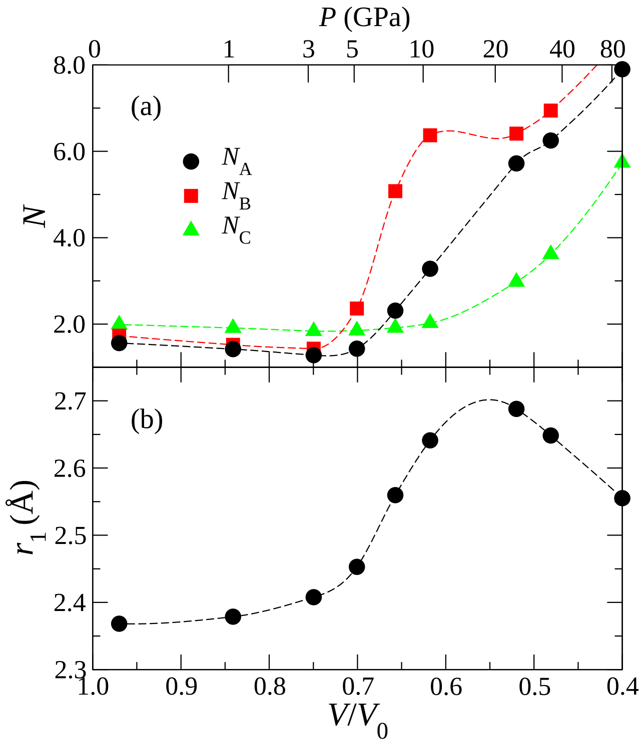

Figure 5.3: (a) Pressure dependence of the average coordination number N. The circles, squares, and triangles show N_A, N_B, and N_C, respectively, calculated by three different definitions (see text). (b) Pressure dependence of the nearest-neighbor distance r_1.

coordination number is obtained in three ways; (A) N_{A} is obtained by integrating $4\pi r^2\rho_0 g(r)$ up to r_1, and multiplying it by two, where the ρ_0 denotes the number density, (B) N_{B} is obtained by integrating $4\pi r^2\rho_0 g(r)$ up to the first-peak position of $4\pi r^2 g(r)$, and multiplying it by two, and (C) N_{C} is by integrating $4\pi r^2\rho_0 g(r)$ up to the first-minimum position of $g(r)$, $r_{\mathrm{min}} = 2.7$ Å, at 0.1 GPa. In Fig. 5.3(a), the circles, squares, and triangles show N_{A}, N_{B}, and N_{C}, respectively. All N_{A}, N_{B}, and N_{C} decrease slightly with pressure below 5 GPa. Since $g(r)$ has the sharp first peak, N_{A} and N_{B} have similar values to each other. However, above 5.0GPa, there is a large difference among them. While N_{A} increases almost linearly with the volume reduction above 5 GPa, N_{B} increases drastically from about 2 to 7 between 5 and 10 GPa. In this pressure range, $g(r)$ has a very broad profile, and, therefore, a discrepancy exists between N_{A} and N_{B}. Unlike N_{A} and N_{B}, N_{C} increases only slightly with pressure. As shown in Fig. 5.3(b), r_1 increases only a little below 5 GPa. When the pressure exceeds 5 GPa, r_1 is extended abruptly, reflecting the broad shape of $g(r)$. r_1 has a maximum around 20 GPa, and decreases with decreasing the volume above that pressure. A more detailed discussion on the changes of the local structure will be given later.

5.3.3 Electronic density of states

Figure 5.4 shows the pressure dependence of the total electronic density of states (DOS), $D(E)$, and the angular-momentum l dependent partial DOS, $D_l(E)$. $D(E)$ is related to $D_l(E)$ as $D(E) = \sum_l D_l(E)$. In $D(E)$, there are two segments below the Fermi level ($E_{\mathrm{F}} = 0$) at 0.1 GPa. The electronic states below -10 eV and above -6 eV originate mainly from the $4s$ and $4p$ electrons, respectively. They are well separated even when the pressure increases. There are two peaks at about -5 eV and -2 eV, which correspond to p-like bonding and p-like non-bonding states, respectively. The DOS above E_{F} comes from p-like anti-bonding states. At 0.1 GPa, $D(E)$ has a deep dip at E_{F} corresponding to the semiconducting properties of liquid Se. The value of $D(E_{\mathrm{F}})$ increases when the pressure increases up to 5.0 GPa. In the sense that $D(E_{\mathrm{F}})$ does not change so much above 5.0 GPa, the metallization is completed around this pressure.

5.3.4 Bond-overlap population

We used population analysis [46, 47] to clarify the change in the bonding properties due to the SC-M transition. By expanding the electronic wave

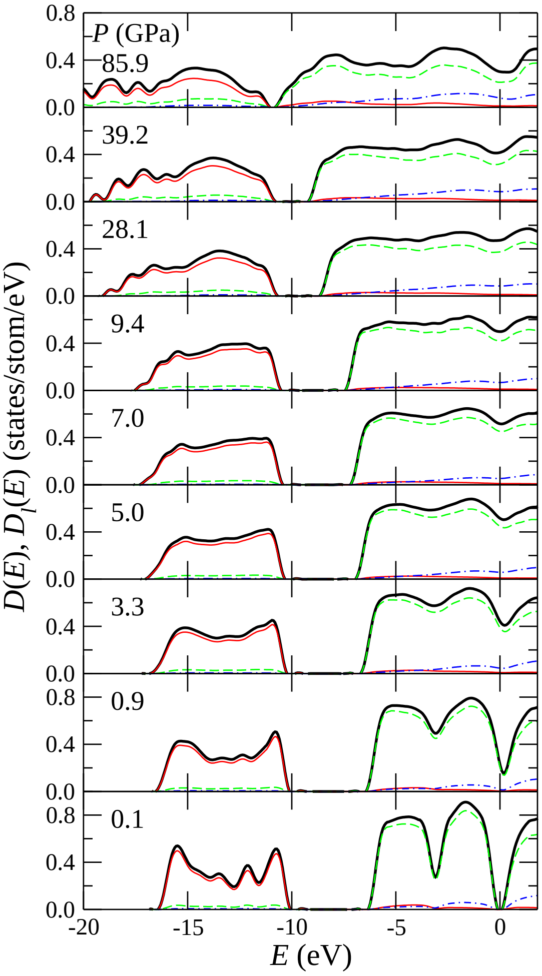

Figure 5.4: Pressure dependence of the electronic density of states $D(E)$ and the angular-momentum l dependent partial electronic density of states $D_l(E)$. The bold solid lines show $D(E)$. The thin solid, dashed, and dot-dashed lines indicate $D_l(E)$ for $l = 0$, 1 and 2, respectively.

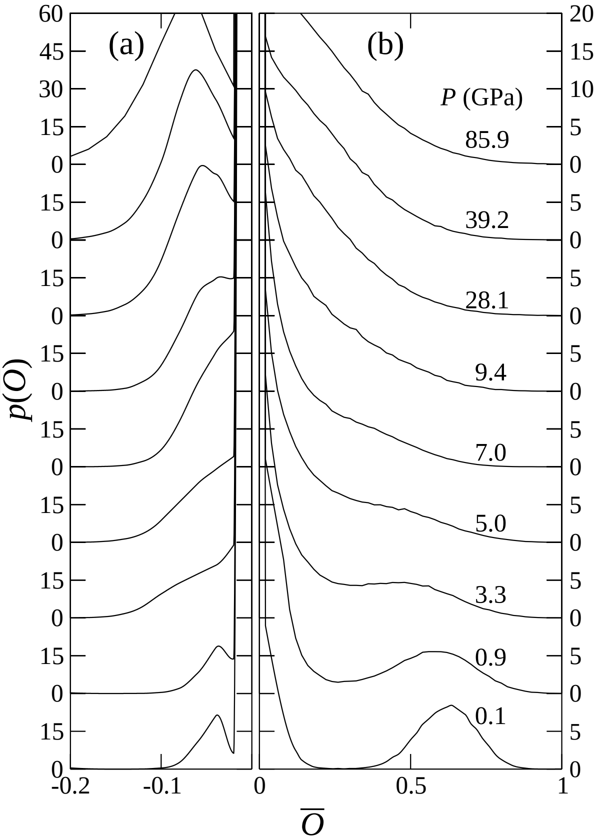

Figure 5.5: Pressure dependence of the distribution of the bond-overlap populations $p(\overline{O})$ for (a) $\overline{O} < 0$ and (b) $\overline{O} > 0$.

functions in an atomic-orbital basis set, we obtain the overlap population $O_{ij}(t)$ between the ith and jth atoms as a function of time t. $O_{ij}(t)$ gives a semiquantitative estimate of the strength of the covalent-like bonding between atoms. Figure 5.5 shows the time-averaged distribution $p(\overline{O})$ of the overlap populations $O_{ij}(t)$. In $p(\overline{O})$, there is a peak clearly at about $\overline{O} = 0.7$ at 0.1 GPa. With increasing pressure, the peak shifts to smaller $\overline{O}$, and becomes broad, which indicates that the covalent-bonding interaction weakens accompanying the metallization. Above 5.0 GPa, the profile of $p(\overline{O})$ for $\overline{O} > 0$ has no clear peak, though we can recognize a shoulder around $\overline{O} = 0.3$ below 10 GPa. The peak around $\overline{O} = -0.05$ at 0.1 GPa corresponds to the repulsive interaction between the next-nearest neighbor atoms within the chain due to the LP states. Although this peak becomes broad with pressure, a new peak grows in the negative $\overline{O}$ region at higher pressures than 10 GPa.

5.3.5 Pressure-induced metallization of liquid Se

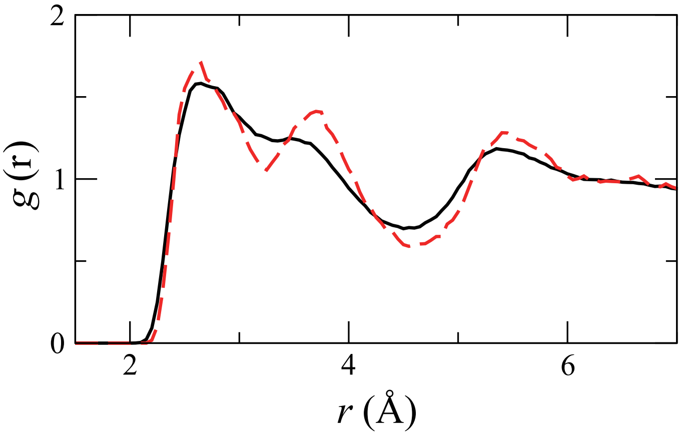

Figure 5.6: Pair distribution function $g(r)$ at 9.4 GPa. The solid and dashed lines show $g(r)$ at 1000 and 500 K, respectively.

As was seen in Fig. 5.3(a), all N_{A}, N_{B} and N_{C} are almost two below 5 GPa, which means that the chain structure remains up to this pressure. The slight decrease of them with pressure indicates that the average chain length shortens under pressure. From the pressure dependence of $D(E_{\mathrm{F}})$ at the Fermi level displayed in Fig. 6.6 as well as that of $p(\overline{O})$ in Fig. 6.7, it is suggested that the pressure-induced metallization is advanced up to 5 GPa, and that the system has the metallic properties at higher pressures. It is concluded from these results that liquid Se is metalized under compression while the chain structure is maintained in the similar way as the metallization near the critical point accompanying the volume expansion [66, 67]. Note that the first minimum of $g(r)$ becomes shallower with increasing pressure from 0 to 5 GPa (Fig. 5.2), which results from the frequent occurrence of bond breaking and bond forming in Se chains under pressure. In other words, such strong interaction between Se chains accompanied with their rearrangement plays an important role for the pressure-induced metallization.

5.3.6 Covalent-like interaction in the metallic state

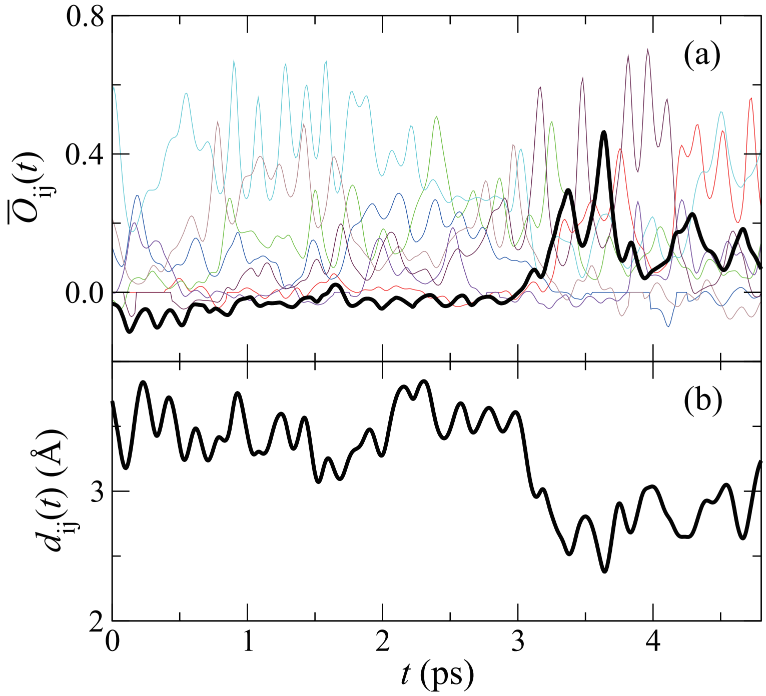

Figure 5.7: (a) The time evolutions of the overlap populations $O_{ij}(t)$. (b) The time evolutions of the atomic distance $d_{ij}(t)$ for the atomic pair corresponding to the bold line in (a).

Between 5 and 10 GPa, N_A and N_B as well as r_1 increase rapidly with compression as shown in Fig. 5.3. This indicates a considerable structural change in this pressure range. As shown in Fig. 5.2, $g(r)$ at 7.0 and 9.4 GPa have a peculiar shape in the sense that $g(r)$ has no clear peaks, and exceeds one in a wide range of r from 2.4 to 4.0 Å. This characteristic profile of $g(r)$ seems to mean that the covalent interactions disappear in liquid Se at these pressures. In order to clarify the origin of the peculiar shape of $g(r)$, it is essential to uncover the inherent structure of these states by eliminating the effects of thermal fluctuations. For this purpose, we decrease the temperature of the system at 9.4 GPa from 1000 to 500 K, while keeping the volume the same, i.e. $V/V_0 = 0.62$. Figure 5.6 compares $g(r)$ obtained at 500 K with that at 1000 K. When the temperature effects are reduced, two peaks appear at 2.6 and 3.7 Å [45]. The coordination numbers at 500 K are $N_{\mathrm{A}} = 3.2$, $N_{\mathrm{B}} = 3.4$, and $N_{\mathrm{C}} = 2.0$. Since $g(r)$ has the clear first peak, N_{A} and N_{B} are consistent with each other. At 1000K, the dip between these two peaks disappears due to larger thermal motion of atoms, and, as a result, $g(r)$ at 7.0 and 9.4 GPa has a peculiar shape.

To discuss the bonding properties between atoms at this volume in detail, the time evolution of $O_{ij}(t)$ between a focused (ith) atom selected arbitrarily and its surrounding (jth) atoms within the distance of 5 Å is shown in Fig. 5.7(a). It is seen that the ith atom interacts with several atoms with finite $O_{ij}(t) > 0$, out of which are one or two atoms with large $O_{ij}(t) \sim 0.4$. Figure 5.7(b) shows the time evolution of the distance $d_{ij}(t)$ between the ith and jth atoms, whose $O_{ij}(t)$ is displayed by the bold line in Fig. 5.7(a). It is obvious that $O_{ij}(t)$ is strongly correlated with $d_{ij}(t)$; when the distance is larger $d_{ij}(t) \sim 3.5$ Å for $t < 3$ ps, $O_{ij}(t)$ is almost zero, and when the distance becomes smaller $d_{ij}(t) \sim 2.6$ Å after 3 ps, $O_{ij}(t)$ comes to be finite. In conclusion, each atom interacts with neighboring atoms through the covalent-like bonding with finite $O_{ij}(t) > 0$ as a remnant of chain structure even though the system is in the metallic state for the pressure range of 5 to 10 GPa (the volume V/V_0 range of 0.6 to 0.7). These atomic pairs form the first peak of $g(r)$ at 2.6 Å.

5.3.7 Comparison with liquid Te

According to *ab initio* MD simulations [74], the coordination number of liquid Te is $N_{\mathrm{A}} = 2.5$, 5.0, 6.3, and 7.0 at 0, 4, 12, and 18 GPa, respectively. Considering this pressure dependence, $g(r)$ of liquid Te is compared with that of liquid Se as displayed by the dashed lines with open circles in Fig. 5.2. Although there is no state in liquid Se well corresponding to that at 0 GPa in liquid Te, the shape of $g(r)$ of liquid Te under pressure is in good agreement with that of liquid Se above 28.1 GPa. These results confirm that the local structure of liquid Se at high pressures is similar to that of liquid

Te.

5.3.8 Dynamic properties

Figure 5.8(a) shows the diffusion coefficients D as a function of pressure, which are estimated from the slopes of the mean squared displacement as

$$D = \lim_{t\to\infty} \frac{\left\langle \{\boldsymbol{r}_i(t) - \boldsymbol{r}_i(0)\}^2 \right\rangle}{6t}, \tag{5.1}$$

where $\boldsymbol{r}_i(t)$ is the position of the ith atom at time t, and $\langle \cdots \rangle$ means taking the average over all atoms and time.

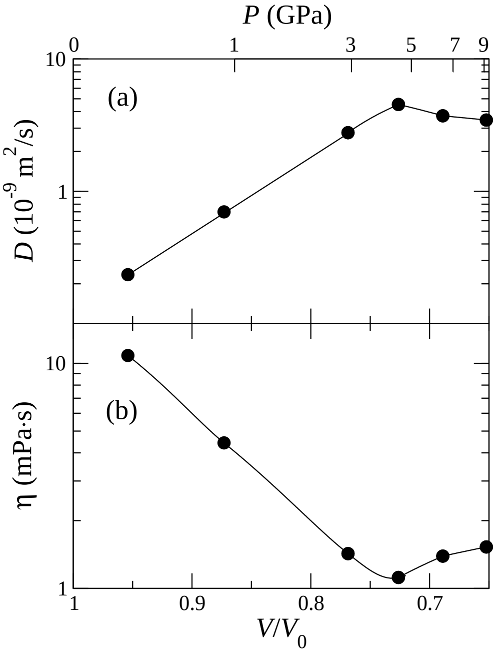

Figure 5.8: Pressure dependence of (a) the diffusion coefficient D and (b) the share viscosity η.

We see that D of liquid Se increases with increasing pressure up to about 5 GPa and temperature up to 1000 K along the experimental melting curve. Since this pressure dependence of D results from the changes of both temperature and pressure, we do not discuss the pure effect of pressure on the

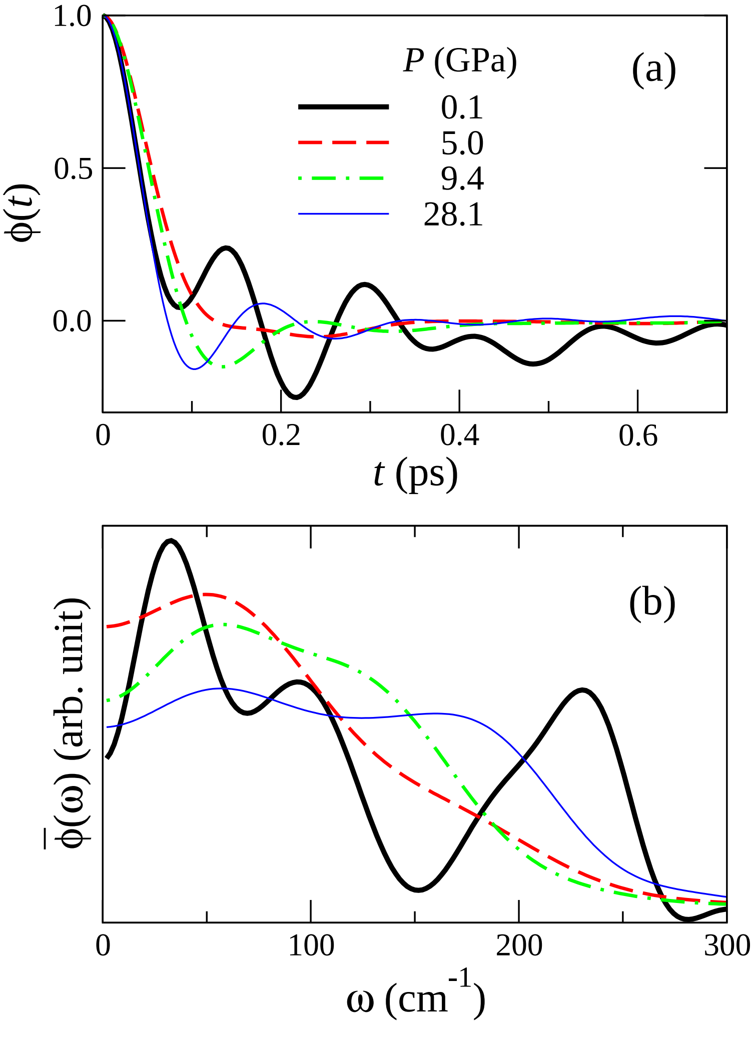

Figure 5.9: Pressure dependence of (a) the normalized velocity autocorrelation function $\phi(t)$ and (b) its Fourier transform $\overline{\phi}(\omega)$.

dynamic properties. It should be noted, however, that the volume contraction enhances the atomic diffusion in covalent liquids, such as liquid SiO_2 [26] and B_2O_3 [34] , due to weakening of the strong covalent-bonding interaction between atoms. In liquid Se, the same effect of pressure should exists while it has the semiconducting properties well below 5 GPa. To compare with the experimental observation, we estimate the viscosity η by using the Stokes-Einstein formula as shown in Fig. 5.8(b). The pressure dependence of η is in qualitative agreement with experiments [69, 75].

The normalized velocity auto-correlation function $\phi(t)$ and its Fourier transform $\overline{\phi}(\omega)$ are defined as

$$\phi(t) = \frac{\langle \boldsymbol{v}_i(t) \cdot \boldsymbol{v}_i(0) \rangle}{\langle \boldsymbol{v}_i(0) \cdot \boldsymbol{v}_i(0) \rangle}, \tag{5.2}$$

$$\overline{\phi}(\omega) = \int_0^\infty \phi(t) \cos(\omega t)\, dt, \tag{5.3}$$

where $\boldsymbol{v}_i(t)$ is the velocity of the ith atom at time t. Figure 5.9 shows the pressure dependence of $\phi(t)$ and $\overline{\phi}(\omega)$. At 0.1 GPa, $\phi(t)$ has an oscillating behavior reflecting the strong covalent bonding in the semiconducting state. The peak of $\overline{\phi}(\omega)$ at 230 cm^{-1} corresponds to the stretching motion of Se-Se bonds. Since the covalent-like interaction becomes weak with increasing pressure as shown in Fig. 5.7, $\phi(t)$ shows less oscillating behavior as displayed by the dashed line for 5 GPa, and the corresponding $\overline{\phi}(\omega)$ consists of a broad peak at a lower frequency $\sim$50 cm^{-1}. On the other hand, in the metallic state, $\phi(t)$ again shows an oscillation as seen at 9.4 and 28.1 GPa, which is considered as the cage effects exhibited by typical liquid metals. $\overline{\phi}(\omega)$ has a shoulder or broad peak at a relatively high frequency around 150 cm^{-1}.

5.4 Summary

We have investigated the structural and bonding properties of liquid Se under pressure up to 85.9 GPa by *ab initio* molecular dynamics simulations. From the analyses of the pair distribution function, the electronic density of states, and the bond-overlap population, the microscopic mechanism of pressure-induced metallization of liquid Se has been revealed. It has been found that a covalent-like interaction exists in the metallic state in the pressure range from 5 to 10 GPa, which gives a characteristic feature of the static structure. It has been confirmed that the local structure of liquid Se and Te under high pressure is similar to each other. The pressure dependence of the dynamic properties, such as the diffusion coefficient and the velocity auto-correlation function, has also been investigated.

Chapter 6

Polymerization transition in liquid AsS under pressure

6.1 Introduction

The microscopic mechanism of structural changes in covalent materials under pressure is a topic of great interest in condensed-matter physics. From the geological viewpoint, not only well-known materials such as SiO_2, but arsenic chalcogenides, especially arsenic monosulfide AsS, which are formed at the boundary between the Earth's upper mantle and crust under pressures of 5-7 GPa, have also attracted considerable attention as minerals [76]. Under ambient conditions, crystalline realgar AsS has a monoclinic structure consisting of As_4S_4 molecules [77, 78].The molecule is made of As atoms threefold coordinated to two S and one As atoms with S atoms bridging two adjacent As atoms. At pressures of about 7 GPa, realgar AsS undergoes a polymorph transition to another molecular phase with a supposedly orthorhombic structure [76].

It is known that, under low-pressure conditions, As_4S_4 molecules remain even upon melting. However, the structural properties and dynamics of liquid AsS under pressure are not well understood. Within the As_4S_4 molecule, atoms are connected by covalent bonds, so the rearrangement of the covalent bonds must occur under compression. While liquid arsenic chalcogenides show semiconducting properties at ambient conditions, high pressure leads to metallization. To investigate the microscopic mechanism of the pressure-induced semiconductor-metal (SC-M) transition, it is important to consider the relationship with the structural changes along with the rearrangement of the covalent bonds.

The temperature dependence of the SC-M transition in liquid arsenic chalcogenides has been extensively studied both experimentally [79, 80, 81] and theoretically [82, 83, 84, 85]. The mechanism of this temperature-induced SC-M transition in liquid As_2S_3 and As_2Se_3 is closely related to the structural change with increasing temperature from the network to chain-like structure [83, 84, 85].

However, we are unaware of theoretical studies of the SC-M transition in liquid arsenic sulfides under pressure.

X-ray diffraction measurements of liquid AsS have clarified the pressure effects on structural properties [86], and two structural changes have been proposed to occur with increasing pressure in the liquid state. The first structural change is from a molecular liquid to a nonmetallic polymerized liquid at 1.6-2.2 GPa. The second structural change is from this nonmetallic polymerized liquid to a metallic liquid at 4.6-4.8 GPa. The viscosity of liquid AsS under high pressure has also been measured [87]. It is highly anomalous that the viscosity increases with pressure up to 2 GPa, after which it drops with further compression. For covalent liquids, the viscosity is strongly related to the covalent interactions, so studying the pressure effects on the bonding properties of liquid AsS to understand the pressure dependence of the viscosity is warranted.

In this paper, we investigate the structural and bonding properties and the dynamics of liquid AsS under pressure using *ab initio* molecular dynamics (MD) simulations. We have recently clarified the microscopic mechanisms of the pressure-induced SC-M transition in monatomic covalent liquid Se [88], and this paper extends this research to compound covalent liquids. A key point to grasp in understanding the properties of this kind of liquid under pressure is that the covalent interactions remain in the metallic state, as indicated earlier for liquid Si [89, 90] as well as for liquid Se [88]. The purposes of our study are (1) to elucidate the microscopic relationship between the structural changes and the pressure-induced SC-M transition and (2) to clarify the pressure effects on the dynamic properties in relation to the covalent interactions in liquid AsS.

6.2 Numerical details

In the MD simulations, a system of 160 (80As+80S) atoms in a cubic supercell is used under periodic boundary conditions. The equations of motion for atoms are solved via an explicit reversible integrator [35] with a time step of $\Delta t = 2.0$ fs. A constant-pressure MD simulation [39] is performed for 4.8

ps at each given pressure to determine the density of the liquid state under pressure. Using the time-averaged density, the static and diffusion properties are investigated by MD simulations in the canonical ensemble [40, 41] at a temperature of 1300 K. The quantities of interest are obtained by averaging over 14.4 $\sim$ 21.6 ps to achieve good statistics after the initial equilibration, which takes at least 2.4 ps.

The atomic forces are obtained from the electronic states calculated using the projector-augmented-wave method [11, 12] within the framework of density functional theory. Projector functions are generated for the $4s$, $4p$, and $4d$ states of As and the $3s$, $3p$, and $3d$ states of S. The plane-wave cutoff energies for the electronic pseudo-wave functions and the pseudo-charge density are 20 and 150 Ry, respectively. The exchange-correlation energy is treated by the generalized gradient approximation (GGA) [10]. The Γ point is used for Brillouin zone sampling. The energy functional is minimized using an iterative scheme [36, 37].

6.3 Results

6.3.1 Volume-pressure relation

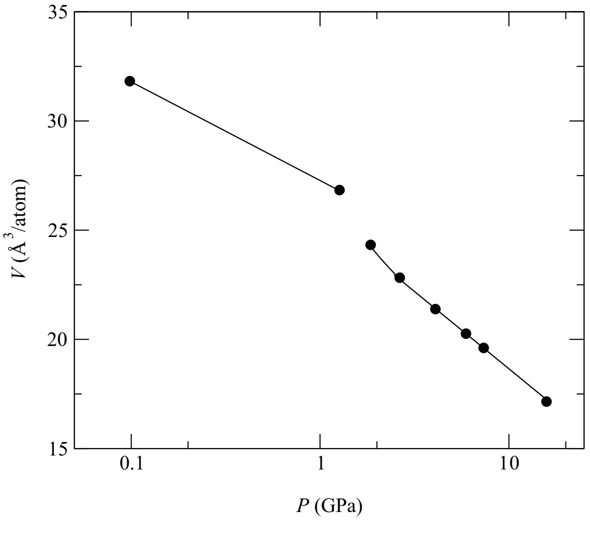

Figure 6.1: Volume as a function of pressure for liquid AsS at 1300 K.

The time-averaged pressure [42, 43] is calculated at each density, and leads to the volume-pressure relation shown in Fig. 6.1. The thermodynamic states investigated in this study cover a density range from 2.79 to 5.17 g/cm^3, and a pressure range from 0.1 to 15.8 GPa. Figure 6.1 shows that the pressure dependence of the volume changes qualitatively at around 2 GPa. This feature suggests that a first-order liquid-liquid transition occurs in liquid AsS, which is related to the transition from the molecular liquid to the polymeric liquid, as described in detail below.

6.3.2 Structure factor

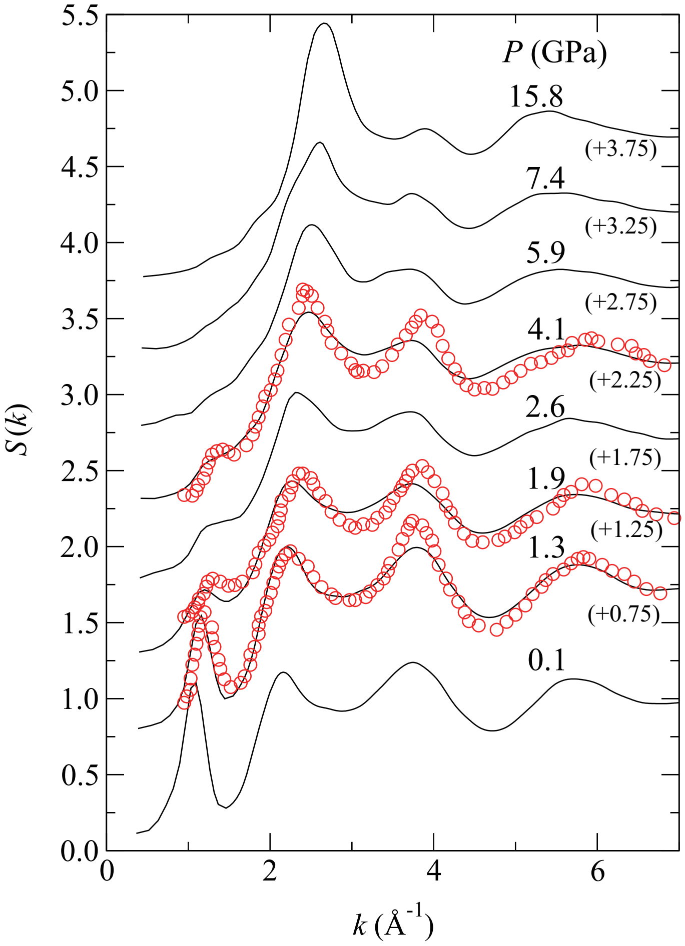

Figure 6.2: Pressure dependence of the total structure factor $S(k)$. The solid lines show the calculated $S(k)$, and the open circles represent the $S(k)$ obtained by x-ray diffraction measurements [86]. The curves are shifted vertically as indicated by the figures in parentheses.

Figure 6.2 shows the pressure dependence of the structure factor $S(k)$ of liquid AsS. The solid lines represent the calculated $S(k)$, which are obtained from the partial structure factors $S_{\alpha\beta}(k)$ with the x-ray scattering factors. The results of x-ray diffraction experiments [86] are indicated by open circles. The calculated results are in fairly good agreement with experiments. A remarkable feature exhibited in $S(k)$ is the first-sharp diffraction peak (FSDP) near $k = 1$ Å^{-1}. This peak reflects the existence of some structural characteristics in an intermediate range, such as the presence of As_4S_4 molecules below 2 GPa. The position of the FSDP gradually shifts to larger wavevectors and the intensity decreases with increasing pressure. Above 4.1 GPa, there is no clear FSDP. The height of the peak near $k = 2$ Å^{-1} increases with compression, whereas the peak height near $k = 4$ Å^{-1} decreases. Figure 6.3 shows

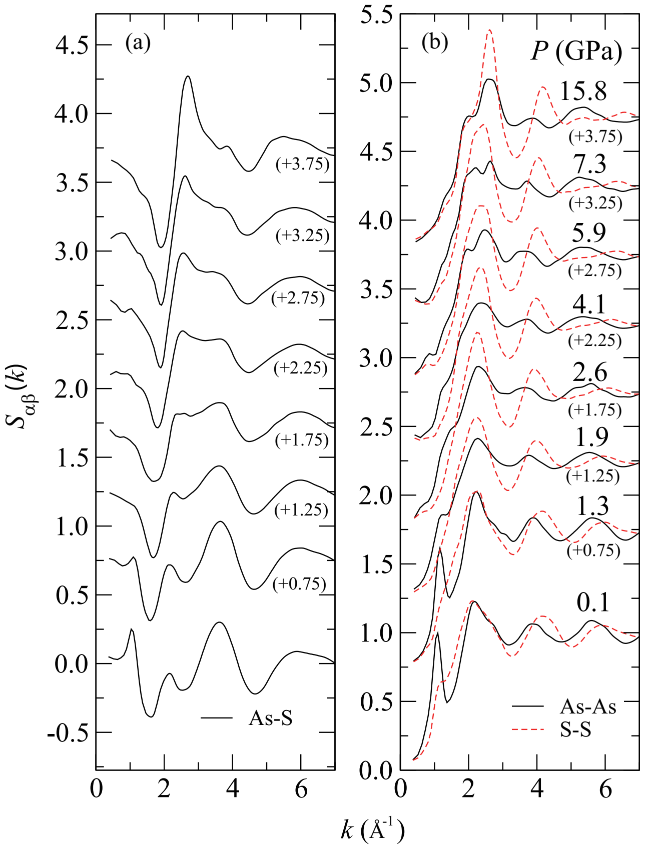

Figure 6.3: Pressure dependence of the partial structure factors $S_{\alpha\beta}(k)$. (a) The solid lines show $S_{\mathrm{AsS}}(k)$. (b) The solid and dashed lines indicate $S_{\mathrm{AsAs}}(k)$ and $S_{\mathrm{SS}}(k)$, respectively. The curves are shifted vertically as indicated by the figures in parentheses.

the pressure dependence of $S_{\alpha\beta}(k)$. We see that the FSDP shown in Fig. 6.2 is mainly determined by the As-As correlation, although the As-S correlation also contributes to forming the FSDP. The S-S correlation has only a shoulder at the position of FSDP. The intensities of these peaks decrease drastically for pressures above 1.3 GPa, which corresponds to the breakdown of As_4S_4 molecules in the liquid under compression. The peak of $S_{\mathrm{AsAs}}(k)$ near $k = 2$ Å^{-1} splits into two peaks for pressures above 4.1 GPa. Above 2.6 GPa, a shoulder appears in $S_{\mathrm{SS}}(k)$ near $k = 1.8$ Å^{-1}. The decrease of the intensity of the peak in $S(k)$ near $k = 4$ Å^{-1} originates from the decrease in the $S_{\mathrm{AsS}}(k)$ peak.

6.3.3 Pair distribution function

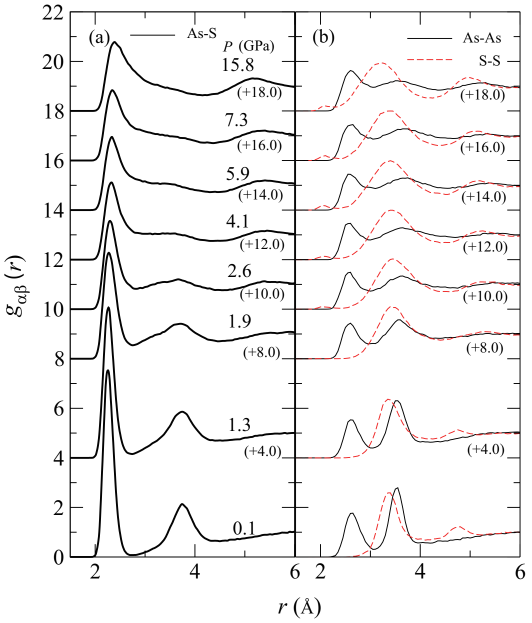

Figure 6.4: Pressure dependence of the pair distribution functions $g_{\alpha\beta}(r)$. (a) The solid lines show $g_{\mathrm{AsS}}(r)$. (b) The solid and dashed lines indicate $g_{\mathrm{AsAs}}(r)$ and $g_{\mathrm{SS}}(r)$, respectively. The curves are shifted vertically as indicated by the figures in parentheses.

The pressure dependence of the pair distribution functions $g_{\alpha\beta}(r)$ of liquid AsS is shown in Fig. 6.4. Since As_4S_4 molecules remain intact up to 1.3 GPa, the shape of $g_{\alpha\beta}(r)$ is almost unchanged. Above 1.9 GPa, $g_{\alpha\beta}(r)$ is largely different from those at lower pressures because the As_4S_4 molecule is broken. In particular, the first minimum and second peak of $g_{\mathrm{AsS}}(r)$ disappear with increasing pressure. Note that, above 2.6 GPa, the peak reflecting to the formation of S-S homopolar bonds appears clearly near $r = 2.1$ Å in $g_{\mathrm{SS}}(r)$. The S-S homopolar bond also exists in liquid $\mathrm{As_2S_3}$ at ambient pressure [91].

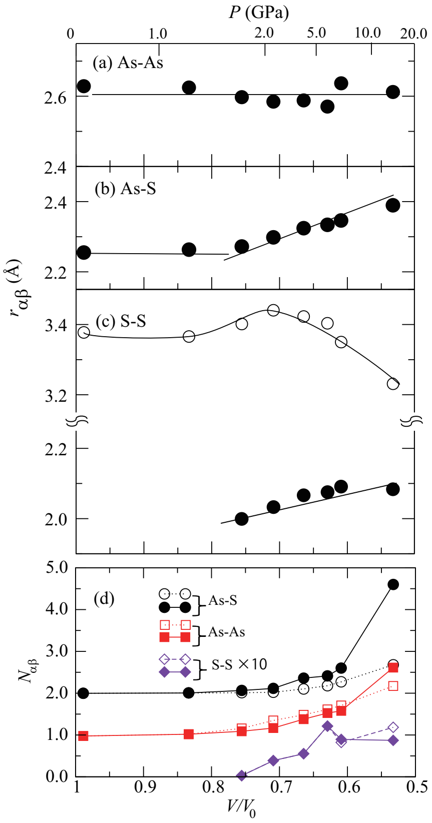

Figure 6.5: Pressure dependence of the nearest-neighbor distances $r_{\alpha\beta}$ for (a) α-β = As-As, (b) α-β = As-S, and (c) α-β = S-S. (d) Pressure dependence of the average coordination numbers $N_{\alpha\beta}$. The circles, squares, and diamonds show N_{AsS}, N_{AsAs} and N_{SS}, respectively. The open and solid symbols indicate $N^{(\mathrm{I})}_{\alpha\beta}$ and $N^{(\mathrm{II})}_{\alpha\beta}$, respectively (see text).

Figure 6.5 shows the pressure dependence of the nearest-neighbor distances $r_{\alpha\beta}$ [the first-peak positions of $g_{\alpha\beta}(r)$]. In Fig. 6.5(c), the open circles indicate the position of the peak in $g_{\mathrm{SS}}(r)$ which exists from ambient pressure, and the solid circles show the peak of the homopolar bonds above 2.6 GPa. At ambient pressure, r_{AsS}, r_{AsAs}, and r_{SS} are 2.62, 2.25, and 3.38 Å, respectively. These distances are almost the same as for the crystalline state [92] and remain almost unchanged up to 1.3 GPa. Above 1.9 GPa, the As-S and S-S covalent bonds lengthen gradually with increasing pressure, as indicated by the solid circles in Figs. 6.5(b) and 6.5(c), whereas no such change is seen in r_{AsAs} (Fig. 6.5(a)).

Figure 6.5(d) shows the pressure dependence of the partial coordination numbers $N_{\alpha\beta}$ for α-β = As-S (circles), As-As (squares), and S-S (diamonds). The coordination numbers are obtained in two ways: (I) $N_{\alpha\beta}^{(\mathrm{I})}$ are obtained by the integration of $4\pi r^2 \rho_\beta g_{\alpha\beta}(r)$ up to the first minimum position $r_{\alpha\beta}^{\mathrm{min}}$ of $g_{\alpha\beta}(r)$ at 0.1 GPa for As-S and As-As, and at 2.6 GPa for S-S ($r_{\mathrm{AsS}}^{\mathrm{min}} = 2.7$, $r_{\mathrm{AsAs}}^{\mathrm{min}} = 3.0$, and $r_{\mathrm{SS}}^{\mathrm{min}} = 2.35$ Å), where ρ_β denotes the number density of β-type atoms. (II) $N_{\alpha\beta}^{(\mathrm{II})}$ are obtained by the integration of $4\pi r^2 \rho_\beta g_{\alpha\beta}(r)$ up to the first minimum of $r^2 g_{\alpha\beta}(r)$ at each pressure. At ambient pressure, $N_{\mathrm{AsS}} = 2$ and $N_{\mathrm{AsAs}} = 1$, irrespective of the method of calculation. These values are the same as for the crystalline state consisting of $\mathrm{As_4S_4}$ molecules. Above 1.9 GPa, both N_{AsS} and N_{AsAs} begin to increase. Note that $N_{\mathrm{AsS}}^{(\mathrm{II})}$ and $N_{\mathrm{AsAs}}^{(\mathrm{II})}$ increase drastically above 10 GPa as shown by the solid symbols, which indicates that the first-coordination shell changes significantly in this pressure range, as discussed in Sec. 6.4. Above 2.6 GPa, N_{SS} has finite values, and increases with compression. Different from $N_{\mathrm{AsS}}^{(\mathrm{II})}$ and $N_{\mathrm{AsAs}}^{(\mathrm{II})}$, $N_{\mathrm{SS}}^{(\mathrm{II})}$ does not show the sudden increase at pressures over 10 GPa, but keeps a similar value of about 0.1.

6.3.4 Electronic density of states

Figure 6.6 shows the pressure dependence of the total electronic density of states (DOS) $D(E)$ and the partial DOS $D_\alpha(E)$. The electronic states below -8 eV and above -6.5 eV originate mainly from the hybridization of s and p electrons, respectively. They are well separated from each other even for pressures up to 15.8 GPa. The DOS above E_{F} ($E = 0$) originates from p-like anti-bonding states. At 0.1 GPa, $D(E)$ has a small gap at E_{F}, which corresponds to the semiconducting properties of the liquid. Although the gap remains at pressures up to 1.3 GPa, the value of $D(E_{\mathrm{F}})$ becomes finite above 1.9 GPa, and increases with increasing pressure, which indicates that metallization follows the rupture of $\mathrm{As_4S_4}$ molecules. It should, however, be noted that having a finite value of $D(E_{\mathrm{F}})$ does not directly prove that the system has the metallic properties. It is also well known that GGA underestimates band gaps in semiconductors. In addition to these facts, at pressures of 1.9-4.1 GPa, a deep dip is recognized at E_{F}. Therefore, we consider that the

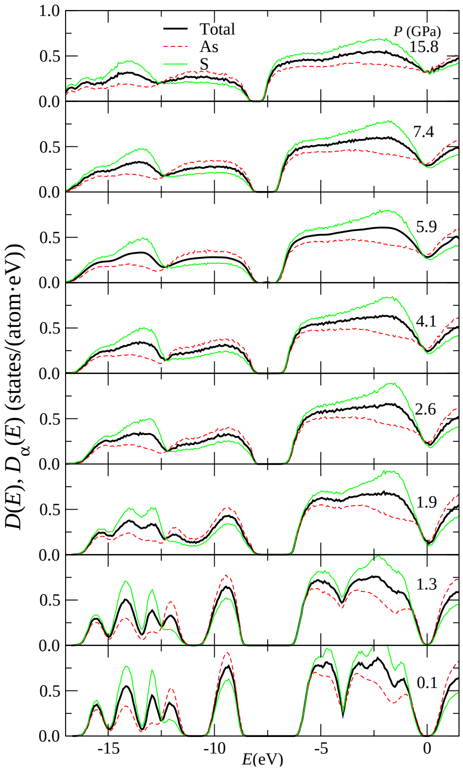

Figure 6.6: Pressure dependence of the electronic density of states $D(E)$ and the partial electronic density of states $D_\alpha(E)$. The bold-solid lines indicate $D(E)$. The thin-dashed and thin-solid lines show $D_{\mathrm{As}}(E)$ and $D_{\mathrm{S}}(E)$, respectively.

system is not completely metalized but has some semiconducting properties over this pressure range even after polymerization. In this sense, our calculations are consistent with the experimental observations [86], which suggest that nonmetallic polymerized liquid is metalized at 4.6-4.8 GPa. The shape of $D(E)$ does not change significantly for pressures above 4.1 GPa, indicating that metallization is completed at this pressure.

6.3.5 Bond-overlap population

We use population analysis [46, 47] to clarify changes in bonding properties associated with compression. By expanding the electronic wave functions in an atomic-orbital basis set, we obtain the overlap population $O_{ij}(t)$ between the ith and jth atoms as a function of time t. $O_{ij}(t)$ gives a semi-quantitative estimate of the strength of the covalent-like bonding between atoms. Note

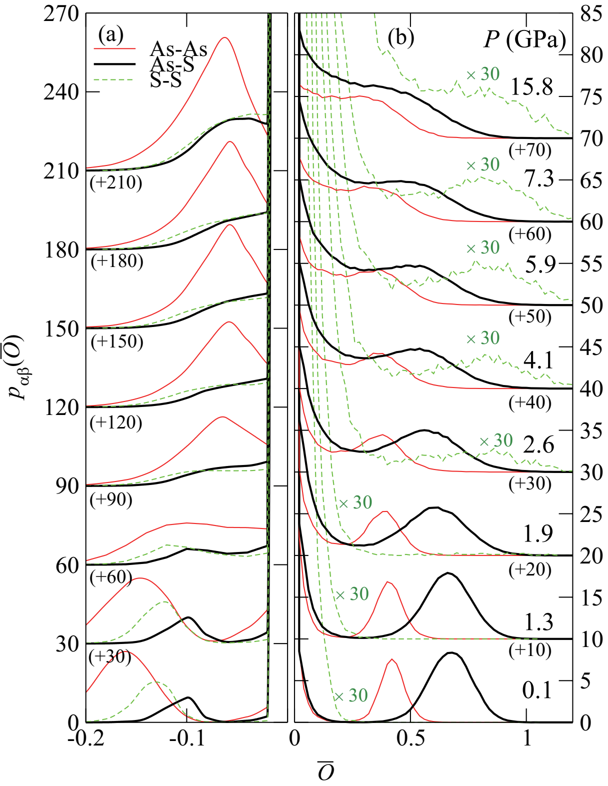

Figure 6.7: Pressure dependence of the distribution $p_{\alpha\beta}(\overline{O})$ of the bond-overlap populations for (a) $\overline{O} < 0$ and (b) $\overline{O} > 0$. The bold-solid, thin-solid, and thin-dashed lines indicate $p_{\mathrm{AsS}}(\overline{O})$, $p_{\mathrm{AsAs}}(\overline{O})$, and $p_{\mathrm{SS}}(\overline{O})$, respectively. In (b), $p_{\mathrm{SS}}(\overline{O})$ are enlarged to thirty times the original value. The curves are shifted vertically as indicated by the figures in parentheses.

that $p_{\alpha\beta}(\overline{O})$ is normalized so that $\int_{O_{\min}}^{\infty} p_{\alpha\beta}(\overline{O})\,\mathrm{d}\overline{O}$ gives the average number of β-type atoms that have overlap populations greater than $O_{\min}$ around one α-type atom.

Figure 6.7 shows the time-averaged distribution $p_{\alpha\beta}(\overline{O})$ of the overlap populations $O_{ij}(t)$. In $p_{\mathrm{AsS}}(\overline{O})$ and $p_{\mathrm{AsAs}}(\overline{O})$, clear peaks exist near $\overline{O} = 0.7$ and $\overline{O} = 0.4$, respectively, up to 1.3 GPa, which reflects the covalent-bond interactions within $\mathrm{As_4S_4}$ molecules. Above 1.3 GPa, $p_{\mathrm{AsS}}(\overline{O})$ and $p_{\mathrm{AsAs}}(\overline{O})$ increase with pressure in the ranges of $0 < \overline{O} < 0.5$ and $0 < \overline{O} < 0.3$, respectively, because bond exchange and bond rupture occur more frequently at higher pressures. Up to 5.9 GPa, the peaks in $p_{\mathrm{AsS}}(\overline{O})$ and $p_{\mathrm{AsAs}}(\overline{O})$

remain near $\overline{O} = 0.7$ and $\overline{O} = 0.4$, respectively, which indicates that the covalent interactions survive in this pressure range. The shift of these peaks to smaller $\overline{O}$ with increasing pressure means that the covalent interactions weaken, which is why r_{AsS} and r_{SS} increase with pressure, as indicated by the solid circles in Fig. 6.5. Above 2,6 GPa, $p_{\mathrm{SS}}(\overline{O})$ has a broad peak near $\overline{O} = 0.8$, which corresponds to the pressure-induced appearance of the S-S homopolar bonds. For $\overline{O} < 0$, the profiles of $p_{\alpha\beta}(\overline{O})$ are significantly different below and above 1.9 GPa, reflecting the transition from molecular to polymeric liquid.

6.3.6 Diffusion coefficient

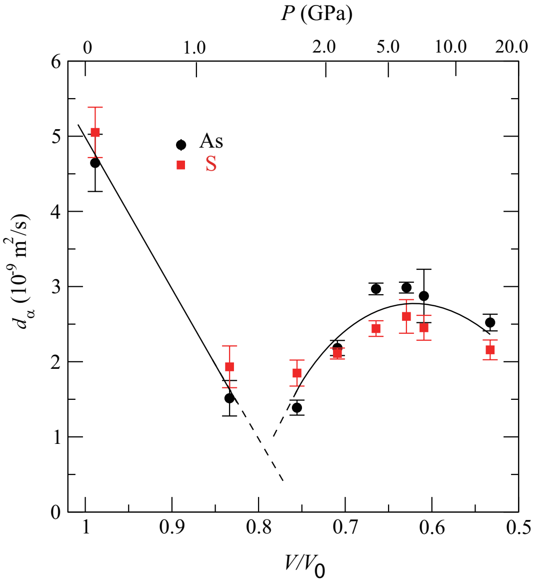

Figure 6.8: Pressure dependence of the diffusion coefficients d_α for α = As (circles) and α = S (squares).

The pressure dependence of the diffusion coefficients d_α is shown in Fig 6.8. Up to 1.3 GPa, d_α decrease with increasing pressure while remaining the As_4S_4 molecule intact. In molecular liquids, long-range molecular diffusion must occur in order for atoms to diffuse long range. As pressure increases from 0.1 to 1.3 GPa, the volume of the system largely decreases as shown in Fig. 1. Therefore, the free space between molecules is reduced and the molecular diffusion path is significantly limited. In addition, we observed that direct interactions between molecules become stronger, i.e., new bonds are almost formed between neighboring molecules at 1.3 GPa. As a result, diffusion coefficients decrease rapidly.

Above 1.9 GPa, the pressure dependence changes qualitatively. Although the system exhibits metallic properties in the sense that there is no energy gap in the DOS at E_{F} in this pressure range (as shown in Fig. 6.6), covalent interactions exist between atoms (as shown in Fig. 6.7). Since each bond weakens with an increase in the number of neighboring atoms, bond exchange occurs easily and frequently, and the diffusion coefficients increase above 1.9 GPa. Under further compression, d_α eventually decrease so that a local maximum occurs around 5 GPa, as seen in typical covalent liquids [34, 93]. The pressure dependence of d_α corresponds well to the experimentally measured pressure dependence of the viscosity [87] . Note that the experimental measurements were performed just above the melting temperature at each pressure, whereas all simulations were carried out at 1300 K. However, changing the pressure in the order of GPa has a stronger effect than changing the temperature by an order of 100 K, as suggested by Fig. 2 of ref. 12. Therefore, the qualitative pressure dependence of the calculated d_α agrees with that of the experimental viscosity.

As for temperature dependence, the transition pressure of polymerization will increase and the diffusion maximum will appear more clearly when the temperature decreases.

6.4 Discussion

We discuss here the pressure-induced structural changes in relation to the covalent interactions. Each pair distribution function $g_{\alpha\beta}(r)$ is resolved according to the strength of the interatomic covalent bonds. The bold-dashed, thin-solid, and thin-dashed lines in Fig 6.9 show $g^{(+)}_{\alpha\beta}(r)$, $g^{(-)}_{\alpha\beta}(r)$, and $g^{(0)}_{\alpha\beta}(r)$ obtained from atomic pairs with $O_{ij}(t) \geq \delta$, $O_{ij}(t) \leq -\delta$, and $-\delta < O_{ij}(t) < \delta$, respectively (we use $\delta = 0.01$). At 0.1 GPa, the first peak of $g_{\mathrm{AsS}}(r)$ consists of only $g^{(+)}_{\mathrm{AsS}}(r)$, whereas the second peak consists of mainly $g^{(-)}_{\mathrm{AsS}}(r)$. A similar profile is apparent in $g_{\mathrm{AsAs}}(r)$, i.e., $g^{(+)}_{\mathrm{AsAs}}(r)$ and $g^{(-)}_{\mathrm{AsAs}}(r)$ form the first and second peak, respectively, of $g_{\mathrm{AsAs}}(r)$. Note that $g^{(+)}_{\mathrm{AsS}}(r)$ and $g^{(+)}_{\mathrm{AsAs}}(r)$ have broad peaks at 3.2∼3.5 Å, which comes from inter-molecular interactions, whereas the peaks of $g^{(-)}_{\mathrm{AsS}}(r)$ and $g^{(-)}_{\mathrm{AsAs}}(r)$ correspond to intra-molecular interactions. With increasing pressure, the broad peaks of $g^{(+)}_{\mathrm{AsS}}(r)$ and $g^{(+)}_{\mathrm{AsAs}}(r)$

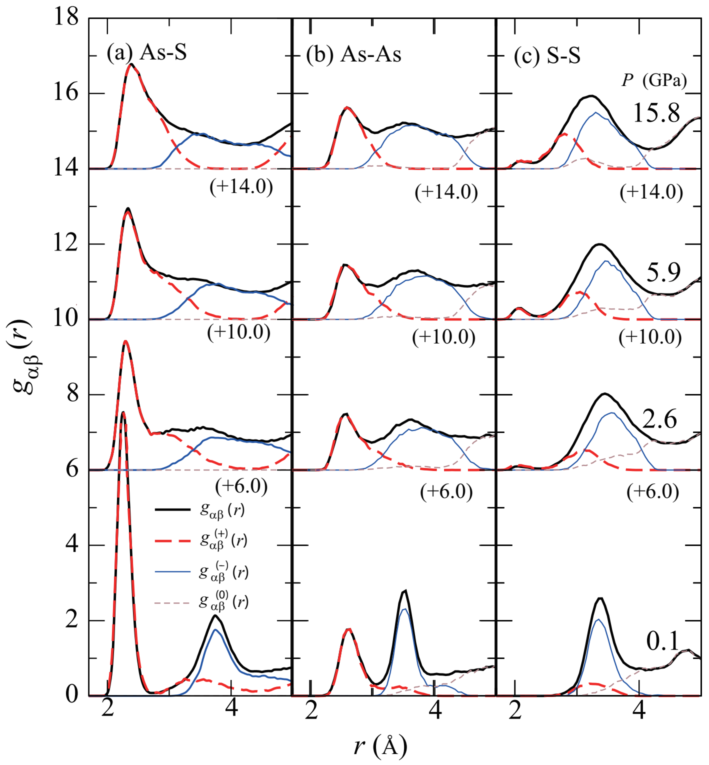

Figure 6.9: Pressure dependence of the pair distribution functions for (a) As-S, (b) As-As, and (c) S-S. The bold-dashed, thin-solid, and thin-dashed lines show $g_{\alpha\beta}^{(+)}(r)$ obtained for $O_{ij}(t) > \delta$, $g_{\alpha\beta}^{(-)}(r)$ for $O_{ij}(t) < -\delta$, and $g_{\alpha\beta}^{(0)}(r)$ for $-\delta < O_{ij}(t) < \delta$, respectively, with $\delta = 0.1$. The bold-solid lines indicate $g_{\alpha\beta}(r)$. The curves are shifted vertically as indicated by the figures in parentheses.

shift to smaller r, and merge into their respective first peaks. However, the peaks of $g_{\mathrm{AsS}}^{(-)}(r)$ and $g_{\mathrm{AsAs}}^{(-)}(r)$ remain well separated from their first peaks. These results mean that the increase in average coordination number accompanying the polymerization transition is due to bond formation between atoms belonging to different molecules; that is, after the transition, atoms belonging to different molecules come into the first coordination shell.

At 15.8 GPa, $g_{\mathrm{AsS}}^{(-)}(r)$ and $g_{\mathrm{AsAs}}^{(-)}(r)$ interpenetrate $g_{\mathrm{AsS}}^{(+)}(r)$ and $g_{\mathrm{AsAs}}^{(+)}(r)$, respectively. Consequently, the coordination numbers $N_{\mathrm{AsS}}^{(\mathrm{II})}$ and $N_{\mathrm{AsAs}}^{(\mathrm{II})}$ increase drastically, as shown in Fig. 6.5(d). We consider that the covalent nature of the liquid becomes quite weak in this pressure range.

Regarding the S-S correlation, $g_{\mathrm{SS}}^{(-)}(r)$, which originates from intra-molecular correlation, provides the main contribution at 0.1 GPa to the peak of $g_{\mathrm{SS}}(r)$ at 3.3 Å. $g_{\mathrm{SS}}^{(+)}(r)$ also has a small peak, which corresponds to inter-molecular interactions. These results show that no clear chemical bonds exist between S atoms at 0.1 GPa. With increasing pressure, a peak appears near 2.1 Å that consists of $g_{\mathrm{SS}}^{(+)}(r)$, which indicates the formation of S-S homopolar bonds between different molecules. Note that the peak of $g_{\mathrm{SS}}^{(+)}(r)$ near 3.3 Å shifts to smaller r with increasing pressure. At 15.8 GPa, this peak is almost at the same position as the peak of $g_{\mathrm{AsAs}}(r)$. This fact implies that the order in the atomic configuration, which originates from the covalent interactions that are a remnant of the molecular liquid, disappears at this pressure.

6.5 Summary

By using *ab initio* molecular dynamics simulations, we have investigated the structural and bonding properties and the dynamics of liquid AsS under pressures up to 15.8 GPa. The present work confirms that the metallization of liquid AsS follows the pressure-induced transition from molecular to polymeric liquid. The profiles of the bond-overlap populations show that covalent interactions persist in the metallic state, which determines the pressure dependence of the dynamic properties. After polymerization, the As-S bond lengthens with increasing pressure, and the diffusion coefficients exhibit a local maximum near 5 GPa.

Chapter 7

Energy transport in light-harvesting dendrimer

7.1 Introduction

Harvesting energy from sunlight is of paramount importance for the solution of the global energy problem [94], for which synthetic supermolecules such as light-harvesting dendrimers [95] are attracting great attention [96]. In these molecules, electronic excitation energy due to photoexcitation of antennas located on the periphery of the molecules is rapidly transported to the photochemical reaction centers at the cores of the molecules, which in turn perform useful work such as photosynthesis and molecular actuation [97]. A number of experimental [98, 99, 100] and theoretical [101] works have addressed rapid energy transport mechanisms in light-harvesting dendrimers. Though such energy transfer is conventionally attributed to either dipole-dipole interactions (Forster mechanism) or the overlapping of donor and acceptor electronic wave functions (Dexter mechanism) [95], atomistic mechanisms of rapid electron transport in these dendrimers remain elusive. Here, we perform quantum-mechanical (QM) molecular dynamics (MD) simulations incorporating nonadiabatic electronic processes [102, 103] to identify atomistic mechanisms of rapid energy transport after photoexcitation of a light-harvesting dendrimer. The results reveal the key molecular motion (i.e. thermal vibration of the aromatic rings in the peripheral antennas), which significantly accelerates the energy transport based on the Dexter mechanism. The simulation results also elucidate the effect of temperature and solvent on the electron transport rate, which explains recent experimental observations.

7.2 Numerical details

The simulated system consists of a zinc-porphyrin core (labeled “ core ” in Fig. 7.1(a)) and a benzyl ether-type antenna. In the antenna, there are three aromatic rings connected by ether oxygen atoms, out of which one aromatic ring is directly connected to the zinc-porphyrin core. We hereafter refer to this ring as “ intermediate ” (labeled “ inter ” in Fig. 7.1(a)) and the other two rings bonded to the intermediate ring as “ peripheries ” (labeled “ peri ” in Fig. 7.1(a)). The periodic boundary condition is employed with a suprecell of dimensions $18 \times 18 \times 24$ Å^3, which is large enough to avoid the interaction between periodic images of the molecule. Namely, the total energy changes only slightly (0.01 meV/atom) when a larger supercell of $20 \times 20 \times 26$ Å^3 is used.

7.3 Result and discussion

7.3.1 Simulation result of the ground state

We first calculate the electronic structure of the system based on the density functional theory (DFT) The spatial distribution of some of the one-electron wave functions in the ground state is shown in Fig. 7.1(b), where the atomic positions are relaxed so as to minimize the total energy. It is seen from Fig. 7.1(b) that the highest occupied molecular orbital (HOMO) and the lowest unoccupied molecular orbital (LUMO) spread only within the core, which is consistent with the fact that electrons and holes photoexcited in the peripheries eventually move to the core. Figure 7.1(b) also shows the wave function of the occupied molecular orbital (MO) with the n-th highest energy but one (denoted as HOMO-n, where n = 1-4) and that of the unoccupied MO with the m-th lowest energy but one (denoted as LUMO+m, where m = 1-4). The wave functions of HOMO-1, HOMO-2, LUMO+1, and LUMO+2 are distributed mainly within the core. The eigenenergies of LUMO and LUMO+1 are almost degenerate within 0.01 eV, and they are separated well from the other states; the energy difference between HOMO and LUMO is about 2.0 eV, and that between LUMO+1 and LUMO+2 is about 1.3 eV. In contrast to these core states, HOMO-3, HOMO-4, LUMO+3, and LUMO+4 spread mainly within the peripheries. To study the effect of thermal molecular motions on the electronic wave functions, we next perform adiabatic MD simulation at a temperature of $T = 300$ K in the canonical ensemble, where the electrons stay in the ground state and the atomic forces are calculated

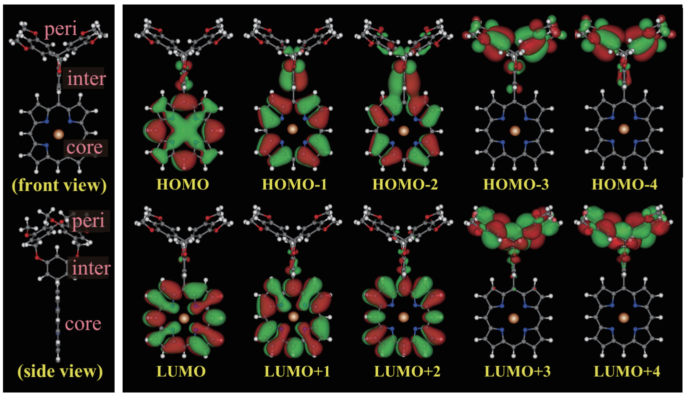

(a) (b)

Figure 7.1: (a) Simulated dendrimer consisting of a zinc-porphyrin core (labeled ‘core’) and a benzyl ether-type antenna that has one “intermediate” (labeled ‘inter’) and two “peripheries” (labeled ‘peri’) rings. The brown, blue, grey, red, and white balls indicate Zn, N, C, O, and H atoms, respectively. (b) Spatial distribution of electronic wave functions in the ground state, for HOMO, HOMO-n (MO with the n-th lowest energy but one, n = 1-4), LUMO, and LUMO+m (MO with the m-th highest energy but one, m = 1-4), where red and green colors represent the isosurfaces of the wave functions with the values of 0.013 and -0.013 a.u., respectively.

based on the DFT [104]. The left panel of Fig. 7.2 shows the time evolution of electronic eigenenergies ϵ_i during the MD simulation. From the time average of these eigenenergies, we calculate electronic densities of states (DOS) $\mathrm{D}_\alpha(E)$ projected to the wave functions of the atoms in molecular subsystems [47], where α = core, inter, peri for the zinc-porphyrin core, intermediate ring, and peripheral rings, respectively. The right panel of Fig. 7.2 shows $\mathrm{D}_{core}(E)$ (black solid curve), $\mathrm{D}_{inter}(E)$ (red dashed curve), and $\mathrm{D}_{peri}(E)$ (blue solid curve) at T = 300 K, along with the eigenenergies of the optimized structure at T = 0 K in Fig. 7.1 (horizontal lines). In $\mathrm{D}_{core}(E)$, there are peaks at 0.1, 2.1, and 3.3 eV (the origin of energy is taken at the HOMO eigenenergy at 0 K), whereas $\mathrm{D}_{peri}(E)$ has peaks at -0.3 and 4 eV. The differences between these energies are in good agreement with photo-absorption measurements at 25 °C [105]; the absorption peaks for the zinc-porphyrin core have been observed at the photon energies of about 2.2 and 3.0 eV (known as Q and Soret bands, respectively), and that for the peripheries has been observed around 4.4 eV. Even at a finite temperature of 300 K, the two core states, LUMO and LUMO+1, are not mixed with the other states, represented by the clear distinct peak at 2.1 eV in $\mathrm{D}_{core}(E)$ (right panel in Fig. 7.2). In contrast, LUMO+2, which also spreads only within the core at 0 K, mixes with the states in the intermediate and peripheral rings due to thermal fluctuation at 300 K, and $D_{core}(E)$ above 3 eV overlaps with $D_{inter}(E)$ and $D_{peri}(E)$. The left panel of Fig. 7.2 exhibits multiple crossings of eigenenergies in this energy range. When an eigenenergy is well separated from the others, its wave function has a large amplitude only within the core or one of the peripheries as shown in Figs. 7.2(a) and 7.2(b), respectively. On the other hand, the wave function spreads over both peripheries, when the LUMO+3 and LUMO+4 energies approach each other (Fig. 7.2(c)). Also, at a crossing of the LUMO+2 energy with another eigenenergy, the wave function spreads over both the core and a periphery (Fig. 7.2(d)). This suggests that electrons photoexcited in the peripheries are transferred to the core through such extended state, i.e., by the Dexter mechanism. A similar situation is observed for the occupied states (HOMO, HOMO-1, ...), which suggests that hole transport also occurs with the same mechanism.

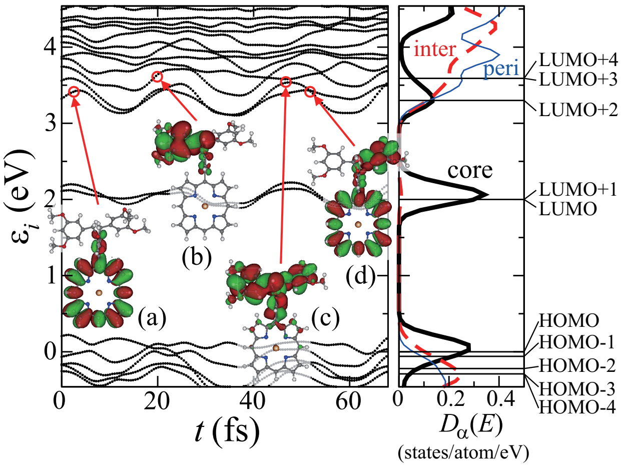

Figure 7.2: (Left panel) Time evolution of electronic eigenenergies during adiabatic MD simulation for the ground state. Spatial distribution of an electronic wave function is also shown for (a) LUMO+2 at 3 fs, (b) LUMO+4 at 20 fs, (c) LUMO+3 at 47 fs, and (d) LUMO+2 at 52 fs. (Right panel) Time-averaged electronic densities of states $D_\alpha(E)$, where the black solid, red dashed, and blue solid curves are for the core, intermediate, and peripheries, respectively.

7.3.2 Simulation results of the excited state

In order to confirm that a photoexcited electron indeed transfers based on the Dexter mechanism, we perform nonadiabatic MD simulations that incorporate electronic transitions through the fewest-switches surface-hopping (FSSH) method [102] along with the Kohn-Sham (KS) representation of time-dependent (TD) DFT [103]. The nuclei are treated classically in the adiabatic representation, i.e., the atomic forces are calculated from the (excited) electronic eigenstates for the current nuclear positions. Switching probability from the current adiabatic state to another is computed from the density-matrix elements obtained by solving the TDKS equations [103], and nonadiabatic transitions between adiabatic states occur stochastically[102]. We have estimated the many-body correction on an electron-hole pair excitation based on Casida's linear-response TDDFT [106] and found that the switching probability is modified by at most a few percent. The TDKS-FSSH simulations are initiated by exciting an electron from the HOMO-4 to LUMO+4 state at time $t = 0$, corresponding to the ultraviolet-light excitation in experiments [105]. We also calculate the distribution of oscillator strengths using Casida's linear-response TDDFT method [106], which agrees well with the observed absorption spectra. An example of the time evolution of the eigenenergies is shown in Fig. 7.3 (supplementary movie S1 shows this pro-

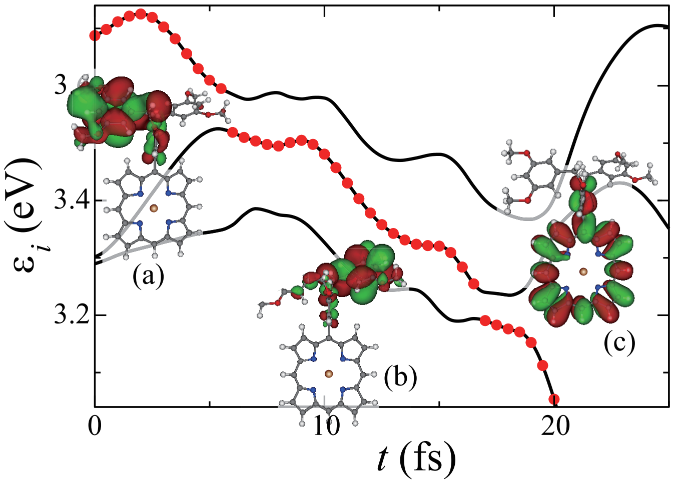

Figure 7.3: Time evolution of electronic eigenenergies in TDKS-FSSH simulation. The red circles denote energies of the electronic states occupied by the photoexcited electron. The spatial distribution of the wave function of the photoexcited electron is also shown at time t = (a) 0, (b) 10, and (c) 20 fs.

cess). Just after the excitation, the wave function of the occupied LUMO+4 is distributed mainly in the left periphery (Fig. 7.3(a)). At 6 fs, a transition from LUMO+4 to LUMO+3 occurs, accompanied by the transfer of the electron to the right periphery (Fig. 7.3(b)). Note that the eigenenergy of the right periphery is not always lower than that of the left periphery due to their crossings. At 17 fs, another transition to LUMO+2 occurs, causing the wave function of the occupied state to reside mainly within the core (Fig. 7.3(c)).

7.3.3 Effects of the environments

As demonstrated above, the crossings of eigenenergies ϵ_i due to thermal motions of atoms are crucial for electron transfer. With larger fluctuation of eigenenergies, the crossings are more frequent, resulting in fast energy transfer. The fluctuation of eigenenergies can be estimated from adiabatic MD simulations. We obtain the average standard deviation of eigenenergies, where is the time-averaged value and denotes the average over i = LUMO+2, LUMO+3, LUMO+4, as well as over time. From the time evolution of ϵ_i in Fig. 7.2, σ is calculated to be 0.13 eV at 300 K. When the temperature is decreased to 100 K, our MD simulation exhibits much smaller fluctuation, σ = 0.02 eV, which indicates that the energy transfer should be slower at lower temperatures. This explains a recent experiment on light-harvesting dendrimers [99], in which a remarkable temperature dependence of photoluminescence intensities indicates that the energy transfer from the peripheries to the core is suppressed at low temperatures (i.e. below 100 K). Since photoluminescence experiments for dendrimers are carried out in a solvent [99], we also consider the environmental effects on the electron transfer. To study the effect of the anhydrous tetrahydrofuran (THF) solvent used in the experiment, we explicitly introduce 14 THF molecules around the dendrimer as shown in Fig. 7.4(a) and treat them quantum-mechanically as well. The weak dispersion (van der Waals) interactions between the dendrimer and THF molecules are treated semiempirically,in the adiabatic MD simulations. The time evolution of electronic eigenenergies at 300 K is shown in Fig. 7.4(b), where both the results with and without the THF solvent are plotted. It is obvious that the solvent suppresses the fluctuation of eigenenergies, as the corresponding σ is reduced to only 0.04 eV.

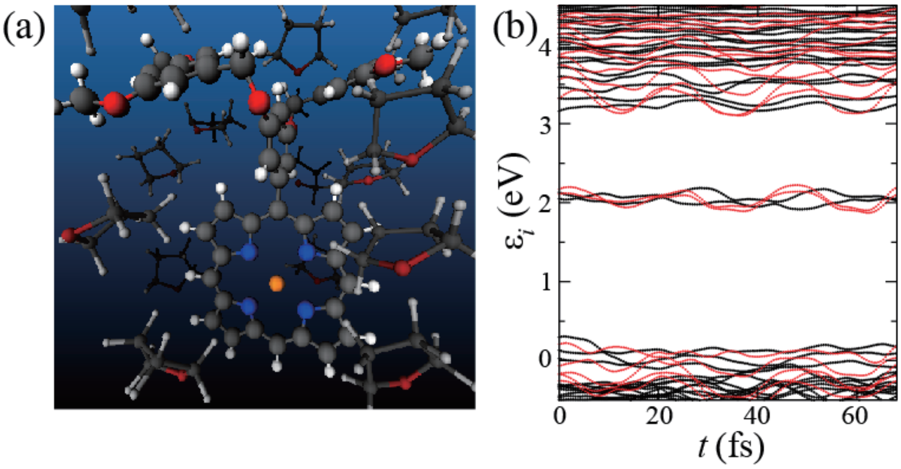

Figure 7.4: (a) A snapshot of atomic configuration. Dendrimer consisting of a zinc-porphyrin core with three benzenes and a benzyl ether-type antenna is surrounded by 14 THF molecules. The brown, blue, grey, red and white spheres represent Zn, N, C, O and H atoms, respectively. (b) Time evolution of electronic eigenenergies during adiabatic MD simulation at 300 K. The black and red curves are obtained from MD simulations with and without THF solvent, respectively.

7.3.4 Transfer time

In order to estimate the electron transfer time, additional TDKS-FSSH simulations are carried out, and Fig. 7.5 shows the time evolution of the existence probability $R_\alpha(t)$ (α = core or antenna) of a photoexcited electron obtained from the ensemble average over 40 simulations. Here, the solid and dashed curves show $R_\alpha(t)$ for the core and antenna regions, respectively, which are calculated in the same way as $D_\alpha(E)$ (the antenna region is defined as the intermediate plus the peripheries). The electron transfer time is estimated to be 40 fs. The corresponding electron transfer rate, 0.025 fs^{-1}, is found to be orders-of-magnitude larger than that due to the competing Forster mechanism.

7.4 Summary

Our quantum-mechanical molecular dynamics simulation incorporating nonadiabatic electronic transitions reveals the key molecular motion that significantly accelerates the energy transport based on the Dexter mechanism.

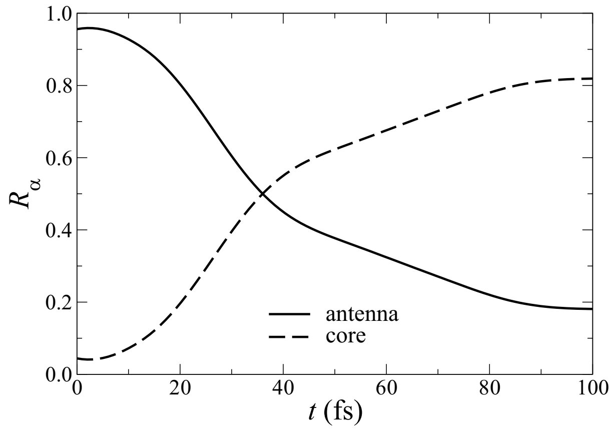

Figure 7.5: Time evolution of the existence probability $R_\alpha(t)$ of a photoexcited electron. The solid and dashed lines indicate $R_\alpha(t)$ for the core and antenna regions, respectively.

An essential feature of the electronic structure to support the rapid electron transfer is the existence of unoccupied levels in the peripheries just above LUMO+2 of the core, and that of occupied levels in the peripheries just below HOMO of the core. Crossings of these energy levels occur due to thermal fluctuation even in the ground state. Upon photoexcitation, the motion of aromatic rings connected by ether bonds enhances the lowering of the energy of the photoexcited state, thereby promoting such crossings further. The acceleration is less pronounced in the presence of solvent at low temperatures, which explains recent experimental observations.

Chapter 8

Summary

The dynamic and electronic properties of covalent liquids are studied by *ab initio* molecular dynamics simulation. The findings from this study are as follows;

(i) Liquid B_2O_3, SiO_2 and GeO_2 has diffusion maximum under high pressure. The diffusion mechanism in these three liquids always involves overcoordinated atoms such as BO_4, SiO_5 and GeO_5. High pressure leads to the forming overcoordination, that is, the diffusion coefficients increase with increasing pressure. On the other hand, the diffusivity of liquid $SrGeO_3$ decreases monotonically with increasing pressure. In liquid $SrGeO_3$, atomic diffusion occurs by switching back and forth between single and double bond. In other words, liquid $SrGeO_3$ does not need overcoordinated atoms when atoms diffuse. This is the reason why liquid $SrGeO_3$ does not have diffusion maximum under high pressure. In addition, liquid B_2O_3 and SiO_2 have dynamic asymmetry under high pressure. That is, the diffusion coefficients of higher coordinate atom (Si in SiO_2, B in B_2O_3) is more than twice that of the other atom (O in both liquid). The origin of this anomaly is that bridging oxygen still exists as diffusion path at higher pressure region where almost all other atoms (Si, B) is over coordination. In this pressure region, there are diffusion path for Si or B atom but there are no diffusion path for O atom. On the other hand, liquid GeO_2 which has similar local unit with liquid SiO_2 does not have dynamic asymmetry. In GeO_2, it does not need high energy to make overcoordinated atoms compared to SiO_2 or B_2O_3. That is, diffusion path exists for O atoms as well as Ge atoms despite high pressure. This is the reason why dynamic asymmetry does not appear in liquid GeO_2.

(ii) In liquid chalcogenide, the covalent-like interaction which is a remnant of ambient pressure plays important role for the pressure-induced metalization. Even after metallization, there is a microscopic covalent-like interaction between atoms, which results in a peculiar behavior in both liquids. For liquid Se, after metallization, there is a characteristic first coordination shell in which each atom interacts with neighboring atoms through covalent like bonding as a remnant of chain structure. As a result, the radial distribution function of liquid Se under pressure has a peculiar shape in the sense that there are no clear peaks like in a dilute gas. For liquid AsS, the distance between As and S becomes longer with increasing pressure even after metallization. In addition, the diffusion coefficients have local maximum in the pressure range of the metallic state.

(iii) In the light-harvesting dendrimer, energy transport from antennas to core occors with Dexter mechanism. An essential feature of the electronic structure to support the rapid electron transfer is the existence of unoccupied levels in the peripheries just above LUMO+2 of the core, and that of occupied levels in the peripheries just below HOMO of the core. Crossings of these energy levels occur due to thermal fluctuation even in the ground state. Upon photoexcitation, the motion of aromatic rings connected by ether bonds enhances the lowering of the energy of the photoexcited state, thereby promoting such crossings further. The acceleration is less pronounced in the presence of solvent at low temperatures, which explains recent experimental observations [13].

Acknowledgements

This research would not have been possible without the support of many people. I wish to express my gratitude to my supervisor, Professor Fuyuki Shimojo who was abundantly helpful and offered invaluable assistance, support and guidance. Deepest gratitude are also due to Professor Aiichiro Nakano and Professor Ken-ichi Nomura at University of Southern California without whose knowledge and assistance this study would not have been successful. Special thanks also to all the member of Shimojo's labolatory; Mr. Akihide Koura, Mr. Kohei Shimamura, Mr. Keisuke Goto and Mr. Daiki Fukunaga for sharing the literature and invaluable assistance. I would like to acknowledge the financial support of the KAKENHI [Grant-in-Aid for JSPS Fellows No. 22 • 1853]. I furthermore thank the Research Institute for Information Technology, Kyushu University, for the use of its facilities. The computations were also performed using the computer facilities at the University of Southern California and at the Supercomputer Center, Institute for Solid State Physics, University of Tokyo. Finally I am grateful to my parents and their understanding through the duration of my studies.

Bibliography

[1] Y. Katayama, T. Mizutani, W. Utsumi, O. Shimomura, M. Yamakata, and K. I. Funakoshi. *Nature*, 403:170–173, 2000.

[2] S. K. Sharma, D. Virgo, and I. Kushiro. *J. Non-Cryst. Solids*, 33:235–248, 1979.

[3] K. I. Funakoshi, A. Suzuki, and H. Terasaki. *J. Phys.: Condens. Matter*, 14:11343–11347, 2002.

[4] P. F. McMillan and M. C. Wilding. *J. Non-Cryst. Solids*, 355:722–732, 2009.

[5] P. Hohenberg and W. Kohn. *Phys. Rev.*, 136:B864–B871, 1964.

[6] R. M. Martin. *Electronic Structure*. Cambridge University Press, 2004.

[7] A. D. Becke. *Phys. Rev. A*, 38:3098–3100, 1988.

[8] Chengteh Lee, Weitao Yang, and Robert G. Parr. *Phys. Rev. B*, 37:785–789, 1988.

[9] R. Colle and O. Salvetti. *Theoretica Chimica Acta*, 37:329–334, 1975.

[10] J. P. Perdew, K. Burke, and M. Ernzerhof. *Phys. Rev. Lett.*, 77:3865–3868, 1996.

[11] P. E. Blöchl. *Phys. Rev. B*, 50:17953, 1994.

[12] G. Kresse and D. Joubert. *Phys. Rev. B*, 59:1758–1775, 1999.

[13] G. E. Gurr, P. W. Montgomery, C. D. Knutson, and B. T. Gorres. *Acta Cryst. B*, 26:906, 1970.

[14] P. A. V. Johnson, A. C. Wright, and R. N. Sinclair. *J. Non-Cryst. Solids*, 50:281–311, 1982.

[15] C. T. Prewitt and R. D. Shannon. *Acta Cryst. B*, 24:869, 1968.

[16] D. Nieto-Sanz, P. Loubeyre, W. Crichton, and M. Mezouar. *Phys. Rev. B*, 70:214108, 2004.

[17] V. V. Brazhkin, Y. Katayama, K. Trachenko, O. B. Tsiok, A. G. Lyapin, E. Artacho, M. Dove, G. Ferlat, Y. Inamura, and H. Saitoh. *Phys. Rev. Lett.*, 101:035702, 2008.

[18] S. K. Lee, P. J. Eng, H. K. Mao, Y. Meng, M. Newville, M. Y. Hu, and J. F. Shu. *Nature Mater.*, 4:851–854, 2005.

[19] M. Massot and M. Balkanski. *Disorder in Condensed Matter Physics,* edited by J. A. Blackman and J. Taguena, page 74. Oxford, New York, 1991.

[20] *Optical Constants of Inorganic Glasses,* edited by A. M. Efimov, page 88. CRC, New York, 1995.

[21] J. Sakowski and G. Herms. *J. Non-Cryst. Solids*, 293-295:304–311, 2001.

[22] S. Ohmura and F. Shimojo. *Phys. Rev. B*, 78:224206, 2008.

[23] V. V. Brazhkin, Y. Katayama, Y. Inamura, M. V. Kondrin, A. G. Lyapin, S. V. Popova, and R. N. Voloshin. *JETP Lett.*, 78:393–397, 2003.

[24] V. V. Brazhkin and A. G. Lyapin. *J. Phys.: Condens. Matter*, 15:6059–6084, 2003.

[25] J. Diefenbacher and P. F. McMillan. *J. Phys. Chem. A*, 105:7973–7978, 2001.

[26] B. B. Karki, D. Bhattarai, and L. Stixrude. *Phys. Rev. B*, 76:104205, 2007.

[27] V. Van Hoang, H. Zung, and N. T. Hai. *J. Phys.: Condens. Matter*, 19:116104, 2007.

[28] A. Takada, C. R. A. Catlow, J. S. Lin, G. D. Price, M. H. Lee, V. Milman, and M. C. Payne. *Phys. Rev. B*, 51:1447–1455, 1995.

[29] D. Li and W. Y. Ching. *Phys. Rev. B*, 54:13616–13622, 1996.

[30] U. Engberg. *Phys. Rev. B*, 55:2824–2830, 1997.

[31] M. M. Islam, T. Bredow, and C. Minot. *Chem. Phys. Lett.*, 418:565–568, 2006.

[32] T. Uchino and T. Yoko. *J. Chem. Phys.*, 105:4140–4150, 1996.

[33] P. Umari and A. Pasquarello. *Phys. Rev. Lett.*, 95:137401, 2005.

[34] S. Ohmura and F. Shimojo. *Phys. Rev. B*, 80:020202, 2009.

[35] M. Tuckerman, B. J. Berne, and G. J. Martyna. *J. Chem. Phys.*, 97:1990–2001, 1992.

[36] G. Kresse and J. Hafner. *Phys. Rev. B*, 49:14251–14269, 1994.

[37] F. Shimojo, R. K. Kalia, A. Nakano, and P. Vashishta. *Comput. Phys. Commun.*, 140:303–314, 2001.

[38] P. B. Macedo, W. Capps, and T. A. Litovitz. *J. Chem. Phys.*, 44:3357, 1966.

[39] G. J. Martyna, D. J. Tobias, and M. L. Klein. *J. Chem. Phys.*, 101:4177–4189, 1994.

[40] S. Nosé. *Mol. Phys.*, 52:255–268, 1984.

[41] W. G. Hoover. *Phys. Rev. A*, 31:1695–1697, 1985.

[42] O. H. Nielsen and R. M. Martin. *Phys. Rev. B*, 32:3780–3791, 1985.

[43] A. Dal Corso and R. Resta. *Phys. Rev. B*, 50:4327–4331, 1994.

[44] A. C. Hannon, D. I. Grimley, R. A. Hulme, A. C. Wright, and R. N. Sinclair. *J. Non-Cryst. Solids*, 177:299–316, 1994.

[45] *Since the first peak of* $g_{\mathrm{B-O}}(r)$ *is rather asymmetric, we do not calculate* $N_{\mathrm{B-O}}$ *as the integration up to* $r_{\mathrm{B-O}}$ *(times two).*

[46] R. S. Mulliken. *J. Chem. Phys.*, 23:1841–1846, 1955.

[47] F. Shimojo, A. Nakano, R. K. Kalia, and P. Vashishta. *Phys. Rev. E*, 77:066103, 2008.

[48] John Kieffer. *Phys. Rev. B*, 50:17–29, 1994.

[49] D. Marrocchelli, M. Salanne, and P. A. Madden. *J. Phys.: Condens. Matter*, 22, 2010.

[50] S. Ohmura and F. Shimojo. *Phys. Rev. B*, 81, 2010.

[51] G. S. Smith and P. B. Isaacs. *Acta Crystallogr.*, 17:842–846, 1964.

[52] Y. Shimizu, Y. Syono, and S. Akimoto. *HTHP*, 2:113–120, 1970.

[53] W. A. Harrison. *Electronic Structure and the Properties of Solids.* Freeman, San Francisco, 1980.

[54] Y. Akahama, M. Kobayashi, and H. Kawamura. *Phys. Rev. B*, 47:20–26, 1993.

[55] M. I. McMahon, C. Hejny, J. S. Loveday, L. F. Lundegaard, and M. Hanfland. *Phys. Rev. B*, 70, 2004.

[56] J. C. Jamieson and D. B. McWhan. *J. Chem. Phys.*, 43:1149–1152, 1965.

[57] K. Aoki, O. Shimomura, and S. Minomura. *J. Phys. Soc. Jpn.*, 48:551–556, 1980.

[58] P. Vulliet and J. P. Sanchez. *Phys. Rev. B*, 58:171–174, 1998.

[59] G. Parthasarathy and W. B. Holzapfel. *Phys. Rev. B*, 37:8499–8501, 1988.

[60] Y. Ohmasa, I. Yamamoto, Yao Makoto, and H. Endo. *J. Phys. Soc. Jpn.*, 64:4766–4789, 1995.

[61] T. Tsuzuki, M. Yao, and H. Endo. *J. Phys. Soc. Jpn.*, 64:485–503, 1995.

[62] J. C. Perron, J. Rabit, and J. F. Rialland. *Philos. Mag. B*, 46:321–330, 1982.

[63] H. Hoshino, R. W. Schmutzler, W. W. Warren, and F. Hensel. *Philos Mag*, 33:255–259, 1976.

[64] W. W. Warren Jr and R. Dupree. *Phys. Rev. B*, 22:2257–2275, 1980.

[65] H. Ikemoto, I. Yamamoto, M. Yao, and H. Endo. *J. Phys. Soc. Jpn.*, 63:1611–1621, 1994.

[66] K. Tamura and M. Inui. *J. Phys.: Condens. Matter*, 13:R337, 2001.

[67] F. Shimojo, K. Hoshino, M. Watabe, and Y. Zempo. *J. Phys.: Condens. Matter*, 10:1199–1210, 1998.

[68] F. Kirchhoff, G. Kresse, and M. J. Gillan. *Phys. Rev. B*, 57:10482–10495, 1998.

[69] V. V. Brazhkin, K. Funakoshi, M. Kanzaki, and Y. Katayama. *Phys. Rev. Lett.*, 99:245901, 2007.

[70] J. Y. Raty, J. P. Gaspard, T. Le Bihan, M. Mezouar, and M. Bionducci. *J. Phys.: Condens. Matter*, 11:10243–10249, 1999.

[71] K. Tsuji. *J. Non-Cryst. Solids*, 117-118:27–34, 1990.

[72] Y. Katayama, T. Mizutani, W. Utsumi, O. Shimomura, and K. Tsuji. *Phys. Stat. Sol. B*, 223:401–404, 2001.

[73] N. Funamori and K. Tsuji. *Phys. Rev. B*, 65:141051–141055, 2002.

[74] F. Shimojo, K. Hoshino, and Y. Zempo. *J. Phys. Soc. Jpn.*, 72:2822–2828, 2003.

[75] D. E. Harrison. *J. Chem. Phys.*, 41:844, 1964.

[76] M. A. Tuktabiev, S. V. Popova, V. V. Brazhkin, A. G. Lyapin, and Y. Katayama. *J. Phys.: Condens. Matter*, 21:385401, 2009.

[77] R. Zallen and M. L. Slade. *Phys. Rev. B*, 18:5775, 1978.

[78] E. Hinze and J. Lauterjung. *High Pressure Research: An International Journal*, 4:324 – 326, 1990.

[79] K. Tamura, S. Hosokawa, M. Inui, M. Yao, H. Endo, and H. Hoshino. *J. Non-Cryst. Solids*, 150:351–355, 1992.

[80] S. Hosokawa and K. Tamura. *J. Phys.: Condens. Matter*, 16:R1465, 2004.

[81] Y. Kajihara, M. Inui, K. Matsuda, K. Tamura, and S. Hosokawa. *J. Non-Cryst. Solids*, 353:1985–1989, 2007.

[82] X. F. Zhu and L. F. Chen. *Physica B: Condensed Matter*, 403:3302–3306, 2008.

[83] F. Shimojo, S. Munejiri, K. Hoshino, and Y. Zempo. *J. Phys.: Condens. Matter*, 11:L153–L158, 1999.

[84] F. Shimojo, S. Munejiri, K. Hoshino, and Y. Zempo. *J. Phys.: Condens. Matter*, 12:6161–6172, 2000.

[85] F. Shimojo, S. Munejiri, K. Hoshino, and Y. Zempo. *J. Non-Cryst. Solids*, 312-314:349–355, 2002.

[86] V. V. Brazhkin, Y. Katayama, M. V. Kondrin, T. Hattori, A. G. Lyapin, and H. Saitoh. *Phys. Rev. Lett.*, 100:145701, 2008.

[87] V. V. Brazhkin, M. Kanzaki, Ken-ichi Funakoshi, and Y. Katayama. *Phys. Rev. Lett.*, 102:115901, 2009.

[88] S. Ohmura and F. Shimojo. *Phys. Rev. B*, 83:134206, 2011.

[89] I. Stich, M. Parrinello, and J. M. Holender. *Phys. Rev. Lett.*, 76:2077, 1996.

[90] M. M. G. Alemany, Manish Jain, Leeor Kronik, and James R. Chelikowsky. *Phys. Rev. B*, 69:075101, 2004.

[91] F. Shimojo, K. Hoshino, and Y. Zempo. *J. Non-Cryst. Solids*, 312-314:388–391, 2002.

[92] P. Bonazzi, S. Menchetti, and G. Pratesi. *Am. Miner.*, 80:400–403, 1995.

[93] S. Tsuneyuki and Y. Matsui. *Phys. Rev. Lett.*, 74:3197, 1995.

[94] G. W. Crabtree and N. S. Lewis. *Physics Today*, 60:37–42, 2007.

[95] F. Vogtle, G. Richardt, and N. Werner. *Dendrimer Chemistry.* Wiley-VCH, Weinheim, 2009.

[96] B. L. Rupert, W. J. Mitchell, A. J. Ferguson, M. E. Kose, W. L. Rance, G. Rumbles, D. S. Ginley, S. E. Shaheen, and N. Kopidakis. *J. Mater. Chem*, 19:–5324, 2009.

[97] T. Muraoka, K. Kinbara, and T. Aida. *Nature*, 440:512–515, 2006.

[98] I. Akai, H. Nakao, K. Kanemoto, T. Karasawa, H. Hashimoto, and M. Kimura. *J. Lumin.*, 112:449–453, 2005.

[99] A. Yamada, A. Ishida, I. Akai, M. Kimura, I. Katayama, and J. Takeda. *J. Lumin.*, 129:1898, 2009.

[100] I. Akai, K. Miyanari, T. Shimamoto, A. Fujii, H. Nakao, A. Okada, K. Kanemoto, T. Karasawa, H. Hashimoto, A. Ishida, A. Yamada, I. Katayama, J. Takeda, and M. Kimura. *New J. Phys.*, 10:125024, 2008.

[101] Y. Kodama, S. Ishii, and K. Ohno. *J. Phys.: Condens. Matter*, 21:064217, 2009.

[102] J. C. Tully. *J. Chem. Phys.*, 93:1061–1071, 1990.

[103] W. R. Duncan, C. F. Craig, and O. V. Prezhdo. *J. Am. Chem. Soc*, 129:8528–8543, 2007.

[104] F. Shimojo, S. Ohmura, R. K. Kalia, A. Nakano, and P. Vashishta. *Phys. Rev. Lett.*, 104:126102, 2010.

[105] I. Akai, T. Kato, K. Kanemoto, T. Karasawa, M. Ohashi, S. Shinoda, and H. Tsokube. *Phys. Stat. Sol. C*, 3:3420–3425, 2006.

[106] M. E. Casida. *Time-Dependent Density Functional Response Theory for Molecules*, page 155. World Scientific, Singapore, 1995.